Thermal Meson Properties from Correlation Functions and their Spectral Representation

Dissertation

zur Erlangung des Doktorgrades
an der Fakultät für Physik
der Universität Bielefeld

vorgelegt von
Sven Stickan

November 2003

Contents

List of Figures

List of Tables

Introduction

> *How many bodies are required before we have a problem? G.E. Brown points out that this can be answered by a look at history. In eighteenth-century Newtonian mechanics, the three-body problem was insoluble. With the birth of relativity around 1910 and quantum electrodynamics in 1930, the two- and one- body problems became insoluble. And with modern quantum field theory, the problem of zero bodies (vacuum) is insoluble. So, if we are out after exact solutions, no bodies at all is already too many!*
>
> R. D. Mattuck

The strong interaction is one of the four fundamental forces in physics. It is described by quantum chromodynamics (QCD) which is expected to show a rich and interesting phase structure at high temperatures and/or densities. The appearance of these new phases is related to a feature of QCD which is called “asymptotic freedom” and is discovered in deep inelastic scattering experiments. It predicts a weakening of the interaction at large momentum transfers between the constituents. It has soon be realized that this feature leads to a new state of matter in a dense and hot environment. This form of matter is called quark gluon plasma (QGP) and is expected to exist in cold and dense cores of neutron stars and has been existing in the hot early universe. The relevant degrees of freedom which describe these forms of matter are no longer hadrons but the constituents of QCD, the quarks and gluons.

Two large heavy ion colliders will be utilized to create a hot fireball by colliding two relativistic ion (with number of nucleons, $A \sim 200$) beams. One is the relativistic heavy ion collider (RHIC) at the BNL in Brookhaven with a center of mass energy of $\sqrt{s} \sim$ 200AGeV, and the other one is the large hadron collider (LHC) at CERN in Geneva with $\sqrt{s} \sim$ 5500AGeV. In this fireball the conditions for the creation of the QGP are expected to be reproduced so that one is able to to study its properties. To provide evidence that this new form of matter is indeed created in a heavy ion collision, a coherent picture emerging from very different observables is necessary[1]. Some prominent examples commonly discussed are[2]: jet quenching, particle ratios, strangeness enhancement, J/Ψ suppression and dilepton and photon production.

These signals depend on the medium properties in different stages of the fireball evolution. This evolution is depicted in Fig. 1(a) and consists of four major steps: Thermalization, QGP, Hadron gas and freeze-out state.[1] To study the matter in these different stages of a heavy ion collision, different theoretical concepts have been developed. The thermalization phase needs methods applicable for systems far from equilibrium. In the subsequent steps thermal equilibration is usually assumed. The first one is the QGP. It is expected to be created from the experiments, mentioned before, at temperatures a few times the QGP phase transition temperature. A description of this phase as a weakly interacting gas of quarks and gluons is motivated by perturbative aspects of QCD. At these temperatures, however, the interactions are still too strong to be reliably treated by perturbative methods. The properties in the hadronic phase, to which the system will condense during the next step of the evolution, are tried to be described in different hadronic models. The last freeze-out stage can be described using well known hadron phenomenology[6]. We will be concerned here with the properties of the QGP and Hadron Gas stages, which may be described by equilibrium thermodynamics. The only known tool to study their features in a common framework is lattice gauge theory (LGT) which we are going to use here.

In this work we will focus on the modifications of hadron properties, e.g., their mass, in a

---

[1] A mixed state needs a first order phase transition from the QGP to the deconfined phase, which is disfavored by currently available lattice calculations[5].

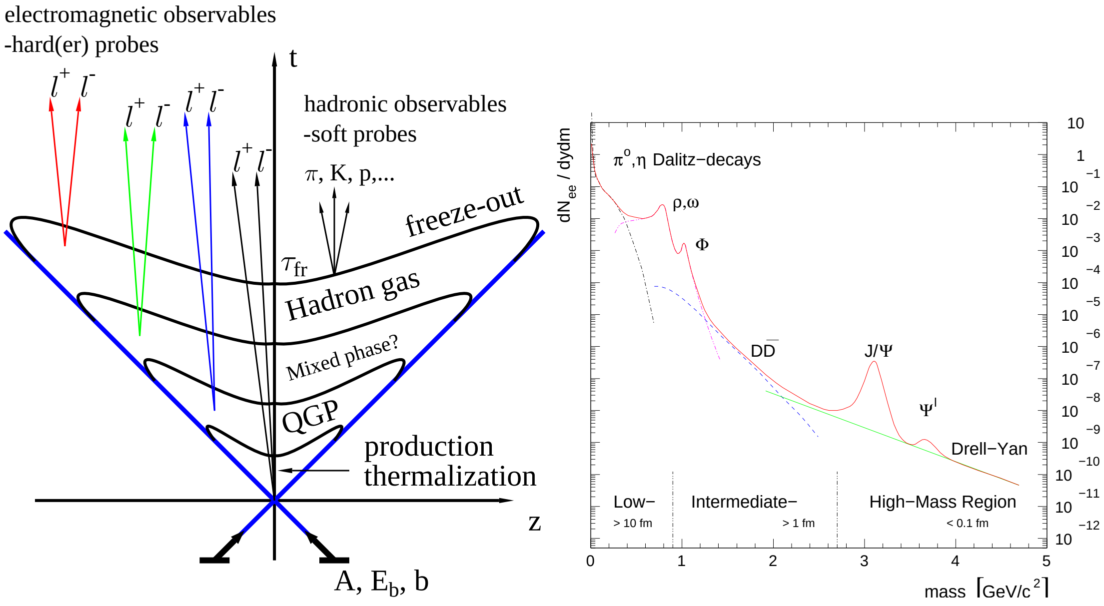

(a) (b)

Figure 1: (a) Space-time evolution of an A+A collision [3] and (b) dilepton rates and contribution of hadron resonances in different dilepton mass regions [4].

thermal medium which can either be the hadron gas or the QGP. Lattice calculations provide information on this through the calculation of Euclidean meson correlation functions. Through their relation to the thermal meson spectral functions these correlation functions can provide information on the temperature dependence of hadron masses as well as the very existence of bound states. Moreover, spectral functions are directly related to experimentally observable dilepton rates[7]. Having determined the meson spectral functions, in particular the spectral function in the vector channel, we can make contact to the thermal rates from (vector) mesons seen experimentally in the spectrum of dileptons ($e^+e^-, \mu^+\mu^-$) at various values of the invariant mass. Of particular interest is the region of light vector mesons (ρ, ω, ϕ), the region of heavy quark bound states $J/\psi, \Psi'$ as well as the thermal modification of rates in the continuum regions. These different invariant mass regimes are illustrated in Fig. 1(b) which receive contributions from different stages of the fireball evolution (See Fig. 1(a)). In this work we will discuss properties of meson correlation functions constructed from light quarks. We thus will focus on thermal properties of light mesons ($\rho, \omega, \cdots$) as well as dilepton rates resulting from the annihilation of light quark anti-quark pairs, which was one of the first suggested observables of the QGP in heavy ion collisions [8].

The lighter vector states have a lifetime short enough to decay within the medium, and therefore, medium effects in this channel will modify the vector SPF and thus will also lead to a modified dilepton yield. Such medium effects in the dilepton rate at low and intermediate masses have indeed been observed in nucleus nucleus collisions [9, 10, 11] by comparing the measured rate to the one obtained by scaling the nucleon nucleus rates ("Cocktail" rate). The theoretical interpretation is, however, still ambiguous and involves many interesting features of QCD, like chiral symmetry restoration, deconfinement and quark hadron duality. As the connection between the vector meson SPF and the dilepton rates holds for all phases, shown in Fig. 1(a), for which thermal equilibrium is usually assumed, a computation of these rates in the framework of LGT is particularly suited to clarify the interpretation of the experimental data.

As LGT is formulated at imaginary times, for a long time a calculation of real time spectral functions was possible only by using strong assumptions. At finite temperature, however, only little a priori knowledge on the structure of the spectral function exists, which could justify assumptions on their shape. The maximum entropy method (MEM) is designed to solve this problem[12], and its possibilities are therefore investigated in the present work in detail. Moreover, the spectral functions are calculated for the first time in the free lattice gauge theory which presents a ground setting analysis for the investigation of mesonic spectral functions on the lattice, in particular for their sensitivity to cut-off effects. Additionally, the dilepton and photon rates, obtained from the meson spectral functions, calculated with MEM, are presented.

This work is organized as follows:

In the first chapter, QCD is introduced as a continuum quantum gauge field theory in the path integral formalism. Appended is a detailed description of the different phases and symmetries of the QCD Lagrangian and the expected consequences for hadron phenomenology is discussed.

In the second chapter, the discretization of QCD is described and the subtleties, accompanying this procedure, for the fermion action, are carefully explored. In particular, the problems which arise from an explicit breaking of chiral symmetry in the Wilson fermion formulations used in our work is discussed. Additionally, various aspects concerning the continuum limit are presented. As the most important measured observables are correlation functions, the determination of the meson properties from them is discussed. Finally, the explicit implementation of the Monte Carlo integration method and the treatment of statistical errors is presented.

The third chapter is devoted to the free lattice field theory. First, the continuum calculation of the spectral function and the correlation functions is presented. Next, this calculation is performed for the Wilson discretization scheme in its most general form. After that, the computations are repeated for the more involved truncated fixed point action. Discretization effects of these different fermion formulations are discussed for correlation functions and the spectral functions. Additionally, the properties of improved meson operators in the spectral representation are explored.

In the last chapter, the parameters of the simulations are discussed first. Then, the temperature influence on the quark mass is discussed. Next, the maximum entropy method is explained and several tests and details on the implementation of this method are reviewed. Meson properties and their cut-off dependencies visible in the screening masses, temporal correlation functions and the spectral functions are investigated afterwards. This is done for temperatures belonging to the hot hadronic as well as to the deconfined phase. Then, the dilepton production processes in heavy ion collisions are reviewed and the non-perturbative calculation of these processes in the QGP phase is presented. In the end, the possibility of calculating the photon rate using the same methods is explored.

Chapter 1

Continuum QCD

> *There is at present a unique candidate to be a theory of strong interactions which satisfies Feynman's criteria: it is simple and not obviously wrong*
>
> Kenneth G. Wilson

This chapter starts with the formulation of QCD as a non-abelian $SU(3)$ gauge theory and reviews its two basic phenomenological features, asymptotic freedom and confinement. In the second section a discussion of the different phases of QCD and their relation to the symmetry of the Lagrangian is presented.

1.1 Formulation of QCD

QCD is a non-abelian $SU(3)$ gauge theory and describes the strong interaction between the fundamental constituents of the theory, the quarks and the gluons. The quarks can be grouped in three generations. The first consists of the (u)p and (d)own quarks which are the lightest massive objects in QCD with $m_{u,d} \approx 5\text{MeV}$[13]. The next generation is made of the (s)trange and the (c)harm quarks. The s quark is with $m_s \approx 140\text{MeV}$ moderately heavy as opposed to the c quark with $m_c \approx 1.2\text{GeV}$. The third generation of quarks contains the (b)ottom and the (t)op quarks with even larger masses $m_b \approx 4\text{GeV}$ and $m_t \approx 175\text{GeV}$. The topics explored within this thesis deal mostly with the light quark sector around a critical temperature of $\mathcal{O}(100\text{MeV})$. Hence the influence of heavier quarks can be neglected, i.e., they are treated as infinitely heavy. This approximation should be valid at least for the charm and higher quark masses. Whether this is true also for the strange quark is questionable and therefore the number of light flavors n_f is not further specified at the moment. Its influence on the QCD phase transition will be discussed in

Section 1.2.2. The second group of constituents of QCD, the gluons, are however massless by construction, and the general Lagrangian for QCD becomes

$$\begin{aligned}\mathcal{L}_{QCD}(x) &= \mathcal{L}_F(x) + \mathcal{L}_G(x) &(1.1)\\ \mathcal{L}_F &= \sum_{f=1}^{n_f} \overline{\psi}^f(x)(i\gamma_\mu D^\mu - m_f \mathbb{1})\psi^f(x) &(1.2)\\ \mathcal{L}_G(x) &= -\frac{1}{4}\sum_{a=1}^{N_c^2-1} G^a_{\mu\nu}(x) G_a^{\mu\nu}(x) &(1.3)\end{aligned}$$

with the quark fields $\psi, \overline{\psi}$ and the gluon field strength tensor $G_{\mu\nu}$. The Dirac matrices are defined by the Clifford algebra $\{\gamma_\mu, \gamma_\nu\} = 2g_{\mu\nu}$. The interaction, with the coupling constant g, is introduced by the covariant derivative

$$\begin{aligned}D_\mu &= \partial_\mu - igA_\mu &(1.4)\\ A_\mu(x) &= \sum_{a=1}^{8} A^a_\mu(x)\frac{\lambda^a}{2}\ . &(1.5)\end{aligned}$$

The non-commuting generators λ^a of the $SU(3)$ lead to the non-vanishing structure constants f_{abc} in the field strength tensor

$$G^a_{\mu\nu} = \partial_\mu A^a_\nu - \partial_\nu A^a_\mu - g f^a_{bc} A^b_\mu A^c_\nu \tag{1.6}$$

which gives rise to the gluon self interaction described by $\mathcal{L}_G$.

The quantization of the theory is achieved by the Euclidian Path integral formulation with the QCD partition function

$$Z^{(E)}(T,V) = \int \mathcal{D}A\mathcal{D}\psi\mathcal{D}\overline{\psi}\ \exp\left\{-S^{(E)}_{QCD}(T,V)\right\} \tag{1.7}$$

depending on the temperature T and the volume V. The associated action

$$S^{(E)}_{QCD}(V,T) = \int\limits_0^{1/T} \mathrm{d}\tau \int\limits_V \mathrm{d}^3x\ \mathcal{L}^{(E)}_{QCD} \tag{1.8}$$

is defined by an integral of the Lagrangian over the space and imaginary time τ. The latter is restricted to the finite interval $[0, 1/T)$ through which the temperature of the system is defined. The Euclidian Lagrangian

$$\mathcal{L}^{(E)}_{QCD} = \sum_{f=1}^{n_f} \overline{\psi}^f(x)\ (i\gamma^{(E)}_\mu D_\mu + m_f\mathbb{1})\ \psi^f(x) + \frac{1}{4}\sum_{a=1}^{N_c^2-1} G^a_{\mu\nu}(x)G_a^{\mu\nu}(x) \tag{1.9}$$

is obtained from Eq.(1.1) by replacing $it \to \tau$ and $\gamma_\mu \to \gamma^{(E)}_\mu$ with the Euclidian Dirac matrices defined by $\{\gamma^{(E)}_\mu, \gamma^{(E)}_\nu\} = 2\ \mathbb{1}_{\mu\nu}$ and listed in Appendix A.1. In thermal equilibrium the expectation value of any observable O is then given by

$$\langle O\rangle_T = \frac{1}{Z^{(E)}(V,T)}\int \mathcal{D}A\mathcal{D}\psi\mathcal{D}\overline{\psi}\ O(A,\overline{\psi},\psi)\ \exp\left\{-S^{(E)}_{QCD}(T,V))\right\}\ . \tag{1.10}$$

From now on only the Euclidian metric will be used, so that the subscript (E) is omitted.

1.2 Phases and Symmetries of QCD

QCD describes two fundamental properties of the strong interactions, asymptotic freedom and chiral symmetry, which are important at the different limits of the length scales. Due to quantum fluctuations the coupling "constant" becomes a function of the length scale/momentum transfer (q) of any physical process one considers. This leads to the running coupling in lowest order perturbation theory

$$\alpha(q) = \frac{\alpha(\Lambda)}{1 + \alpha(\Lambda)\frac{33-2n_f}{12\pi}\ln(\frac{q^2}{\Lambda^2})} , \tag{1.11}$$

where $\alpha = g^2/4\pi$ and Λ is a mass scale which has to be fixed by experiment. In the limit of small distances (large momentum q) the coupling gets small and leads to weaker interactions among the gluons themselves and the gluons with the quarks. Hence the constituents of QCD can be described as nearly free particles in this limit and the usual perturbative methods can be applied. This is called asymptotic freedom. Nevertheless, at large length scales and small momenta, the coupling grows. This results in a potential which rises linearly with distance. For this reason it is impossible to separate two quarks from each other and the quarks are bound into hadrons. This phenomenon is called confinement. In this regime of hadronic scales the coupling is too large for usual perturbation theory to hold. One way to treat QCD in this regime is to construct effective models like the MIT-Bag Model or σ-models. Their validity is however always restricted to certain aspects of the theory. A complete description of hadrons therefore requires non-perturbative techniques like lattice gauge theory. This approach is described in Section 2 and will provide the framework used within this thesis.

1.2.1 Symmetries of the Lagrangian

The further description of QCD requires the discussion[14] of symmetries. First of all, the theory is a relativistic field theory and therefore invariant under Poincare transformations. Furthermore it is a gauge theory which is by construction invariant under local field transformations

$$\psi(x) \quad\rightarrow\quad G(x)\psi(x) \tag{1.12}$$
$$\overline{\psi}(x) \quad\rightarrow\quad \overline{\psi}(x)G^\dagger(x) \tag{1.13}$$
$$A_\mu(x) \quad\rightarrow\quad G(x)A_\mu(x)G^\dagger(x) - g^{-1}(\partial_\mu G(x))G^\dagger(x) \tag{1.14}$$

with $G(x)$ as an element of the $SU(3)$ color gauge group. The gauge fields self interact and responsible for the confinement at low temperatures. This confined phase is described as the phase in which only colorless objects can exist.

The hadronic scale $\Lambda \simeq 1\text{GeV}$ is much larger than the up and down quark mass and still larger than the strange quark mass. To a good approximation they thus may be considered as massless. In this limit the Lagrangian, Eq.(1.1), possesses a global $U_L(n_f) \otimes U_R(n_f)$

symmetry for n_f massless quarks called chiral symmetry which is spontaneously broken to $U_V(1) \otimes U_A(1) \otimes SU_V(n_f)$. According to Noethers Theorem the chiral symmetry leads to conserved currents and suitably defined charges

$$\mathcal{J}_\mu(x) = \overline{\psi}(x)\gamma_\mu(T_D \otimes T_F)\psi(x) , \tag{1.15}$$

$$Q = \int \mathrm{d}^3x \ \overline{\psi}(x)\gamma_0(T_D \otimes T_F)\psi(x) . \tag{1.16}$$

where $T_D = \mathbb{1}, \gamma_5$ acts on the Dirac degrees of freedom, $T_F = \mathbb{1}_{n_f}, T_a$ acts on the flavor degrees of freedom. The T_a $(a = 1, \cdots, n_f^2 - 1)$ matrices are the generators of the $SU(n_f)$-group. The conservation of the $U_V(1)$ current implies the conservation of baryon number. This is the reason why the creation of a net baryon number present in the Universe can not be explained in the context of QCD.

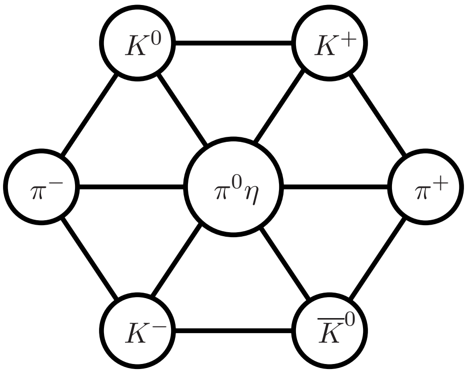

Figure 1.1: The lightest meson multiplet of the $SU_V(3)$ flavor symmetry group.

The $SU_V(n_f)$ gives rise to the mass degeneracy of hadronic states. For $n_f = 3$ this leads to Gell-Mann's eightfold way and the multiplet structure of the mesons $3 \otimes \overline{3} \rightarrow 8 \oplus 1$, depicted if Figure 1.1, and the hadrons $3 \otimes 3 \otimes 3 \rightarrow 10 \oplus 8 \oplus 8 \oplus 1$. For $n_f = 2$ one gets the usual isospin symmetry. Although the quark masses do not vanish exactly, these symmetries are still expected to be realized effectively and the corrections due to this effect are considered to be small.

In QCD the most explored global symmetries are the axial symmetries. The first one discussed here deals with the spontaneously broken subgroup of the chiral symmetry. This symmetry is, in contrast to the afore mentioned vector symmetry not realized at low temperatures. Another form of this statement is that the vector symmetries are realized in the Wigner Weyl mode whereas the broken subgroup is realized in the Nambu-Goldstone mode. If a symmetry is realized in the Nambu-Goldstone mode it produces $n^2 - 1$ massless Goldstone bosons for n spontaneously broken generators. For $n_f = 2$ one identifies the three pions $\pi^{\pm,0}$ as these Goldstone bosons of the broken symmetry. These broken operators applied to the vacuum create the Goldstone bosons

$$\langle 0|A_\mu(x)|\pi(p)\rangle = i f_\pi p_\mu e^{-ipx} \tag{1.17}$$

with the axial current $A_\mu = \overline{\psi}\gamma_\mu(\gamma_5 \otimes T_a)\psi$ and the pseudoscalar decay constant f_π. Taking the derivative yields the famous hypothesis of partial conservation of the axial current (PCAC)

$$\partial_\mu A_\mu = f_\pi m_\pi^2 P \tag{1.18}$$

with the pseudoscalar field $P = \overline{\psi}(\gamma_5 \otimes T_a)\psi$. The non-conservation of the axial current is induced by the finiteness of the quark mass m_q and the non-vanishing chiral condensate $\langle\overline{\psi}\psi\rangle$ via the Gell-Mann-Oakes-Renner relation[15]

$$f_\pi m_\pi^2 = -2m_q\langle\overline{\psi}\psi\rangle . \tag{1.19}$$

The last symmetry to be discussed here is the $U_A(1)$-symmetry which is broken too. However, this symmetry can not be realized in Nambu-Goldstone mode, because the corresponding Goldstone boson would be the η' with a mass of 960MeV which is not at all small in view of the hadronic scale of 1GeV. Indeed only the classical Lagrangian Eq.(1.9) possesses the $U_A(1)$ symmetry which gets broken explicitly by quantum effects. Hence this is called the $U_A(1)$ or Adler-Bell-Jackiw (ABJ) anomaly. If one computes the divergence of the appropriate flavor singlet axial current in the limit of vanishing quark masses one gets

$$\partial^\mu \mathcal{J}_{5\mu} \;=\; \partial^\mu \, \overline{\psi}\gamma_\mu(\mathbb{1}\otimes\gamma_5)\psi \;=\; n_f \frac{\alpha_s}{8\pi^2}\epsilon^{\mu\nu\rho\sigma}G^a_{\rho\sigma}G^a_{\mu\nu} \, , \tag{1.20}$$

where the right hand side is proportional to the topological charge density of the gluon field. Therefore topologically non trivial gauge field configurations break the $U_A(1)$ symmetry which in turn are responsible for the large mass of the η' meson due to the Witten-Veneziano mechanism[16, 17].

1.2.2 Phases of QCD at Finite Temperature

If the temperature increases, at some point it becomes the dominant scale in any physical process. Therefore one can discuss the phases of QCD by using only this scale.[1] A high temperature corresponds to a small length scale at which, as already mentioned, the quarks and gluons can effectively be described as free particles. The constituents in a system at these high temperatures form the so called Quark Gluon Plasma (QGP) and a phase transition between the low temperature phase with confinement and the QGP phase with liberated quarks and gluons is expected to exist. In the limit $m_q = \infty$ the order parameter for this phase transition is the Polyakov loop and which characterizes the behavior of the free energy between a static quark-antiquark pair at large distances. Only in the deconfined phase this energy is finite, and the Polyakov loop does not vanish.

It was mentioned that it is generally assumed that the $SU_A(n_f)$ symmetry is spontaneously broken. Thence a high temperature phase has to exist where this symmetry gets restored. At vanishing quark masses the order parameter is the chiral condensate which vanishes in the chirally symmetric high temperature phase. This transition can a priory be different from the deconfinement transition[18]. However, although the order of the transition depends on the number of quark flavors and their masses, both “transitions” always appear at the same temperature[19] and seem to be connected. The n_f dependence of the nature of the transition was conjectured by Pisarski and Wilczek[20] with the aid of the simpler σ model which shares the same global symmetries as QCD and leads to the phase diagram in the quark mass plane summarized in Fig. 1.2. In the pure gauge theory (pg) the transition is of first order and the deconfining phase transition occurs at a temperature of $T_c \simeq 270$MeV [21]. Decreasing quark masses weaken this transition and a line of a second order phase transitions occurs which falls into the three dimensional Ising universality class[22]. For two quark flavors the chiral symmetry restoration

---

[1] As already implicitly stated in the partition function, Eq.(1.7), a non-vanishing chemical potential is not considered throughout this work.

appears at vanishing quark masses (n2) and at a temperature $T_c \simeq 175$MeV [23]. This is a second order phase transition which is assumed to fall into the three dimensional $O(4)$ universality class[24]. This point is the endpoint of a line of second order phase transitions which on the other side ends at a strange quark mass m_s^{tr} in a tricritical point. Reducing the strange quark mass further leads to a first order phase transition. This region of first order phase transitions is bounded by a line which again falls into the three dimensional Ising universality class[25]. At the point of three massless quark flavors (n3), the critical temperature was determined to $T_c \simeq 155$MeV [23]. But for the majority of quark masses only a crossover between the different phases exists. Even for the physical quark masses the transition is expected to lie in this crossover regime (cross dashed region in Fig. 1.2), although this still require further clarification (See however [26]).

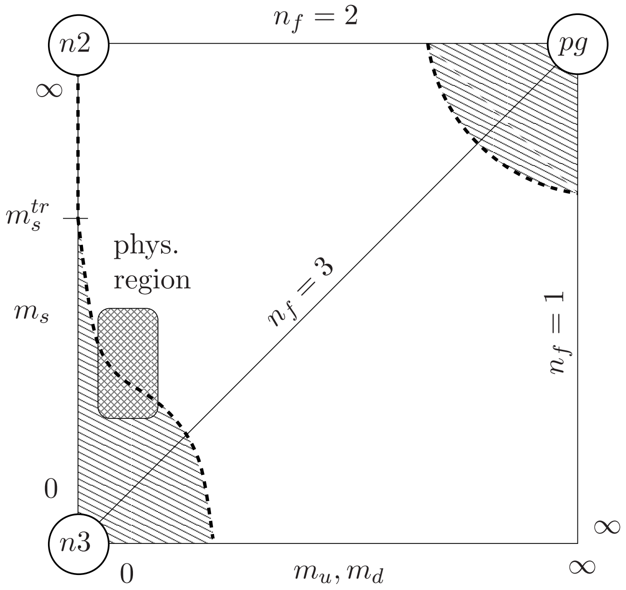

Figure 1.2: The phase diagram of QCD with $n_f = 2+1$ quark flavors in the quark mass plane.

At very high temperatures, quantum effects gets weaker and that is why one may expect an effective restoration of the $U_A(1)$ symmetry. If this happens at the same temperature at which chiral symmetry becomes restored, the order of the phase transition could be changed. The restoration of the different axial symmetries can be observed by analyzing the properties of the mesons, because some of them are related to each other by the corresponding symmetry transformation shown in Fig. 1.3, where two degenerate quark flavors are assumed for the moment. The π and δ susceptibilities, for instance, are then related to each other by the $U_A(1)$ symmetry whereas the π and the σ susceptibilities are sensible to the restoration of the $SUA(2)$ symmetry. These symmetries have been investigated in a lattice simulation[27] with staggered fermions by monitoring the temperature dependence of the inverse square of the susceptibilities, Eq.(2.60), which below T_c can be interpreted as the meson masses (see however Section 2.4.2). It shows indeed the expected degenerate pseudoscalar π and singlet scalar σ at the critical temperature for chiral symmetry restoration but the π and δ susceptibilities approach each other only very slowly and one can therefore conclude that the $U_A(1)$ is restored only at higher temperatures. This conclusion is in fact supported by other more recent lattice simulations[28, 29].

$$\begin{tikzcd}
\pi : \overline{\psi}\,(\gamma_5 \otimes T_a)\,\psi \arrow[r, leftrightarrow, "SU_A(2)"] \arrow[d, leftrightarrow, "U_A(1)"'] & \sigma : \overline{\psi}\,(\mathbb{1} \otimes \mathbb{1}_2)\,\psi \arrow[d, leftrightarrow, "U_A(1)"] \\
\delta : \overline{\psi}\,(\mathbb{1} \otimes T_a)\,\psi \arrow[r, leftrightarrow, "SU_A(2)"'] & \eta' : \overline{\psi}\,(\gamma_5 \otimes \mathbb{1}_2)\,\psi
\end{tikzcd}$$

(a)

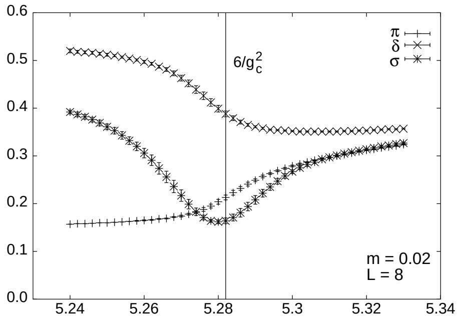

(b)

Figure 1.3: (a) The transformations which relate different particles in the chiral limit. (b) The temperature dependence of the square root of the inverse susceptibilities in different quantum number channels [27].

Chapter 2

Lattice QCD

> *Who can properly define and divide is to be considered a god*
>
> Plato

In this chapter the adaption of the continuum QCD to the lattice is discussed. The necessary steps can be found in text books[30] and in review articles[31, 32] and were first formulated by Wilson[33]:

- Discretization of space-time
- Transcription of the gauge and fermion fields
- Definition of the measure in the path integral
- Construction of the action
- Transcription of the operators to be computed.

In the following, these steps are described in more detail as for as it is needed to keep the further discussion self-containt. Moreover a short description of an efficient implementation is given. In the end some comments on the errors accompanying every lattice computation are given.

2.1 Discrete Space-time and the Gauge and Matter Fields

In the first step, the 4-dimensional Euclidean space-time has to be discretized which regularizes the theory. This discretization has to be removed afterwards, in order to obtain continuum physics again. The discussion of the continuum limit is left to Section 2.5. Here, only the regularization and the transcription of the different building blocks of QCD on the lattice are presented.

The starting point is an isotropic hypercubic lattice with spacing a and size $N_\sigma^3 \times N_\tau$. Such a lattice has a volume V and temperature T given by

$$V = (a\, N_\sigma)^3, \qquad T = \frac{1}{aN_\tau}. \tag{2.1}$$

At this point a has to be chosen large enough to ensure that the observed particle "fits" into the lattice. On the other hand, discretization effects grow with a and should be kept small. Thus considering a particle of mass m which has a correlation length of $\xi = 1/m$, a should obey the inequality

$$a \quad \ll \quad \xi \quad \ll \quad aN_\sigma\, . \tag{2.2}$$

The matter fields $\psi(x)$ are represented by anticommuting Grassmann variables defined at each site. Because the fermion action is linear in ψ and $\overline{\psi}$, the standard Grassmann integration rules can be used to integrate them out.
Consider for example the current $\mathcal{J}_H(x) = \overline{\psi}^{f_1}(x)\Gamma_H \psi^{f_2}(x)$ which describes a meson in the quantum number state H. It is selected by Γ_H which is an element of the Clifford algebra. The actual particle created by this operator is determined if the flavors f_i are fixed. Now the meson propagator can be computed by

$$\begin{aligned} \langle \mathcal{J}_H(x)\, \mathcal{J}_H^\dagger(0)\rangle_{\psi\overline{\psi}U} &= \frac{1}{Z}\int \mathrm{d}\psi \mathrm{d}\overline{\psi}\mathrm{d}U\; \overline{\psi}^{f_1}(x)\Gamma_H\psi^{f_2}(x) \left(\overline{\psi}^{f_1}(0)\Gamma_H\psi^{f_2}(0)\right)^\dagger e^{-\psi M\overline{\psi}-S_G} \\ &= \frac{1}{Z}\int \mathrm{d}U\;\; \det(M)\exp(-S_G)\Gamma_H\Gamma_H^\dagger \times \\ &\quad \times \left[M^{-1,f_1f_1}(x,0)M^{-1,f_2f_2}(0,x) - M^{-1,f_2f_1}(x,x)M^{-1,f_1f_2}(0,0)\right] \end{aligned} \tag{2.3}$$

with the fermion matrix $M = \gamma_\mu D_\mu - m_q$. In the quenched or valence quark approximation one neglects the determinant $\det(M) = 1$, which means that one considers the sea quarks as infinitely heavy and hence quark loops are suppressed. This approximation leads to a dramatic reduction of computing time in lattice gauge theory simulations and is therefore often used. This quenching effect in the light meson spectrum leads to a deviation from the experimental measured masses of at most 5% [34].

To implement the gauge fields one uses the fact that a fermion moving from the lattice site x in the direction $\hat{\mu}$ to the lattice site $x + \hat{\mu}$ picks up a phase factor given by

$$\psi(x+\hat{\mu}) \quad = \quad \exp\left(ig\int_x^{x+\hat{\mu}} A_\nu(z)\mathrm{d}z_\nu\right)\psi(x). \tag{2.4}$$

This is the reason why the gauge fields $A_\mu(x)$ are associated with the link that connects two sites. So, the gauge fields are implemented by a discrete version of the parallel transporter given in Eq.(2.4)

$$U_\mu(x) \quad = \quad e^{iag\, A_\mu(x+\frac{\hat{\mu}}{2})} \quad \simeq \quad 1 + iag\, A_\mu\left(x + \frac{\hat{\mu}}{2}\right) + \mathcal{O}(a^2g^2). \tag{2.5}$$

The integration over the gauge fields represented by elements of the compact $SU(3)$ can be defined with the Haar measure and a gauge fixing term is therefore not necessary for the computation of the path integral.

2.2 The Gauge Action

Having implemented the gauge and matter fields, in the way above described, the action has now to be formulated. The discretization of the field strength tensor is easily formulated with the smallest gauge invariant object on the lattice: the 1 × 1 Wilson loop

$$U_{\mu\nu}(x) \quad = \quad U_\mu(x) U_\nu(x+\hat{\mu}) U_{-\mu}(x+\hat{\nu}+\hat{\mu}) U_{-\nu}(x+\hat{\nu}) \ , \tag{2.6}$$

also called plaquette.

The plaquette is already sufficient to construct the gauge part of the action

$$S_G \quad = \quad \beta \sum_x \sum_{\mu,\nu}^{\mu<\nu} \left[1 - \frac{1}{3} \, \mathrm{Re} \ \mathrm{Tr} \ U_{\mu\nu}(x) \right] \tag{2.7}$$

which reproduces the continuum action already up to order $\mathcal{O}(a^2, \ a^2 g^2)$ as can be seen if one performs a Taylor expansion in the lattice spacing and the coupling. Here the conventional notation $\beta = 6/g^2$ is used. Using additional larger $n \times m$ Wilson loops reproduces the classical continuum action to higher orders in a^2. Quantum effects however induce $a^2 \rightarrow \mathcal{X}(g^2) a^2$ deviations from the continuum results with $\mathcal{X}(g^2) = 1 + c_1 g^2 + \cdots$ in lowest order perturbation theory. To correct these effects even non-planar loops with appropriately chosen weights between them have to be added to the action. This builds the framework of the so called Symanzik improvement scheme[35] described in Section 2.3.2. The disadvantage of such improved actions is the computational effort which rises with larger loops. Due to this and because other sources for deviations from the continuum are expected to be more important, only the simple Wilson plaquette gauge action Eq.(2.7) is used in this work.

2.3 The Fermion Action

After discretizing the gauge action, one also has to discretize the fermion action, Eq.(1.1), which is much more involved and several formulations are possible. This freedom can be chosen to improve some properties of the action. The most important improvements concern the number of doublers and the discretization of the derivative of the continuum fermion action. Special emphasis is put here on the Wilson action and its improvement, i.e., the Sheikholeslami-Wohlert action [36] which is used throughout Chapter 4.

The discussion of the discretization starts with the symmetrized version of the discrete derivative, $\partial\psi(x)$. Including the appropriate gauge fields to obtain a gauge invariant path of links bounded by the fermions one obtains

$$\overline{\psi}(x)\gamma_\mu D_\mu\psi(x) \simeq \frac{1}{2a}\overline{\psi}(x)\sum_\mu \gamma_\mu \Big[\, \overline{\psi}(x)U_\mu(x)\psi(x+\hat{\mu}) - \overline{\psi}(x)U^\dagger_\mu(x-\hat{\mu})\psi(x-\hat{\mu}) \,\Big] . \quad (2.8)$$

This leads to the most simple (so called "naive") discretized fermion action

$$\begin{aligned} S_F^N &= \sum_{x,y} \overline{\psi}(x) M^N_{x,y}[U]\psi(y) && (2.9) \\ M^N_{x,y}[U] &= m_q\delta_{x,y} + \frac{1}{2a}\sum_\mu \gamma_\mu \Big[\, U_\mu(x)\delta_{x+\hat{\mu},y} - U^\dagger_\mu(x-\hat{\mu})\delta_{x-\hat{\mu},y} \,\Big] && (2.10) \end{aligned}$$

with the naive fermion matrix M^N. This reproduces the continuum fermion action already to the same order as the gauge action and has the nice property to preserve the important chiral symmetry. But it leads to a the serious problem - the so called doubler problem. To investigate this consider the Fourier transformed version of the free ($g = 0$) quark action S_F^N

$$\begin{aligned} S_F^N &= \sum_k \overline{\psi}(k)\ (\Delta_q^N(k))^{-1}\ \psi(k) && (2.11) \\ \Delta^N(k) &= \frac{-i\gamma_4\sin(k_4)\ - i\mathcal{K} + m_q}{\sin^2(k_4) + \mathcal{K}^2 + m_q^2} && (2.12) \end{aligned}$$

with $\mathcal{K} = \sum_{i=1}^3 \gamma_i \sin(k_i)$, and $k_i = 2n_i\pi/N_\sigma$ with $0 \leq n_i < N_\sigma$ and $k_4 = (2n_4 + 1)\pi/N_\tau$ with $0 \leq n_4 < N_\tau$. The dispersion relation is given by the pole of the propagator Δ^N by setting $k_4 = iE_1/\pi + iE_2$. This results in the case of massless quarks to $\sinh(E_{1/2}(\mathbf{k})) = \sqrt{\mathcal{K}^2}$. Obviously the energy vanishes at every corner of the Brillouin zone $\mathbf{k} = (0,0,0), (\pi,0,0), \cdots, (\pi,\pi,\pi,)$, and therefore the action describes $2 \times 8 \times n_f$ different particles for n_f different quark flavors. These auxiliary particles do not disappear in the continuum limit. Additionally the naive fermion action has not the ABJ-anomaly of QCD described in Section 1.2. The doubler problem is typical for every lattice fermion action as stated in the no-go theorem by Nielsen-Ninomiya[37]. It excludes the possibility to define a local, translation invariant hermitian lattice action in 4-dimensions that preserves chiral symmetry and does not have doublers. Hence all lattice actions are a compromise between breaking chiral symmetry and allowing doublers, because local actions are mandatory for simulations.

2.3.1 The Wilson Action

In the construction of lattice actions one has the freedom to add an arbitrary number of irrelevant operators, as these do not change the continuum limit (see Section 2.5). Due to that, Wilson proposed to add the dimension-5 operator $\frac{r_\mu}{2}\ \sum_x \overline{\psi}(x)D_\mu^2\psi(x)$ with the

Wilson parameter $r_\mu = (r_\tau, r, r, r)$ to eliminate the unwanted doublers[1]. With this term the naive action changes to

$$\begin{aligned} S_F^W &= \sum_{x,y} \overline{\psi}(x) M^W_{x,y}[U] \psi(y) \ , && (2.13) \\ M^W_{x,y}[U] &= (m + 3r + r_\tau)\delta_{x,y} - && (2.14) \\ & \frac{1}{2} \sum_\mu (r_\mu - \gamma_\mu) U_\mu(x) \delta_{x+\hat{\mu},y} + (r_\mu + \gamma_\mu) U^\dagger_\mu(x-\hat{\mu}) \delta_{x-\hat{\mu},y} \ , \end{aligned}$$

where m is the quark mass parameter. Its connection to the physical quark mass becomes modified by interactions, as explained below. This reproduces the continuum action in the free case only up to $\mathcal{O}(a)$ but the advantage of adding this term lies in the doubler problem. To investigate this one has to compute again the free quark propagator in momentum space

$$\begin{aligned} \Delta^W(k) &= \frac{-i\gamma_4 \sin(k_4) \ - i\mathcal{K} + [r_\tau(1-\cos(k_4)) + \mathcal{M}]}{\sin^2(k_4) + \mathcal{K}^2 + [r_\tau(1 - cos(k_4)) + \mathcal{M}]^2} \ , && (2.15) \\ \mathcal{M} &= r \sum_{i=1}^{3} [1 - \cos(k_i)] + m^2. && (2.16) \end{aligned}$$

Now the search for poles of the propagator leads to two different solutions

$$\begin{aligned} \cosh(E_{+/-}(\mathbf{k})) &= \frac{\mathcal{U} \pm r_\tau(r_\tau + \mathcal{M})}{1 - r_\tau^2} \ , && (2.17) \\ \mathcal{U}^2 &= (1 + r_\tau\mathcal{M})^2 + (1 - r_\tau^2)(\mathcal{K}^2 + \mathcal{M}^2). && (2.18) \end{aligned}$$

This dispersion relation vanishes only in the limit $m, \mathbf{k} \to 0$, for $r \neq 0 \neq r_\tau$ which leads to $\cosh(E_{+/-}) = \frac{1 \pm r_\tau^2}{1 - r_\tau^2}$. If also the limit $r_\tau \to 1$ is taken the energy E_- vanishes and corresponds therefore to the continuum quark. The energy E_+, however, diverges in the continuum limit, i.e., gets an infinite mass. The generic choice for r is 1, because this opens some possibilities to save computing time (see Section 2.6) $r < 1$ may also used to improve different features of the action (see Section 3.3.2).[2] The values of the dispersion relation at the corner of the Brillouin zone are often interpreted as “doubler masses” so that $r \neq 0$ leads to a generation of a mass of order $\mathcal{O}(1/a)$ for the doublers, i.e. they become infinitely heavy in the continuum limit. In the light hadron sector and for values of a, usually used in the simulations, the doubler masses are essentially infinitely heavy and their contributions thus can be neglected. If one is interested in particles with heavy quarks this is, however, not obvious and has to be checked. Hence, at least for light quarks, the doubler problem seems to be solved (see Section 3.3.2 for more details) by the cost of an explicite breaking of chiral symmetry at $\mathcal{O}(a)$.

---

[1] Another fermion formulation, called staggered fermion discretization[38], reduces the 16 fermion doublers to 4. In this formulation, however, the one to one correspondence between the spin and flavor degrees of freedom on the lattice to the continuum one is lost and therefore no longer discussed.

[2] Not that $r_\mu \leq 1$ is necessary to maintain a reflection positivity to establish the existence of a positive semidefinite self-adjoint Hamiltonian[30].

To get the correct chiral limit in the continuum one eventually also has to redefine the observables. This can be achieved by demanding that the axial Ward identities

$$\left\langle \mathcal{J}\,\frac{\delta S_F^W}{\delta \phi}\right\rangle \;=\; \left\langle \frac{\delta \mathcal{J}}{\delta \phi}\right\rangle \tag{2.19}$$

are still valid. From this one can see that it is still possible to redefine the vector current in order to be conserved, but this is no longer true for the axial vector current, for which Eq.(2.19) leads to [39]

$$\langle \alpha|\nabla^\mu A_\mu|\beta\rangle \;=\; \langle \alpha|\overline{\psi}\{T_a,m\}\gamma_5\psi + X|\beta\rangle \tag{2.20}$$

for arbitrary states $|\alpha\rangle, |\beta\rangle$ and with the lattice derivative ∇ and

$$X \;=\; -\frac{r}{2}\sum_\mu \Big[\overline{\psi}(x)T_a\gamma_5 U_\mu(x)\psi(x+\mu) \;+\overline{\psi}(x+\mu)T_a\gamma_5 U_\mu^\dagger(x)\psi(x+\mu) \tag{2.21}$$

$$+\,(x\to x-\mu) \;-\; 4\overline{\psi}(x)T_a\gamma_5\psi(x)\Big]\;. \tag{2.22}$$

which is a dimension 5 operator for vanishing lattices spacing and therefore vanishes the continuum limit. Because of interactions X mixes, however, with operators of lower dimension and its vanishing can no longer be guaranteed. To analyze this one defines an operator X' by subtracting from X all allowed lower dimensional operators

$$X' \;=\; X + \overline{\psi}\{T_a,m'\}\gamma_5\psi \;+\; (Z_A-1)\nabla^\mu A_\mu \tag{2.23}$$

with the additional mass parameter m'. This operator is multiplicatively renormalizable and its matrix element vanishes in the continuum limit. Using Eq.(2.20) and (2.23) one obtains the continuum limit equation

$$\langle \alpha|\partial^\mu (Z_A A_\mu)|\beta\rangle \;=\; \langle \alpha|\overline{\psi}\{T_a,m_q\}\gamma_5\psi|\beta\rangle \tag{2.24}$$

with the new definition of the quark mass $m_q = m - m'$. Hence, the axial current is conserved only in the limit where m_q vanishes. The chiral limit corresponds to a m' value which depends on m and g and the mass parameter m has to be chosen such that it fulfill the condition $m_c = m'(m_c, g)$. This critical value has to be calculated numerically. With this mass, the matrix elements of the rescaled current $Z_A A_\mu$ correctly reproduce the continuum limit. Keeping the canonical form of the vector current one has to rescale it in complete analogy to the axial case with Z_V. This gives a conserved vector current.

Using $\langle\alpha| = \langle 0|,\;\; |\beta\rangle = |P(0)\rangle$ in Eq.(2.24) and integrating over space leads to

$$2m_q \;=\; \frac{\sum_{\mathbf{x}}\langle \partial_\mu (Z_A A_\mu(\mathbf{x},\tau))P^\dagger(0)\rangle}{\sum_{\mathbf{x}}\langle P(\mathbf{x},\tau)P^\dagger(0)\rangle}. \tag{2.25}$$

This can be used to compute the so called current quark mass. Another way to define the quark mass is obtained after rescaling the fields by $\psi \to \psi/\sqrt{2\kappa}$ with the hopping parameter $\kappa \equiv 1/(2m+8)$. Using κ one can define a bare quark mass by

$$m_q \;=\; \frac{1}{2\kappa} - \frac{1}{2\kappa_c}\;, \tag{2.26}$$

where κ_c is defined as the κ value at which the pion mass vanishes at zero temperature. In the free case $\kappa_c = 1/8$ leads to $m_q = m$. These definitions of the quark masses and therefore the value of m at which the chiral limit is reached can differ at order $\mathcal{O}(a)$. The computation of correlation functions as Eq.(2.3) requires the inversion of the fermion matrix M which is singular if it has a zero mode. But the values of m at which they occur are scattered around m_c at individual configurations because both methods to determine the quark mass rely on an averaging over different configurations to determine m_c. This is the origin of the problem with so called "exceptional configurations" which leads to strong fluctuations in the correlation functions and one has to specify how to deal with them.

The above considerations apply in the same way to the chiral condensate, which therefore also has to be modified to represent the correct order parameter. Since it is not used in this thesis it is not discussed any further. The necessary modifications can, however, be found also in[39].

2.3.2 Sheikholeslami-Wohlert Action and Symanzik Improvement

Symanzik[35] showed that lattice theories can be treated as effective low-energy continuum theories in which the dependence on the lattice spacing a can be is made explicit. The contributions to the full continuum theory from states with momenta $k > \pi/a$ which are absent on the lattice, have then to be "mimicked" by adding local terms to the action which are of higher dimension in a. This leads to an effective theory correct up to order $\mathcal{O}(a^n)$, if all local operators of dimension $n' \leq 4 + n$ are added to the action. From these operators only the ones which share the symmetries of the lattice action have to be taken into account. But operators with higher powers in a are still suppressed if a is small enough. This has been used by Sheikholeslami and Wohlert[36] to improve the Wilson action, Eq.(2.13), up to corrections of order $\mathcal{O}(a^2)$. For it all dimension 5 operators have to be used, and the equations of motion can be utilized to reduce their number. The remaining operators are

$$O_1 = \overline{\psi}\; i\sigma_{\mu\nu} G_{\mu\nu}\; \psi \tag{2.27}$$

$$O_2 = m \;\mathrm{Tr}\; G_{\mu\nu} G_{\mu\nu} \tag{2.28}$$

$$O_3 = m^2 \overline{\psi}\psi . \tag{2.29}$$

The operators Tr $G_{\mu\nu}G_{\mu\nu}$ and $\overline{\psi}\psi$ already appear in the Wilson action and $\mathcal{O}_{2,3}$ can be absorbed by a rescaling of the bare coupling and quark mass. For the improved action this results then in adding operator O_1

$$S_F^{SW} = S_F^W + a^5\, c_{SW} \sum_x \overline{\psi}(x)\, \frac{ig}{4} \sigma_{\mu\nu} G_{\mu\nu}(x)\, \psi(x)\; . \tag{2.30}$$

A symmetric definition of the lattice gluon field tensor is given by the sum over the four plaquettes around the point x

$$G_{\mu\nu}(x) = \frac{1}{8iga^2} \sum_j \left(U^j_{\mu\nu}(x) - U^{j\dagger}_{\mu\nu}(x) \right) . \tag{2.31}$$

The geometrical representation of this operator has the form of a clover which explains the often used name "clover action" for this improved action.

The parameter c_{SW} has to be chosen appropriately in order to remove the $\mathcal{O}(ga)$ errors completely. The determination of c_{sw} to be done non-perturbatively and was performed in quenched QCD[40] with the standard Wilson gauge action by imposing the PCAC relation to be valid up to $\mathcal{O}(a^2)$. The results for c_{SW} for different bare couplings g were found to be well fitted by

$$c_{SW} = \frac{1-0.656g^2-0.152g^4-0.054g^6}{1-0.922g^2} \qquad \text{for } 0 \leq g \leq 1. \tag{2.32}$$

The use of rescaled fields and $r_\mu = 1$ leads to the improved action implemented in the numerical calculations

$$\begin{aligned} S^{SW} &= \frac{1}{2\kappa}\sum_{x,y}\overline{\psi}(x)\ M^{SW}_{x,y}[U]\ \psi(y)\ , && (2.33)\\ M^{SW}_{x,y} &= A_x\delta_{x,y} + \kappa\Delta_{x,y}\ , && (2.34)\\ A_x &= \mathbb{1} - ig\ c_{SW}\ \frac{\kappa}{2}\sigma_{\mu\nu}G_{\mu\nu}(x)\ , && (2.35)\\ \Delta_{x,y} &= \frac{1}{2}\sum_\mu(\gamma_\mu - \mathbb{1})U_\mu(x)\delta_{x+\hat{\mu},y} - (\gamma_\mu + \mathbb{1})U^\dagger_\mu(x-\hat{\mu})\delta_{x-\hat{\mu},y}\ . && (2.36) \end{aligned}$$

Calculating correlation functions of local fields as, e.g., given in Eq.(2.3), one has to improve additionally the operators in the same way as it has been done for the action. This leads to the improved currents

$$\begin{aligned} A^I_\mu &= A_\mu +\ a\ c_A\tilde{\nabla}_\mu P\ , && (2.37)\\ V^I_\mu &= V_\mu +\ a\ c_V\tilde{\nabla}_\nu T_{\mu\nu}\ , && (2.38)\\ P^I = P \quad \text{and} \quad S^I &= S\ , && (2.39) \end{aligned}$$

with $\tilde{\nabla} = \frac{1}{2}(\nabla + \nabla^*)$ and the forward/backward lattice derivatives $\nabla/\nabla^* f(x) = \lim_{a\to 0} \pm(f(x\pm a) - f(x))/a$. The tensor current $T_{\mu\nu}$ is defined by $T_{\mu\nu} = \overline{\psi}\ (\sigma_{\mu\nu}\otimes\tau/2)\ \psi$. Again, the coefficient c_A has been evaluated non-perturbatively by[40]

$$c_A = -0.00756\ g^2 \times \frac{1-0.748\ g^2}{1-0.977\ g^2} \qquad \text{for } 0 \leq g \leq 1. \tag{2.40}$$

This can be used to correct Eq.(2.25) for the current quark mass, because all necessary current have been measured. In the pseudoscalar and scalar channel no improvement of this type is necessary. In the vector channel a non-perturbative study[41] found that the improvement factor c_V vanishes for $\beta \geq 6.4$ within errors. Therefore these improved currents are not considered here anymore.

To reduce cut-off effects further, a first possibility is to use higher derivatives. A systematic approach in this direction is made in [42] by investigating derivatives up to the sixth order. But to this order the only ghost free action remains the Wilson action. Another approach to improve Wilson fermions lies in the generalization of the Dirac operator D. This is used in the construction of "Perfect" actions[43] which can be found by locating the parameters on a renormalized trajectory emanating from the fixed point of the renormalization group transformations. It was soon realized that these fixed point actions are classically perfect actions[44]. They will be discussed in Section 3.2 in more detail. Other possibilities[45, 46, 47] try to fulfill the Ginsparg-Wilson[48] equation $\gamma_5 D + D\gamma_5 = a\gamma_5 D\gamma_5$. As these are numerically quite expensive they are not discussed here.

2.4 Correlation Functions on the Lattice

As in the continuum, information about hadron properties is obtained from their correlation function. First, a detailed explanation how reliable information can be extracted from the temporal meson correlation functions is presented. Then, the spatial correlation functions are introduced and their relation to the temporal correlation function is discussed.

2.4.1 Temporal Meson Correlation Functions

The thermal meson correlation function in coordinate space with Euclidian time $\tau \in [0, 1/T)$ is defined by

$$\begin{aligned} G_H(\tau, \mathbf{x}) &\equiv \langle\, \mathcal{J}_H(\tau, \mathbf{x})\, \mathcal{J}_H^\dagger(0, \mathbf{0})\, \rangle \\ &= \frac{1}{Z} \int \mathrm{d}U \;\; \Gamma_H M^{-1}(x, 0)\, \Gamma_H^\dagger M^{-1}(0, x)\;\; e^{-S_G}\;, \end{aligned} \tag{2.41}$$

where the second line represents Eq.(2.3) in the quenched approximation. Because only flavor nonsinglet channels are considered from now on, the contribution of the disconnected diagrams in the second term of Eq.(2.3) do not contribute. The connection between the correlation function and the spectral function σ_H is established through the momentum space correlation function $\hat{G}_H(i\omega_n, \mathbf{p})$ at the discrete Matsubara frequencies $\omega_n = 2\pi n T$ for bosons. It is related to $G_H(\tau, \mathbf{x})$ by

$$G_H(\tau, \mathbf{x}) \;=\; T \sum_{n=-\infty}^{+\infty} \int_{-\infty}^{\infty} \frac{\mathrm{d}^3 p}{(2\pi)^3}\, e^{-i\omega_n \tau + i\mathbf{p}\mathbf{x}}\, \hat{G}_H(i\omega_n, \mathbf{p}) \tag{2.42}$$

and to the spectral function by

$$\hat{G}_H(i\omega_n, \mathbf{p}) \;\equiv\; \int_{-\infty}^{\infty} \frac{\sigma_H(\omega, \mathbf{p}, T)}{\omega - i\omega_n}\, \mathrm{d}\omega. \tag{2.43}$$

Using the identity

$$T \sum_{n=-\infty}^{+\infty} \frac{e^{-i\omega_n \tau}}{\omega - i\omega_n} = \frac{e^{-\omega\tau}}{1 - e^{-\omega/T}}, \qquad 0 \le \tau < \frac{1}{T} \tag{2.44}$$

and the property of the SPF $\sigma(-\omega) = \sigma(\omega)$, the correlation function, projected to a fixed momentum $\mathbf{p}$, can then be written as

$$\begin{aligned} G_H(\tau, \mathbf{p}) &= T \sum_{n=-\infty}^{\infty} e^{-i\omega_n \tau} \hat{G}_H(i\omega_n, \mathbf{p}) \\ &= \int_0^\infty \mathrm{d}\omega \; \sigma_H(\omega, \mathbf{p}, T) \; K(\tau, \omega) \end{aligned} \tag{2.45}$$

with the finite temperature integration kernel $K(\tau, \omega)$

$$K(\tau, \omega) = \frac{\cosh(\omega(\tau - \frac{1}{2T}))}{\sinh(\frac{\omega}{2T})}. \tag{2.46}$$

In the limit $T \to 0$ the kernel takes the form $K(\tau, \omega) = \exp(-\omega\tau)$.

Consider now a zero temperature "pole+continuum" ansatz for the spectral function

$$\sigma_H(\omega, \mathbf{p}) \equiv |\langle O| \, \mathcal{J}_H \, |H(\mathbf{p})\rangle|^2 \;\; \mathrm{sgn}(\omega) \;\; \delta(\omega^2 - E_H^2(\mathbf{p})) \; + \; \sigma_c \omega^2 \Theta(\omega^2 - E_{H,c}^2(\mathbf{p})) \tag{2.47}$$

with the ground state energy $E_H = \sqrt{m_H^2 + \mathbf{p}^2}$. Generally one has a contribution from the continuum σ_c which starts at a threshold $E_{H,c}$ and is proportional to ω^2 by simple dimensional arguments. The correct form of the continuum contribution could be quite complicated, which, however, reaches due to asymptotic freedom the form given here. Such an ansatz is often used for QCD sum rules, phenomenologic parameterizations of experimental data[49] and to fit $T = 0$ lattice data[50]. The continuum term leads to an ultraviolet divergent correlation function for $\tau = 0, \frac{1}{T}$. At zero temperature the continuum contribution is suppressed for large τ with $\frac{1}{\tau} e^{-E_{H,c}\tau}$. Hence for low temperatures and large distances the correlation function is generally dominated by the pole contribution leading to

$$G_H(\tau, \mathbf{p}) = \frac{|\langle O| \, \mathcal{J}_H \, |H(\mathbf{p})\rangle|^2}{2E_H(\mathbf{p})} \frac{\cosh(E_H(\mathbf{p})(\tau - 1/2T))}{\sinh(E_H(\mathbf{p})/2T)}. \tag{2.48}$$

This ansatz is discussed for different channels in more detail below.

Pseudoscalar channel (P)

The current $\mathcal{J}_P = \overline{\psi}\gamma_5\psi$ projects onto the $J^{PC} = 0^{-+}$ state. In the case of a u and d quark this is the pion, which is the Goldstone particle of the spontaneously broken chiral symmetry. Hence the ground state mass should vanish in the chiral limit of zero quark mass according to the Gell-Mann-Oakes-Renner relation Eq.(1.19). The residue of this current at zero temperature is given by

$$\langle 0|\mathcal{J}_P|P(\mathbf{p})\rangle \;=\; f_P\,\frac{E_P^2(\mathbf{p})}{2m_q} \overset{\mathbf{p=0}}{=} f_P\frac{m_P^2}{2m_q} \tag{2.49}$$

with the pseudoscalar decay constant f_P. Lowest order perturbation theory leads to the continuum contribution $\sigma_c = \frac{3}{8\pi^2}$. The experimental values for the pion state at $T = 0$ are $f_P = 93\text{MeV}$, $m_P = 139\text{MeV}$ and $E_{P,c} = 1.3\text{GeV}$. Using Eq.(2.48) together with Eq.(2.49) leads to

$$G_P(\tau) \;=\; f_P^2\frac{m_P^3}{8m_q^2}\frac{\cosh(m_P(\tau - 1/2T))}{\sinh(m_P/2T)} \tag{2.50}$$

as an ansatz for the low temperature correlation function at vanishing momentum.

Vector channel (V)

The current $\mathcal{J}_{V,\mu} = \overline{\psi}\gamma_\mu\psi$ projects onto the $J^{PC} = 1^{--}$ state which is, for the two lightest quarks u and d, the ρ-meson. In this channel one has to take care of the polarization ϵ_μ of the vector channel

$$\langle 0|\mathcal{J}_{V,\mu}|V(\mathbf{p})\rangle \;=\; \frac{E_V^2(\mathbf{p})}{f_V}\epsilon_\mu. \tag{2.51}$$

Summing over the polarizations leads to

$$\sum_\mu |\langle 0|\mathcal{J}_{V,\mu}|V(\mathbf{p})\rangle|^2 \;=\; \frac{E_V^4(\mathbf{p})}{f_V^2}\xi(\mathbf{p}) \tag{2.52}$$

$$\xi(\mathbf{p}) \;=\; -\sum_\mu(g_{\mu\mu} - \frac{p_\mu^2}{p^2}) \overset{\mathbf{p=0}}{=} 3. \tag{2.53}$$

The continuum contribution at $T = 0$ is $\sigma_c = \frac{\xi}{4\pi^2}$ and is expected to start at $E_{V,c} = 1.6\text{GeV}$. The experimentally measured mass is $m_\rho = 770\text{MeV}$ and the decay constant is $f_\rho^{-1} = 0.2$. Vanishing momenta lead in this channel to the correlation function

$$G_V(\tau) \;=\; 3\,\frac{m_V^3}{2f_V^2}\frac{\cosh(m_V(\tau - 1/2T))}{\sinh(m_V/2T)}. \tag{2.54}$$

Axial Vector channel (A)

The current $\mathcal{J}_A = \sum_\mu \overline{\psi}\gamma_\mu\gamma_5\psi$ projects onto the $J^{PC} = 1^{++}$ state which is for the two lightest quarks the a_1 meson. For the temporal component it projects however on the

$J^{PC} = 0^{-+}$ state which are also the pion quantum numbers, but both states contribute with a different sign. This leads to an ansatz for the spectral function

$$\begin{aligned}\sigma_H(\omega, \mathbf{p}) \equiv & \quad |\langle O| \, \mathcal{J}_A \, |A(\mathbf{p})\rangle|^2 \;\; \delta(\omega^2 - E_A^2(\mathbf{p})) \\ & - \; |\langle O| \, \mathcal{J}_A \, |P(\mathbf{p})\rangle|^2 \;\; \delta(\omega^2 - E_P^2(\mathbf{p})) \\ & + \; \sigma_c \omega^2 \Theta(\omega^2 - E_{A,P,c}^2(\mathbf{p}))\end{aligned} \tag{2.55}$$

and the matrix element

$$\langle 0|\mathcal{J}_{A,\mu}|A_\mu(\mathbf{p})\rangle \;\; = \;\; \frac{E_A^2(\mathbf{p})}{f_A}\epsilon_\mu . \tag{2.56}$$

The experimentally measured mass for the a_1 is $m_{a_1} = 1230\text{GeV}$ and $f_{a_1} \simeq f_\rho$. This allows in principle a negative spectral function and one expects therefore also a negative correlation function at large distances which is dominated by the negative contribution of the lighter pion. This is taken into account in the fit ansatz discussed in the next section, Eq.(2.58). There the contribution of a second state is taken into account and the sign of this contribution is not specified. Therefore this ansatz would be appropriate also in this case and the correlation function at zero momentum, resulting from the pole only, is in analog to the vector case Eq.(2.54).

Scalar channel (S)

The current $\mathcal{J}_S = \overline{\psi}\psi$ projects onto the $J^{PC} = 0^{++}$ state. It is still questionary if such a state with light u and d quarks is realized in nature, although several candidates exist. If it is not then $\langle 0|\mathcal{J}_S|S(\mathbf{p})\rangle = 0$ which is consistent with the lattice calculation performed in[50, 51]. Its existence, however, seems to be experimentally established[13], but not much is known about this channel. Therefore the matrix element is not further specified and a general form of the ground state contribution is used

$$G_S(\tau) \;\; = \;\; \lambda_S \, \frac{\cosh(m_S(\tau - 1/2T))}{\sinh(m_S/2T)} . \tag{2.57}$$

2.4.2 Exploring temporal Correlation Functions

Additional contributions arising from excited states or cut-off effects, explained as bound states with the doubler quarks, can modify the structure of temporal correlation functions. These are taken into account here by modifying the ansatz used in the analysis of correlation functions. One tries to mimic these effects by adding an auxiliary bound state term to fit the correlation functions obtained in the simulations

$$G_H(\tau, \mathbf{p}) \;\; = \;\; \frac{|\langle O| \, \mathcal{J}_H \, |H(\mathbf{p})\rangle|^2}{2E_H(\mathbf{p})} \, \frac{\cosh(E_H(\mathbf{p})(\tau - 1/2T))}{\sinh(E_H(\mathbf{p})/2T)} + c \, \frac{\cosh(E'(\tau - 1/2T))}{\sinh(E'/2T)} . \tag{2.58}$$

This fitting ansatz relies on the assumption of large physical extent in the time direction in which the correlation function is dominated by the ground state peak. Only this makes it possible to extract the properties of this state. However, with increasing temperature the temporal extent shrinks and therefore this limit can in general not be reached. One way to increase the temperatures on isotropic lattices is to reduce the number of points N_τ which discretize the time like extent of the lattice. But reducing the data points makes it even more difficult to obtain a reliable fit of correlation functions. Another option is to keep N_τ fixed and decrease the time extent of the lattice by reducing the lattice spacing a. But in the same way the volume V of the system is decreased which can lead to large finite volume effects. The increase of N_σ to compensate this effect is limited by the computational effort. But this can partially be solved by introducing an anisotropic lattice, on which the spatial lattice spacing a_σ is larger than the temporal one, a, so that N_σ stays reasonably small while maintaining a sufficiently large volume. This approach is quite often followed in finite temperature lattice investigations[52, 53, 54]. The advantage of increasing N_τ at constant N_σ and V is the stability of the fits. However it comes with the price of the additional anisotropy $\xi = a_\sigma/a$ parameter, which has to be determined in additional simulations.

A first estimate of the meson masses can be obtained from the effective mass defined by

$$m_H^{eff}(\tau) \quad = \quad \log\left(\frac{G_H(\tau)}{G_H(\tau+1)}\right) \quad \overset{\tau\to\infty}{\longrightarrow} \quad m_H \ , \tag{2.59}$$

where for the second step the assumption $G_H(\tau) \propto e^{-m_H\tau}$ was made. In this observable the approach to the long range limit can be observed, i.e., the effective mass becomes independent of τ if the assumption is satisfied.

Another observable is the commonly used hadronic susceptibility

$$\chi_H \quad = \quad \int\limits_0^{1/T} G_H(\tau)\,\mathrm{d}\tau \quad = \quad 2\int\limits_0^{\infty} \frac{\sigma_H(\omega)}{\omega}\,\mathrm{d}\omega \ , \tag{2.60}$$

where the right hand side is obtained by using Eq.(2.45). Two features of the susceptibility are evident from this equation. One finds that $\chi_H \propto m_H^{-2}$ if $\sigma_H \propto \delta(\omega^2 - m_H^2)$. For this reason χ_H has been used as a measure of the particle mass. In general, however, one will find that χ_H is the ultraviolet divergent if the usual meson continuum contribution $\propto \omega^2$ is included in σ_H.

Another way of extracting the meson mass was proposed in[55] and is obtained by inserting the $T = 0$ spectral function ansatz, Eq.(2.47), in Eq.(2.45) for $\tau = 1/2T$ and $\mathbf{p} = \mathbf{0}$

$$G_H(\tau = 1/2T) \quad = \quad \frac{|\langle O|\ \mathcal{J}_H\ |H\rangle|^2}{2m_H \sinh(m_H/2T)} \ + \ \sigma_c\, T^3\, f(E_{H,c}) \ , \tag{2.61}$$

$$f(E_{H,c}) \ \equiv \ \int\limits_{E_{H,c}}^{\infty} \frac{\tilde{\omega}^2}{\sinh(\tilde{\omega}/2)}\,\mathrm{d}\tilde{\omega} \qquad\qquad (\tilde{\omega} \ \equiv \ \omega/T) \ , \tag{2.62}$$

$f(E_{H,c})$ is a strictly decreasing function starting from $f(0) \simeq 33.66$ at $E = 0$ to $f(\infty) = 0$ and is shown in Fig. 2.1. Using the matrix elements for the meson channels under

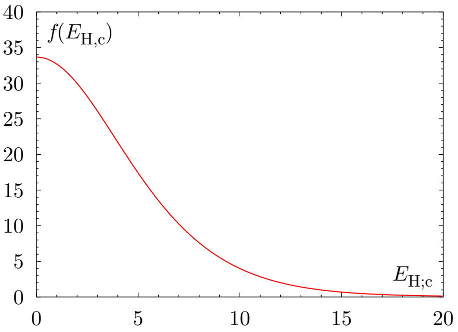

Figure 2.1: The function $f(E_{H,c})$.

consideration as given above and parameterizing the quark mass dependence of the remaining meson masses as known from chiral perturbation theory allows the extrapolation to the chiral limit and the determination of the meson masses and the decay constants in this limit. It has the advantage that $G_H(1/2T)$ is an ultraviolet save quantity and that it is almost independent of the continuum contribution. Problems occur at finite temperature when the $T = 0$ spectral function ansatz is no longer valid or when additional states produce a significant contribution even at the largest distance.

Improved Operators

Another method used improve the determination of hadron properties is to reduce the contributions from excited states. This leads to the construction of better projectors to the ground state. Several versions have been suggested, but all have in common the same idea. They all try to incorporate the finite extension of the mesons in the definition of the hadronic sources. One frequently used approach was developed in [56, 57] and is called fuzzing technique. Here the operator $\mathcal{J}_H = \overline{\psi}\gamma_H\psi$ is replaced by

$$\begin{aligned} J_H^R(x) &= \overline{\psi}^R(x)\Gamma_H\psi(x) && (2.63)\\ \psi^R(x) &= \frac{1}{6}\sum_{\mu=1}^{3} U_\mu^\dagger(x-\hat\mu)\cdots U_\mu^\dagger(x-R\hat\mu)\,\psi(x-R\hat\mu)\;+ \\ &\qquad U_\mu(x)\cdots U_\mu(x+(R-1)\hat\mu)\,\psi(x+R\hat\mu) && (2.64)\end{aligned}$$

and mimics a meson extent of the size Ra, symmetric in all space directions. In principle one can fuzz both operators in Eq.(2.41), but due to technical reasons (see Section 2.6) usually only the sink is fuzzed in this way, and the “correct” extent R has to be chosen in a way that the contributions from excited states are suppressed most effectively.

A more appropriate approximation may be given by sources which are exponentially smeared. Here the meson correlator

$$G_H(\tau,\mathbf{x}) \;=\; \iint \mathrm{d}y_1\mathrm{d}y_2\;\; w_1(y_1)\,w_2(y_2)\,\langle\mathcal{J}_H(\tau,\mathbf{x};\mathbf{y_1},0)\;\;\mathcal{J}_H(\mathbf{y_2},0;\mathbf{x},\tau)\rangle \quad (2.65)$$

is constructed from currents $\mathcal{J}_H(x;y) = \overline{\psi}(x)\Gamma_H\psi(y)$ which are weighted with the functions

$$w_1(y_1)w_2(y_2) = \begin{cases} \delta(\mathbf{y_1})\delta(\mathbf{y_2})\;, & \text{point-point(pp)}\\ \delta(\mathbf{y_1})e^{-a|\mathbf{y_2}|^b}\;, & \text{point-exp(pe)}\\ e^{-a|\mathbf{y_1}|^b}e^{-a|\mathbf{y_2}|^b}\;, & \text{exp-exp(ee)}\end{cases}\quad . \qquad (2.66)$$

Here a and b are free parameters which can be tuned to enhance the overlap with the ground state. The disadvantage of these operators is that they are no longer gauge invariant and hence require gauge fixing which enhances the computational effort. However, it may be advantageous to use them (see Section 3.3.3).

The signal can be further enhanced if the gauge fields are improved in addition. One possibility is the so called APE smearing procedure[58] and replaces the old links U^{old} by the new one U^{new} calculated with

$$\begin{aligned} U_\mu^{new}(x) &= \mathcal{P}_{SU(3)}\left(cU_\mu^{old}(x) + \sum_{\pm\nu\neq\mu<4} U_{\nu\mu}^{staple}(x)\right) && (2.67)\\ U_{\nu\mu}^{staple}(x) &= U_\nu^{old}(x)U_\mu^{old}(x+\nu)U_\nu^{old\dagger}(x+\mu). && (2.68)\end{aligned}$$

The notation $\mathcal{P}_{SU(3)}$ indicates the back projection to the $SU(3)$ group and c is an arbitrary parameter. For lattice cut-off similar to those used in our calculations, it was shown[57] that using $c = 2$ and iterating this procedure eight times is most effective.

Quark Mass

As already mentioned in Section 2.3.1, for $g \neq 0$ the quark mass is no longer directly related to the quark mass parameter κ in the theory. Hence the quark mass is an observable in the simulations with the Wilson action. Two ways to determine it have already been mentioned in this section and both suffer from $\mathcal{O}(a)$ corrections. However, it is easily possible to correct the definition of the current quark mass to $\mathcal{O}(a^2)$ by using the non-perturbatively improved currents introduced in Eq.(2.37) and (2.40). Additionally the signal can be improved by using only the fourth component of the axial current which has the largest overlap with the pion state. This leads to the ansatz

$$\frac{m_q}{Z_A} = \frac{1}{2}\,\frac{\sum_{\mathbf{x}}\langle\nabla_4 A_4(\mathbf{x},\tau)P^\dagger(0)\rangle + c_A \sum_{\mathbf{x}}\langle\nabla_4\nabla_4 P(\mathbf{x},\tau)P^\dagger(0)\rangle}{\sum_{\mathbf{x}}\langle P(\mathbf{x},\tau)P^\dagger(0)\rangle} \qquad (2.69)$$

to determine the quark mass.

2.4.3 Spatial Correlation Functions

One widely used method to extract information on meson properties at non-zero temperature is the usage of spatial correlators. They are obtained from Eq.(2.41) by an integration over the so called funny space which includes the Euclidian time and two spatial directions

$$G_H(\mathbf{p}_\perp, z, i\omega_n) = \int_0^{1/T} \mathrm{d}\tau \int_{-\infty}^{\infty}\int_{-\infty}^{\infty} \mathrm{d}x\,\mathrm{d}y\; e^{-i\mathbf{p}_\perp\mathbf{x}_\perp}e^{-i\omega_n\tau}G_H(\mathbf{x}_\perp, z, \tau)\,. \qquad (2.70)$$

with $\mathbf{x}_\perp = (x, y)$ and $\mathbf{p}_\perp = (p_x, p_y)$. The relation to the temporal correlation function is given again by the spectral function. At $T = 0$ it depends on p^2 only and is therefore independent on spatial or temporal direction interchanging. The parameters obtained from fits with Eq.(2.58) to $G_H(z)$ therefore should be the same as the one from the temporal ones. Hence masses, called screening masses, obtained from these coincide with the masses obtained from the temporal one, called pole masses. At finite temperature the time direction is distinguished as the direction of the four velocity of the heat bath, and the spectral function depends on p_0 and $\mathbf{p}$ separately. To investigate the influence of the heat bath consider again the $T = 0$ spectral function, Eq.(2.47), but now without the matrix element and neglecting the continuum contribution for simplicity. This leads to the free boson propagator in momentum space

$$G_H(i\omega_n, \mathbf{p}) = \frac{1}{\omega_n^2 + E_H^2(\mathbf{p})} \; . \tag{2.71}$$

To discuss the difference between screening and pole masses on the one hand and their relation to the spectral function on the other hand we will discus a simple example. Thermal effects may be modeled by a modified dispersion relation[59]

$$E_H^2(\mathbf{p}, T) \;=\; m_H^2 + \mathbf{p}^2 + \Pi(\mathbf{p}, T) \;=\; m_H^2(T) + A^2(T)\mathbf{p}^2 \tag{2.72}$$

with the vacuum polarization tensor $\Pi(\mathbf{p}, T)$. For the right hand side it is assumed that the temperature influence can be rewritten as a temperature dependent mass $m_H(T)$ and a coefficient $A(T)$ which might be different from 1 due to temperature modifications. This should be valid at least for low temperatures. Inserting this dispersion relation into Eq.(2.71) leads to

$$\begin{aligned} G_H(\mathbf{p}_\perp, z, i\omega_n) &= \int_{-\infty}^{\infty} \frac{\mathrm{d}p_z}{2\pi}\, e^{ip_z z}\, G_H(i\omega_n, \mathbf{p}) && (2.73) \\ &= \frac{1}{2\omega_z\, A^2(T)} e^{-\omega_z z} && (2.74) \end{aligned}$$

with

$$\begin{aligned} \omega_z^2 &= \frac{\omega_n^2}{A^2(T)} + {m_H^z}^2(T) + \mathbf{p}_\perp^2 \; , && (2.75) \\ m_H^z(T) &= m_H(T)/A(T) \; , && (2.76) \end{aligned}$$

the thermal screening mass $m_H^z(T)$. As one can see, one still obtains an exponentially decreasing correlation function. The exponential decay is controlled by the screening mass which coincides with the pole mass only if $A(T) \simeq 1$. If a bound state exists even above T_c, one still obtains an exponential fall off with a mass m_H^z. Once the bound state gets dissolved in the high temperature limit and quarks propagate freely in the medium one will get twice the lowest fermionic Matsubara frequency πT[60] as a screening mass characterizing the exponential fall off.

2.5 The Continuum Limit of Lattice QCD

The introduction of a finite lattice size regulates the theory, because it introduces an ultraviolet and infrared momentum cut-off $\frac{\pi}{N_\sigma a} \leq p_\mu \leq \frac{\pi}{a}$. The integrals are reduced thereby to finite sums and hence all quantities become finite. To obtain physical values, this regularization has to be removed. This is discussed in the following.

A consequence of the lattice regularization is the breaking of rotational, Lorentz and translational symmetries. Therefore one has to make sure that all of them get restored if the regulator a is removed, i.e., in the continuum limit $a \to 0, N_\tau \to \infty$ and in the thermodynamic limit $V \to \infty$, keeping simultaneously the physical parameters fixed. Divergencies which reappear during this procedure have to be absorbed into a redefinition of the parameters and couplings $m_q, g, \cdots$ of the theory. The continuum limit is reached by $g \to 0$ due to asymptotic freedom. At this fixed point the system becomes independent of the underlying microscopic properties. This phenomenon is called universality and ensures that the symmetries, broken by the discretization, become restored and all observables reach their continuum values. This is expressed in terms of the relation

$$\lim_{a\to 0} O(g(a),a) \;=\; \lim_{a \to 0} \left(\frac{1}{a}\right)^{d_O} \hat{O}(g(a),a) \;=\; O_{phys} \, , \tag{2.77}$$

where O is the lattice observable with dimension d_O and O_{phys} is the physical continuum observable. The independence of O with respect to a for small a leads to the renormalization group equation

$$\begin{aligned} 0 \;&=\; a\frac{d}{da} O(g(a),a) \qquad (2.78)\\ &=\; \left(a\frac{\partial}{\partial a} + \; a\frac{\partial g}{\partial a}\,\frac{\partial}{\partial g}\right) O(g(a),a) \qquad (2.79)\end{aligned}$$

which can be solved in the perturbative regime and leads to the β-function

$$\beta(g) \;\equiv\; -a\frac{\partial g}{\partial a} \;=\; -\beta_0 g^3 - \beta_1 g^5 - \mathcal{O}(g^7) \, . \tag{2.80}$$

The solution of the differential equation is

$$\begin{aligned} g^{-2}(a) \;&=\; \beta_0 \log\left(\frac{1}{a\Lambda_{lat}}\right)^2 + \frac{\beta_1}{\beta_0}\log\log\left(\frac{1}{a\Lambda_{lat}}\right)^2 \, , \qquad (2.81)\\ \beta_0 \;&=\; \frac{1}{16\pi^2}\left(11 - \frac{2}{3}n_f\right) \overset{n_f=0}{=} \frac{11}{16\pi^2} \, , \qquad (2.82)\\ \beta_1 \;&=\; \frac{1}{256\pi^4}\left(102 - \frac{38}{3}n_f\right) \overset{n_f=0}{=} \frac{51}{128\pi^4} \qquad (2.83)\end{aligned}$$

with the only two renormalization scheme independent coefficients β_0 and β_1 and the integration parameter of the differential equation (2.80), Λ, which depends on the renormalization scheme. Inverting Eq.(2.81) gives the usual result

$$f(g^2) \;\equiv\; a\Lambda \;=\; (\beta_0 g^2)^{-\frac{\beta_1}{2\beta_0^2}} \exp\left\{-\frac{1}{2\beta_0 g^2}\right\} \, . \tag{2.84}$$

Eq.(2.77) can also be used to determine the physical scale a for given g^2 at finite temperature by relating, e.g., the experimentally known value of the string tension $\sqrt{\sigma}$ to the numerical value of the string tension calculated on the lattice, $\sqrt{\hat{\sigma}}$ at $T = 0$, at the same g^2

$$\frac{1}{a}\sqrt{\hat{\sigma}} \quad = \quad \sqrt{\sigma} \quad = \quad 420\text{MeV} . \tag{2.85}$$

The advantage of taking the string tension to set the scale is that it is insensitive to the quark mass which in principle can induce another scale. In the non-asymptotic regime the finite lattice cut-off leads to modifications of Eq. 2.78, i.e., $a\frac{d}{da}O(g(a), a) = f(O, a)$. The scaling violations $f(0, a) \neq 0$ depend on the observable O and the lattice spacing a. They can be reduced by using small a and/or using the improvement techniques described in Section 2.3.2.

2.6 Errors and Numerical Implementation

In this Section, we will be explained why the above described simulation of QCD is challenging and explain some details of the implementation to save computing time. In the end we discuss the role of limited statistics and the error estimate.

The computation of the thermal average $\langle \cdots \rangle$ in Eq.(2.41) requires the computation of an integral with dimension $\mathcal{O}(10^6)$. The only useful integration method for such high dimensional integrals is the Monte Carlo integration. This method consists in generating gauge field configurations to build a Markov chain of configurations $\{U_i\}_{i=0}^N$ from which one gets the required expectation value of any observable $\langle O \rangle$ by

$$\langle O \rangle \quad = \quad \lim_{N\to\infty} \frac{1}{N} \sum_{i=0}^{N} O[U_i] . \tag{2.86}$$

Because the available computer time is limited, one wants to generate the configurations already according to their Boltzmann weight $\exp(-S_G[U])$ to ensure that only configurations appear in the Markov chain which predominantly contribute to the path integral. This is called importance sampling and is achieved by constructing an appropriate transition probability $P(U \to U')$ between two consecutive configurations. This probability has to fulfill the detailed balance condition

$$\exp(-S_G[U])P(U \to U') \quad = \quad \exp(-S_G[U'])P(U' \to U) \tag{2.87}$$

to ensure that the configuration approaches the phase space region belonging to the thermal equilibrium of the system. Additionally the probability distribution has to be ergodic, i.e., $P(U \to U')$ has to be finite for every configuration pair U and U' in order to produce the correct average. In our work a local pseudo-heatbath algorithm[61, 62] has been used to generate a new configuration after one sweep over the lattice. To reduce the autocorrelation time of the Markov chain 5 overrelaxation steps[63, 64] have been performed between every heatbath update.

The most time consuming part in the study of hadron correlation functions is the calculation of the inverse fermion matrix $M(x, y)$. It is a huge but sparse matrix and its inversion is done with a point like source and using the Conjugate Gradient[65] or BiCGstab[66] algorithm. The first method is applied to the $T > T_c$ calculations and guarantees the convergence for an $N \times N$ matrix in N iterations. The second algorithm is supposed to work for small quark masses faster than the former one[67] and is therefore applied in the $T < T_c$ runs. Convergence of both algorithms depends on the ratio of the largest to the smallest eigenvalue of the fermion matrix which approaches infinity if $\kappa \rightarrow \kappa_c$ below T_c, i.e., if a zero mode exists. Hence the computational effort of these algorithms rises for decreasing quark mass and one is limited to use rather large quark masses below T_c. Above T_c no zero mode exists and simulations at the critical quark mass become feasible. The inversion can be accelerated using the even-odd preconditioning technique[68]. Another acceleration can be used if $r = 1$. Due to this, the terms $\frac{r-\gamma_\mu}{2}$ appearing in Eq.(2.13) are projectors of rank 2 which allows to rewrite the four spinors ψ as two spinors. This can also be used to safe computing time in the Matrix inversion routine[69]. Another simplification is given by the hermiticity property

$$\gamma_5 M(x, 0)\gamma_5 \quad = \quad M^\dagger(0, x) \tag{2.88}$$

which allows to avoid the inversion of both fermion matrices $M(x, 0)$ and $M(0, x)$ appearing in Eq.(2.41). If one restricts the fuzzing to the sink operator (see Section 2.4.2), this improvement can be used with small computational overhead.

Every computer simulation suffers from different sources of systematic and statistical errors due to limited computer power and time. The systematic errors which still have to be taken into account are the quenched approximation, finite size effects and scaling violations. Most of them have already been mentioned and strategies to avoid or to minimize them have been discussed. Their influence on the calculated observables will be incorporated in the discussion of the results of the simulations. Therefore, only statistical errors are discussed here.

Statistical errors are unavoidable and appear due to a limited sample of configurations. Moreover, the N configurations $\{U_i\}_{i=1}^{N}$, as well as the observable $O[U_i]$ calculated on them, are not statistically independent so that a naive error estimate would be misleading. Therefore the jackknife method is applied. For this method one first computes the naive average

$$O_N = \frac{1}{N} \sum_{i=1}^{N} O[U_i] \tag{2.89}$$

and then divides the N data in n blocks with the same number of data N'. Out of these n new data sets are created by leaving out one block at a time. On this one computes the new estimators $\{O_k\}_{k=1}^{n}$ and their average O_n. With these one gets a less biased estimator $\hat{O}$ for $\langle O \rangle$ by

$$\hat{O} \quad = \quad nO_N - (n-1)O_n \tag{2.90}$$

$$\delta\hat{O}^2 \quad = \quad \frac{n-1}{n} \sum_{k=1}^{n} (O_k - O_n)^2 \tag{2.91}$$

and a reliable error estimate $\delta\hat{O}$.

Once the d_o observables $\{O_a\}_{a=1}^{d_o}$ and their errors $\{\delta O_a\}_{a=1}^{d_o}$ are calculated, one tries to fit a model motivated function $F(P)$ with the parameter set $\{P\}_{p=1}^{d_p}$ with d_p parameters to them, e.g., the correlation function with Eq.(2.58). This can be done by minimizing the $\chi^2(P)$ function

$$\chi^2(P) = \sum_{a,b=1}^{d_o} \{F(P) - O_a\}\, C_{ab}^{-1}\, \{F(P) - O_b\}\ , \tag{2.92}$$

$$C_{ab} = \frac{1}{N(N-1)} \sum_{i=1}^{N} \{O_a[U_i] - O_a\}\{O_b[U_i] - O_b\}\ , \tag{2.93}$$

where the covariance matrix C_{ab} in its off-diagonal elements includes possible correlations between the data. One often neglects these correlations, and take into account only the diagonal components, $C_{aa} = \delta O_a^2$. The inversion of the covariance matrix suffers from the problem of largely different eigenvalues. A way out of this problem was proposed in[70] by averaging the small eigenvalues and leaving the large ones unchanged. Consider for example that the d_o eigenvalues λ_a of the covariance matrix are ordered $\lambda_a \leq \lambda_{a+1}$ and that at most d_r are supposed to be too small. Then one uses the new eigenvalues

$$\lambda_i' = \max(\lambda_i, \overline{\lambda}) \tag{2.94}$$

$$\overline{\lambda} = \frac{1}{d_r} \sum_{a=1}^{d_r} \lambda_a \tag{2.95}$$

which means that one retains at least $d_o - d_r + 1$ eigenvalues. This method is frequently used in the maximum entropy method introduced in Section 4.4.1.

Chapter 3

Spectral Functions in the Infinite Temperature Limit

> *Although this may seem a paradox, all exact science is dominated by the idea of approximation.*
>
> Bertrand Russell

In this chapter cut-off effects of the lattice formulation at lowest order perturbation theory, i.e., in the limit $g = 0$ or infinite temperature, are investigated[1]. First results on continuum spectral and correlation functions are reviewed and then an explicit calculation with discretized fermion actions is presented. All calculations in this direction start with the determination of the free quark propagator $S_F(k)$ in momentum space. The second step is the Fourier transform $S_F(k_0, \mathbf{k}) \to S_F(\tau, \mathbf{k})$, which is then inserted into the expression for the meson correlation function

$$G_H(\tau) = \int\limits_{-\infty}^{\infty} \mathrm{d}^3k \;\; \gamma_5 \Gamma_H S_F(\tau, \mathbf{k}) \Gamma_H^\dagger \gamma_5 S_F^\dagger(\tau, \mathbf{k}) \; . \tag{3.1}$$

The last step is to rewrite this expression into a representation containing the spectral function $\sigma_H(\omega)$ and an integration kernel $K(\omega, \tau)$

$$G_H(\tau) = \int_0^\infty \mathrm{d}\omega \; \sigma_H(\omega) \; K(\omega, \tau) \; . \tag{3.2}$$

In principle $K(\omega, \tau)$ could also contain some cut-off effects. This was assumed in former applications of the Maximum Entropy Method [12, 72], explained in Chapter 4.4.1, to reduce the cut-off effects in the reconstructed spectral functions. The analysis presented

---

[1] The main results of this chapter have been summarized in [71].

in this chapter, however, will lead to the conclusion that in the considered limit all cut-off effects are contained in the spectral functions whereas the integration Kernel K keeps its continuum form, Eq.(2.46).

The above described steps are followed first for the Wilson action, Eq.(2.13), generalized to the case of anisotropic lattices, and then for a "perfect action" truncated to a single hypercube [73, 43]. At the end a discussion of the cut-off effects in the correlation functions as well as in the spectral functions will be presented. In this chapter only correlation functions projected to zero meson momentum are considered, hence no $\mathbf{p}$ dependence is specified.

3.1 Free Wilson Fermions on the Lattice

To discuss cut-off effects in different fermion formulations, one has to compare them with the exact free continuum quantities, the meson spectral function (SPF) $\sigma_H^{cont}(\omega)$, and the thermal two-point function $G_H(\tau)$. After these functions are obtained, their calculation within the Wilson formulation is presented. The comparison between them is devoted to Section 3.3.

3.1.1 Continuum Correlation and Spectral Function

The computation of the continuum function starts with the free fermion spectral function $\sigma_F(k_0,\mathbf{k})$ and the free fermion propagator $S_F(i\omega_n,\mathbf{k})$ in momentum space

$$\sigma_F(k) = 2\pi\,\mathrm{sgn}(k_0)\,[k_\mu\gamma_\mu + m_q]\,\delta(k^2-m_q^2) \tag{3.3}$$

$$S_F(i\omega_n,\mathbf{k}) = \int\limits_{-\infty}^{\infty}\frac{\mathrm{d}k_0}{2\pi}\,\frac{\sigma_F(k_0,\mathbf{k})}{i\omega_n - k_0} \tag{3.4}$$

with the fermionic Matsubara frequencies $\omega_n=(2n+1)\pi T$. With them, one obtains the meson spectral function as the imaginary part of the mesonic momentum space correlator

$$\sigma_H^{cont}(\omega) = \frac{1}{\pi}\,\mathrm{Im}\;T\sum_{n=-\infty}^{\infty}\iiint\limits_{-\infty}^{\infty}\frac{\mathrm{d}^3k}{(2\pi)^3}\;\mathrm{Tr}\,[\gamma_5\Gamma_H\,S_F(i\omega_n,\mathbf{k})\,\Gamma_H^\dagger\gamma_5\,S_F(i\omega_n-\omega,\mathbf{k})]\;, \tag{3.5}$$

which leads to[74]

$$\sigma_H^{cont}(\omega) = \frac{N_c}{8\pi^2}\,\Theta(\omega-2m_q)\,\omega^2\tanh(\omega/4T)\sqrt{1-\left(\frac{2m_q}{\omega}\right)^2}\,\times \left(a_H + b_H\left(\frac{2m_q}{\omega}\right)^2\right) + \frac{N_c}{3}\frac{T^2}{2}f_H\,\omega\,\delta(\omega). \tag{3.6}$$

The factors a_H, b_H and f_H, introduced here, are given for different quantum number channels in Table 3.1. In the chiral and $\omega \to \infty$ limit, this leads to the continuum constants σ_c for the SPF as introduced in Section 2.4. The continuum correlation function for the pseudoscalar case in the chiral limit can be obtained from this SPF by using Eq.(3.2)

$$\frac{G_P^c(\tau T)}{T^3} = \pi N_c(1-2\tau T)\frac{1+\cos^2(2\pi\tau T)}{\sin^3(2\pi\tau T)} + 2N_c\frac{\cos(2\pi\tau T)}{\sin^2(2\pi\tau T)} , \tag{3.7}$$

where G_P^c is rescaled with the temperature to obtain a dimensionless quantity and N_c are the color degrees of freedom. As in the high temperature limit T is the only relevant scale, this will be done in this chapter for all quantities with a nontrivial dimension. The relevant ones are

$$\omega \to \tilde{\omega} = \frac{\omega}{T} \quad \sigma \to \tilde{\sigma} = \frac{\sigma}{T^2} \quad G_H \to \tilde{G}_H = \frac{G_H}{T^3} \quad \tau \to \tilde{\tau} = \tau T \tag{3.8}$$

$$K \to \tilde{K} = \cosh(\tilde{\omega}(\tilde{\tau}-1/2))/\sinh(\tilde{\omega}/2). \tag{3.9}$$

For the discussion of the cut-off dependence it is however often useful to maintain the explicit temperature dependence of the distance, i.e., the notation τT.

3.1.2 Free Wilson Correlation Function

The starting point for our discussion of cut-off effects is the Wilson fermion action in momentum space Eq.(2.15). As already pointed out, for finite temperature lattice calculations anisotropic actions are often used, in order to get access to the temporal correlation function at a larger number of grid points N_τ while keeping volume and temperature constant. Thus, the generalization of Eq.(2.15) to an anisotropic lattice $\xi = a/a_\tau \geq 1$ is desirable and leads to the propagator for Wilson fermions

$$\Delta^W(k) = \frac{-i\gamma_4\sin(k_4) - i\mathcal{K} + [r_\tau(1-\cos(k_4)) + \mathcal{M}]}{\sin^2(k_4) + \mathcal{K}^2 + [r_\tau(1-\cos(k_4)) + \mathcal{M}]^2} , \tag{3.10}$$

$$\mathcal{M} = \frac{1}{\xi}\left[r\sum_{i=1}^{3}(1-\cos(k_i)) + m_q\right] , \tag{3.11}$$

$$\mathcal{K} = \frac{1}{\xi}\sum_{i=1}^{3}\gamma_i\sin(k_i) , \tag{3.12}$$

with, for the moment, arbitrary r and r_τ. The dispersion relation is defined by the two poles $k_4 = iE_-$ and $k_4 = \pi + iE_+$ of the propagator

$$\cosh(E_\pm(\mathbf{k})) = \frac{\mathcal{U} \pm r_\tau(r_\tau + \mathcal{M})}{1 - r_\tau} \tag{3.13}$$

$$\mathcal{U}^2 = (1 + r_\tau\mathcal{M})^2 + (1 - r_\tau^2)(\mathcal{K}^2 + \mathcal{M}^2) .$$

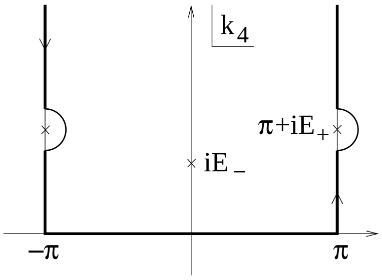

Figure 3.1: Integration contour in the complex k_4 plane.

As already mentioned, the first step is to derive an analytic expression for the quark propagator $S^W(\tau, \mathbf{k})$. This is done by analytic continuation of $\Delta^W(k)$ for k_4 and by taking the limit $N_\tau \to \infty$. This allows to compute the Fourier transform of the quark propagator

$$S^W_\infty(\tau,\mathbf{k}) \quad = \quad \int\limits_{-\pi}^{\pi} \frac{\mathrm{d}k_4}{2\pi}\ \Delta^W(k)\, e^{ik_4\tau} \tag{3.14}$$

analytically[75] by an integration over the contour shown in Fig. 3.1. In the next step one takes the limit $r_\tau \to 1$ in order to eliminate the ghost branch as discussed in Section 2.3.1 which changes the dispersion relation to

$$\cosh E_- \quad = \quad 1 + \frac{\mathcal{K}^2+\mathcal{M}^2}{2(1+\mathcal{M})}, \qquad E_+ \to \infty. \tag{3.15}$$

Therefore only the first pole has to be considered from now on and the index can be omitted. Returning now to finite N_τ and using the identities given in Appendix B leads to the desired form of the quark propagator[2]

$$\begin{aligned} S^W(\tau,\mathbf{k}) \quad &= \quad \sum_{m=-\infty}^{\infty} (-1)^{|m|} S^W_\infty(\tau+m,\mathbf{k}) & (3.16)\\ &= \quad \sum_{i=1}^{3} \frac{i\sin k_i}{2(1+\mathcal{M})\sinh E}\ \frac{\sinh[E(\mathbf{k})(\tau T-1/2)]}{\cosh(E/2T)}\,\gamma_i & (3.17)\\ &\quad + \frac{\sinh E}{2(1+\mathcal{M})\sinh E}\ \frac{\cosh[E(\mathbf{k})(\tau T-1/2)]}{\cosh(E/2T)}\,\gamma_4 \\ &\quad + \frac{1-\cosh E+\mathcal{M}}{2(1+\mathcal{M})\sinh E}\ \frac{\sinh[E(\mathbf{k})(\tau T-1/2)]}{\cosh(E/2T)}\,\mathbb{1}\,. \end{aligned}$$

This can be used to obtain the analytic expression for the meson correlation function

$$\begin{aligned} \tilde{G}^W_H(\tau T) \quad &= \quad N_c \left(\frac{N_\tau}{\xi N_\sigma}\right)^3 \sum_{\mathbf{k}}\ \mathrm{Tr}\ \left[\gamma_5\Gamma_H S^W(\tau,\mathbf{k})\Gamma^\dagger_H\gamma_5 S^{W\dagger}(\tau,\mathbf{k})\right] & (3.18)\\ &= \quad N_c \left(\frac{N_\tau}{\xi N_\sigma}\right)^3 \sum_{\mathbf{k}} \frac{c^W_H(\mathbf{k})\cosh[2E(\mathbf{k})N_\tau(\tau T-1/2)]+d^W_H(\mathbf{k})}{(1+\mathcal{M})^2\cosh^2(E(\mathbf{k})/2T)}\,, & (3.19) \end{aligned}$$

and the coefficients

$$\begin{aligned} c^W_H &= \frac{1}{2}\left[T^H_4 + \frac{\sum_i T^H_i \sin^2 k_i}{\sinh^2 E} + T^H_u - T^H_u \frac{\mathcal{K}^2}{\sinh^2 E}\right]\,, & (3.20)\\ d^W_H &= \frac{1}{2}\left[T^H_4 + \frac{\sum_i T^H_i \sin^2 k_i}{\sinh^2 E} - T^H_u + T^H_u \frac{\mathcal{K}^2}{\sinh^2 E}\right]\,, & (3.21) \end{aligned}$$

are given with

$$T^H_\mu \quad = \quad \frac{1}{4}\mathrm{Tr}\left[\Gamma_H\gamma_\mu\Gamma^\dagger_H\gamma_5\gamma_\mu\gamma_5\right], \qquad T^H_u \quad = \quad \frac{1}{4}\mathrm{Tr}[\Gamma_H\Gamma^\dagger_H]\,. \tag{3.22}$$

---

[2] Here the contact term[75] appearing due to a remanent E_2 contribution, which is proportional to $\delta(\tau)$, is neglected.

H	a_H	b_H	f_H	c_H^W	d_H^W	c_H^{FP}	d_H^{FP}
P	1	0	0	1	0	δ^2	0
S	-1	1	0	$-d^W$	d^W-1	$-d^{FP}$	$d^{FP}-\delta^2$
$\sum_{i=1}^{3} V_i$	2	1	1	$3-d^W$	d^W	$3\delta^2-d^{FP}$	d^{FP}
V_4	0	0	-1	0	-1	0	$-\delta^2$
$V \equiv \sum_{\mu=0}^{3} V_\mu$	2	1	0	$3-d^W$	d^W-1	$3\delta^2-d^{FP}$	$d^{FP}-\delta^2$
$\sum_{i=1}^{3} A_i$	-2	3	-1	-2d^W	2d^W-3	$-2d^{FP}$	$d^{FP}-\delta^2$
A_4	0	0	1	$1-d^W$	d^W	δ^2-d^{FP}	d^{FP}
$A \equiv \sum_{\mu=0}^{3} A_\mu$	-2	3	0	1-3d^W	3(d^W-1)	δ^2-3d^{FP}	$3(d^{FP}-\delta^2)$

Table 3.1: The coefficients a_H, b_H and f_H for the free continuum spectral functions σ_H^{cont} and the coefficients c_H and d_H for the Wilson correlation function, Eq.(3.19), and the corresponding ones for the FP action, Eq.(3.48).

With the abbreviation

$$d^W(\mathbf{k}) \quad = \quad \frac{\mathcal{K}^2}{\sinh^2 E} \tag{3.23}$$

these parameter can be evaluated with Table 3.1. Note that $\sinh^2 E \rightarrow \mathcal{K}^2$ in the continuum limit. Thus d^W approaches one for massless quarks.

3.1.3 Free Wilson Spectral Function

Once the analytic quark propagators and meson propagators are known, Eq.(3.2) can be utilized to compute the spectral functions. To do this, one has to reduce the three dimensional momentum integral to a one dimensional energy integral. The first step in this direction is to split the correlation function, Eq.(3.19), into two independent parts, arising from the two contributions to c_H^W listed in Table 3.2

$$\tilde{G}_1(\tau T) \quad = \quad N_c \left(\frac{N_\tau}{\xi}\right)^3 \int \mathrm{d}^3k \, \frac{1}{(1+\mathcal{M})^2} \frac{\cosh[2E(\mathbf{k})N_\tau(\tau T-1/2)]}{\cosh^2(E(\mathbf{k})N_\tau/2)} \ , \tag{3.24}$$

$$\tilde{G}_2(\tau T) \quad = \quad N_c \left(\frac{N_\tau}{\xi}\right)^3 \int \mathrm{d}^3k \, \frac{d^W(\mathbf{k})}{(1+\mathcal{M})^2} \frac{\cosh[2E(\mathbf{k})N_\tau(\tau T-1/2)]}{\cosh^2(E(\mathbf{k})N_\tau/2)} \ . \tag{3.25}$$

From this one can get meson correlation functions for the different channels as appropriate linear combinations of $\tilde{G}_1$ and $\tilde{G}_2$. Here we take the τ dependent terms only, because the

τ independent term constructed from d_H^W, leads to an independent delta contribution at vanishing frequency $f_H^W \delta(\omega)$ with

$$f_H^W = N_c \left(\frac{N_\tau}{\xi}\right)^3 \int \mathrm{d}^3k \, \frac{d_H^W(\mathbf{k})}{(1+\mathcal{M})^2} \frac{1}{\cosh^2(E(\mathbf{k})N_\tau/2)} \, . \tag{3.26}$$

To compute the lattice spectral function we define

$$\alpha = \frac{\mathcal{K}^2 + \mathcal{M}^2}{4(1+\mathcal{M})} \tag{3.27}$$

to rewrite Eq.(3.15) as $E = 2\ln(\sqrt{\alpha} + \sqrt{1+\alpha})$. Now a series of three variable transformations can be performed

$$\begin{aligned} \mathbf{k} &\rightarrow \mathbf{x} = (\sin^2(k_1/2), \sin^2(k_2/2), \sin^2(k_3/2)) \, , \\ \mathbf{x} &\rightarrow (\tilde{\omega}, z_2, z_3) = (2N_\tau E_1, x_2/\alpha, x_3/\alpha) \, , \\ (\tilde{\omega}, z_2, z_3) &\rightarrow \mathbf{z} = (\sinh^2(y/4), z_2, z_3) \, , \end{aligned} \tag{3.28}$$

where for the second transformation it is necessary to invert the dispersion relation. This requires a one-to-one relation between the Energy and the momentum. This is given for the whole Brillouin zone only for $r = 1$. For the $r < 1$ case, one has to separate the zone into intervals where the one-to-one relation holds and perform the appropriate transformations for each zone separately. Here, however, the discussion is restricted to the $r = 1$ case from now on. The other case will be treated with a “binning” procedure presented in Section 3.2.4.
The transformations Eq.(3.28) lead to

$$\tilde{G}_i(\tau T) = \int_{\tilde{\omega}_{min}}^{\tilde{\omega}_{max}} \mathrm{d}\tilde{\omega} \, \tilde{\sigma}_i(\tilde{\omega}, N_\tau) \, \tilde{K}(\tilde{\omega}, \tau T) \, , \qquad i = 1, \, 2 \, . \tag{3.29}$$

with the continuum kernel $K(\tilde{\omega}, \tau T)$ defined in Eq.(2.46) and the boundaries of integration

$$\tilde{\omega}_{min} = 2N_\tau \ln\left(1 + m_q/\xi\right) \, , \qquad \tilde{\omega}_{max} = 2N_\tau \ln\left(1 + (6+m_q)/\xi\right) \, . \tag{3.30}$$

From the two functions

$$\begin{aligned} \tilde{\sigma}_1(\tilde{\omega}, N_\tau) &= \frac{N_c}{2\pi^3} \frac{N_\tau^2}{\xi^3} \tanh\left(\frac{\tilde{\omega}}{4}\right) \sinh\left(\frac{\tilde{\omega}}{4N_\tau}\right) \sinh\left(\frac{\tilde{\omega}}{2N_\tau}\right) I_1(\tilde{\omega}/N_\tau, \xi) \\ \tilde{\sigma}_2(\tilde{\omega}, N_\tau) &= \frac{N_c}{2\pi^3} \frac{N_\tau^2}{\xi^3} \tanh\left(\frac{\tilde{\omega}}{4}\right) \frac{\sinh^3\left(\frac{\tilde{\omega}}{4N_\tau}\right)}{\sinh\left(\frac{\tilde{\omega}}{2N_\tau}\right)} I_2(\tilde{\omega}/N_\tau, \xi) \, , \end{aligned} \tag{3.31}$$

the spectral functions can be reconstructed for the different channels with

$$\tilde{\sigma}_{PS}^W = \tilde{\sigma}_1 \, , \qquad \tilde{\sigma}_S^W = -\tilde{\sigma}_2 \, , \qquad \tilde{\sigma}_V^W = 3\tilde{\sigma}_1 - \tilde{\sigma}_2 \, , \qquad \tilde{\sigma}_A^W = \tilde{\sigma}_1 - 3\tilde{\sigma}_2 \, . \tag{3.32}$$

The integrals appearing in Eq.(3.31) can be expressed as

$$I_i(\tilde{\omega}/N_\tau, \xi) = \iint_{\Omega(y)} \mathrm{d}z_2 \mathrm{d}z_3 \, A(\mathbf{z}) \, B(\mathbf{z}) \, C_i(\mathbf{z}) \, , \tag{3.33}$$

with the functions A, B, C listed in Appendix B. The integration boundary is determined by

$$\Omega(y) \quad = \quad \{z_2, z_3 \mid 0 \leq xy \leq 1; \;\; 0 \leq z_2 y \leq 1 \;\;\; 0 \leq z_3 y \leq 1\} \tag{3.34}$$

with

$$x \quad = \quad \frac{\xi^2 - (z_2 + z_3)(1 - 2\xi z + m_q) + \xi m_q - \frac{m_q^2}{4z} - 2z z_2 z_3}{1 + 2z(z_2 + z_3) + m_q - 2\xi z} \; . \tag{3.35}$$

Note that cut-off effects arise from the sinh factors and the integrals I_i which both depend on $\tilde{\omega}/N_\tau$ only. No explicit dependence on $1/N_\tau$ appears as has been observed in the calculation of the cut-off effects in the equation of state[76] for example.

3.2 Free Fixed Point Action

Having obtained the meson correlation and spectral function for free Wilson fermions on the lattice, the analog but technically more complicated steps for the fixed point action are presented. As the ansatz for this action also contains the Wilson action the results obtained here implicitly contain also the results of the former section, after appropriate tuning of the corresponding parameters.

3.2.1 Construction of Fixed Point Actions

Cut-off effects arise from using finite lattice spacing a. One tries to minimize them by constructing actions which have smaller cut-off effects, i.e., have a more continuum like dispersion relation. This is achieved step by step with the Symanzik improvement program discussed in Section 2.3.2. Another approach is known as “perfect action” which is by definition free from any cut-off effects. The existence of such actions is a consequence of Wilson’s renormalization group theory[77]. For free quarks a fixed point action can be obtained with a technique called “blocking from the continuum” [43]. This leads to a representation of the lattice fermion fields ψ as the average over the continuum fermion fields Ψ on a unit hypercube, which in momentum space reads

$$\psi(k) \quad = \quad \sum_{l \in \mathbb{Z}^4} \Psi(k + 2\pi l) \prod_{\mu} \frac{2\sin(k_\mu/2)}{k_\mu} \; , \tag{3.36}$$

and leads to the propagator

$$\Delta^{FP}(k) \quad = \quad \sum_{l \in \mathbb{Z}^4} \frac{1}{i(\gamma_\mu k_\mu + 2\pi\gamma_\mu l_\mu) + m} \left(\prod_{\mu} \frac{2\sin(k_\mu/2)}{k_\mu} \right)^2 + b \tag{3.37}$$

with b as an arbitrary renormalization group parameter. This action has still a perfect dispersion relation but is nonlocal and therefore the no-go theorem remains valid. Going then back to coordinate space, one can write

$$S_F^{FP} = \sum_{x,y} \overline{\psi}(x) M_{x,y}^{FP} \psi(y) \ , \tag{3.38}$$

$$M_{x,y}^{FP} = \sum_{\mu=0}^{3} \gamma_\mu \rho_\mu(x-y) + \lambda(x-y) \ , \tag{3.39}$$

where b has been used to optimize the locality of the action, i.e., to enhance the exponential decrease of the parameters ρ and λ which can be achieved with the choice $b(m) = (e^m - m - 1)/m^2$ [43]. Restricting the available momenta to discrete values and using periodic boundary conditions, reduces the support for these coefficients to a hypercube. This defines the truncated perfect action which coefficients can be written as

$$\begin{aligned}
\rho_\mu(x-y) &= \rho_1(\delta_{y,x+\hat{\mu}} - \delta_{y,x-\hat{\mu}}) + \sum_{\hat{\nu}\neq\hat{\mu}} \rho_2(\delta_{y,x+\hat{\mu}+\hat{\nu}} - \delta_{y,x-\hat{\mu}+\hat{\nu}}) \\
&+ \sum_{\substack{\hat{\nu}\neq\hat{\mu} \\ \hat{\rho}\neq\hat{\mu},\hat{\nu}}} \rho_3(\delta_{y,x+\hat{\mu}+\hat{\nu}+\hat{\rho}} - \delta_{y,x-\hat{\mu}+\hat{\nu}+\hat{\rho}}) \\
&+ \sum_{\substack{\hat{\nu}\neq\hat{\mu} \\ \hat{\rho}\neq\hat{\nu},\hat{\sigma}\neq\hat{\rho}}} \rho_4(\delta_{y,x+\hat{\mu}+\hat{\nu}+\hat{\rho}+\hat{\sigma}} - \delta_{y,x-\hat{\mu}+\hat{\nu}+\hat{\rho}+\hat{\sigma}}) \ , \qquad (3.40) \\
\lambda(x-y) &= \lambda_0 \delta_{y,x} + \sum_{\mu} \lambda_1(\delta_{y,x+\hat{\mu}} + \delta_{y,x-\hat{\mu}}) + \sum_{\hat{\nu}\neq\hat{\mu}} \lambda_2(\delta_{y,x+\hat{\mu}+\hat{\nu}} + \delta_{y,x-\hat{\mu}+\hat{\nu}}) \\
&+ \sum_{\substack{\hat{\nu}\neq\hat{\mu} \\ \hat{\rho}\neq\hat{\mu},\hat{\nu}}} \lambda_3(\delta_{y,x+\hat{\mu}+\hat{\nu}+\hat{\rho}} + \delta_{y,x-\hat{\mu}+\hat{\nu}+\hat{\rho}}) \\
&+ \sum_{\substack{\hat{\nu}\neq\hat{\mu} \\ \hat{\rho}\neq\hat{\nu},\hat{\sigma}\neq\hat{\rho}}} \lambda_4(\delta_{y,x+\hat{\mu}+\hat{\nu}+\hat{\rho}+\hat{\sigma}} + \delta_{y,x-\hat{\mu}+\hat{\nu}+\hat{\rho}+\hat{\sigma}}) \ . \qquad (3.41)
\end{aligned}$$

The parameters ρ_i and λ_i have been computed in [73, 78] and the result is listed in Table 3.2 together with the values for the Wilson fermions and the naive fermions for comparison. The construction of the meson correlator starts again with the free fermion propagator in momentum space obtained after a Fourier transformation of Eq.(3.38)

$$S_F^{FP}(k) = \frac{-i\gamma_4 \delta \sin k_4 - i\mathcal{K}_1 - i\mathcal{K}_2 \cos k_4 + \kappa_1 + \kappa_2 \cos k_4}{(\mathcal{K}_1^2 + \kappa_1^2 + \delta^2) + 2\cos k_4(\mathcal{K}_1\mathcal{K}_2 + \kappa_1\kappa_2) + \cos^2 k_4(\mathcal{K}_2^2 + \kappa_2^2 - \delta^2)} \ , \tag{3.42}$$

$$\mathcal{K}_1 = \textstyle\sum_{i=1}^3 \gamma_i \alpha_i \ , \qquad \mathcal{K}_2 = \sum_{i=1}^3 \gamma_i \beta_i \ , \tag{3.43}$$

with the auxiliary functions $\alpha_i(\mathbf{k}), \beta(\mathbf{k}), \kappa_i(\mathbf{k})$ and $\delta(\mathbf{k})$ listed in the Appendix B. The two poles of the propagator can be written as

$$\cosh E_1 = \frac{-P - \sqrt{(P^2 - QR)}}{Q}, \tag{3.44}$$

$$\mathrm{sgn}(Q) \cosh E_2 = \frac{-P + \sqrt{(P^2 - QR)}}{Q}, \tag{3.45}$$

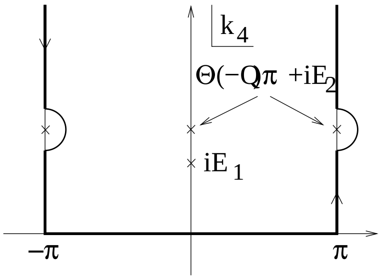

Figure 3.2: Integration contour in the complex k_4 plane.

action	FP			W	Naive
mass	0.0	1.0	2.0	m	m
ρ_1	0.136846794	0.05457967484	0.0185415007	0.5	0.5
ρ_2	0.032077284	0.01101007028	0.0031625467	0.0	0.0
ρ_3	0.011058131	0.00325481234	0.0007898101	0.0	0.0
ρ_4	0.004748991	0.00120632489	0.0002501304	0.0	0.0
λ_0	1.852720547	1.26885069540	0.8442376349	m+4r	m
λ_1	-0.060757866	-0.03008271460	-0.0119736477	-r/2	0.0
λ_2	-0.030036032	-0.01082956270	-0.0032647950	0.0	0.0
λ_3	-0.015967620	-0.00471575763	-0.0011445684	0.0	0.0
λ_4	-0.008426812	-0.00221240767	-0.0004622883	0.0	0.0

Table 3.2: The coefficients for the fixed point action are taken from [73, 78].

with the functions

$$P(\mathbf{k}) = \mathcal{K}_1\mathcal{K}_2 + \kappa_1\kappa_2, \quad Q(\mathbf{k}) = \mathcal{K}_2^2 + \kappa_2^2 - \delta^2, \quad R(\mathbf{k}) = \mathcal{K}_1^2 + \kappa_1^2 + \delta^2. \tag{3.46}$$

The resulting dispersion relation, shown in Fig. 3.3(a), along the different lattice directions $\hat{\mathbf{k}}$, is greatly improved with respect to the Wilson action (b). It stays close to the continuum one up to $|\mathbf{k}| \approx 2.5/a$ whereas the Wilson dispersion relation starts to deviate significantly already at $|\mathbf{k}| \approx 1.5/a$. This is also true for the rotational symmetry as can be seen by comparing the dispersion relations along the different axis at these points.

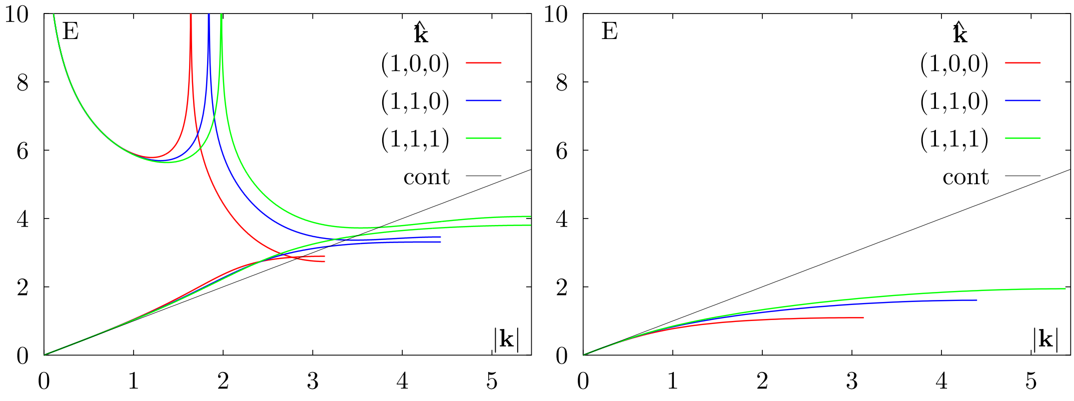

(a) (b)

Figure 3.3: Dispersion relation of the truncated FP action (a) together with the Wilson action (b). The higher energy branch of the dispersion relation for the truncated FP results from the pole E_2 and the lower energy branch from the pole E_1

3.2.2 Free FP Correlation Function

The second step is again the computation of the fermionic propagator in the $N_\tau \to \infty$ limit which can be performed analytically by an integration along the contour shown in Fig. 3.2. The two different poles appear as two different contributions, where the second contribution from $E_2(\mathbf{k})$ is a ghost branch similar to the Wilson case with $r_\tau \neq 1$ [75]

$$\begin{aligned} S_\infty^{FP}(\tau,\mathbf{k}) = \quad & \frac{1}{2\sqrt{P^2-QR}\,\sinh E_1}\; e^{-E_1\tau} \\ & [(\kappa_1 - i\mathcal{K}_1) + (\kappa_2 - i\mathcal{K}_2)\cosh E_1 + \gamma_4\,\delta\,\mathrm{sgn}(\tau)\sinh E_1] \\ - \quad & \frac{(-1)^{\tau\theta(-Q)}}{2\sqrt{P^2-QR}\,\sinh E_2}\; e^{-E_2\tau} \\ & [(\kappa_1 - i\mathcal{K}_1)\,\mathrm{sgn}(Q) + (\kappa_2 - i\mathcal{K}_2)\cosh E_2 + \gamma_4\,\delta\,\mathrm{sgn}(\tau)\sinh E_2]\ . \end{aligned} \tag{3.47}$$

The second branch is an oscillating contribution only for large momenta, where $Q(\mathbf{k}) < 0$. At small momenta the entire contribution is suppressed because $E_2 \gg E_1$. Therefore, the second branch contributes only to the short distance part of the correlation function. Returning again to finite N_τ via Eq.(3.16) leads to the mesonic correlation function for the fixed point action

$$\begin{aligned} \tilde{G}_H^{FP}(\tau T) &= N_c\left(\frac{N_\tau}{N_\sigma}\right)^3 \sum_{\mathbf{k}}\ \mathrm{Tr}\ \left[\Gamma_H S^{FP}(\tau,\mathbf{k})\gamma_5\Gamma_H^\dagger\gamma_5 S^{FP\dagger}(\tau,\mathbf{k})\right] \\ &= N_c\left(\frac{N_\tau}{N_\sigma}\right)^3 \sum_{\mathbf{k}} \frac{c_H^{FP}(\mathbf{k})\cosh[2E_1(\mathbf{k})N_\tau(\tau-1/2)] + d_H^{FP}(\mathbf{k})}{(P^2-QR)\cosh^2(E_1(\mathbf{k})N_\tau/2)} \\ &\quad + \Delta G_H^{E_2}(\tau T). \end{aligned} \tag{3.48}$$

where the functions c_H^{FP} and d_H^{FP} are given by

$$\begin{aligned} c_H^{FP} &= \frac{1}{8}\left[\sum_i T_i^H(\alpha_i + \beta_i\cosh E_1)^2 + T_u^H(\kappa_1 + \kappa_2\cosh E_1)^2 + T_4^H\delta^2\sinh^2 E_1\right] \quad (3.49) \\ d_H^{FP} &= \frac{1}{8}\left[-\sum_i T_i^H(\alpha_i + \beta_i\cosh E_1)^2 - T_u^H(\kappa_1 + \kappa_2\cosh E_1)^2 + T_4^H\delta^2\sinh^2 E_1\right]\ . \end{aligned}$$

They are listed in Table 3.1 for different channels. In contrast to the Wilson fermion case they depend on two different functions $d^{FP}(\mathbf{k})$ and $\delta(\mathbf{k})$. The first one is given by

$$d^{FP}(\mathbf{k}) = \frac{(\mathcal{K}_1 + \mathcal{K}_2\cosh E_1)^2}{\sinh^2 E_1} \tag{3.50}$$

and the second one is defined in Appendix B. Both approach one for massless quarks in the continuum limit (see Eq.(B.15)). The contribution arising from the second pole is denoted by $\Delta G_H^{E_2}$ and is also given in Appendix B.

3.2.3 Free FP Spectral Function

As pointed out in the Wilson case, the inversion of the dispersion relation is necessary for a closed computation of the spectral function. As can be seen from Fig. 3.3, this is possible for all energies only for the contributions arising from the first pole E_1. Therefore, the contribution from the second pole, denoted by $\Delta G_H^{E_2}(\tau T)$ in Eq.(3.48), is first neglected here. The change in the correlation function arising from this form leads to significant contributions only for $\tau/a \leq 1$, hence only in the extreme ultraviolet energies. It is, however, in principle also possible to divide the Brillouin zone in parts with invertible dispersion relations for the second pole, as in the case for the Wilson fermions with $r \neq 1$. But for simplicity, if contributions from the second poles are considered, the "binning" procedure, which is described in Section 3.2.4, will be used.

To compute the spectral functions arising from the first pole, the meson correlator is divided into the different contributions for c_H^{FP}, as it is done in the Wilson case

$$\begin{aligned} \tilde{G}_1(\tau T) &= N_c \left(\frac{N_\tau}{\xi}\right)^3 \int \mathrm{d}^3k \, \frac{\delta^2(\mathbf{k})}{(1+\mathcal{M})^2} \frac{\cosh[2E(\mathbf{k})N_\tau(\tau T - 1/2)]}{\cosh^2(E(\mathbf{k})N_\tau/2)} \, , \\ \tilde{G}_2(\tau T) &= N_c \left(\frac{N_\tau}{\xi}\right)^3 \int \mathrm{d}^3k \, \frac{d^{FP}(\mathbf{k})}{(1+\mathcal{M})^2} \frac{\cosh[2E(\mathbf{k})N_\tau(\tau T - 1/2)]}{\cosh^2(E(\mathbf{k})N_\tau/2)} \, . \end{aligned} \tag{3.51}$$

Again in complete analog to Eq.(3.26) a τ independent part is neglected. The series of variable transformations, necessary to deform the integration, is

$$\begin{aligned} \mathbf{k} &\rightarrow \mathbf{x} = (\cos(k_1), \cos(k_2), \cos(k_3)) \, , \\ \mathbf{x} &\rightarrow (y, x_2, x_3) = (\cosh E_1, x_2, x_3) \, , \\ (y, x_2, x_3) &\rightarrow (\omega, x_2, x_3) = (2N_\tau E_1, x_2, x_3) \, . \end{aligned} \tag{3.52}$$

This leads to the representation of G_i as

$$\tilde{G}_i(\tau T) = \int_{\tilde{\omega}_{min}}^{\tilde{\omega}_{max}} \mathrm{d}\tilde{\omega} \, \tilde{\sigma}_i(\tilde{\omega}, N_\tau) \, \tilde{K}(\tilde{\omega}, \tau T) \, , \qquad i = 1, \, 2 \tag{3.53}$$

with the continuum kernel K as defined by Eq.(2.46) and the functions

$$\sigma_i(\omega, N_\tau) = \frac{N_c}{32} \frac{N_\tau^2}{\pi^3} \tanh(\omega/4) \, \sinh(\omega/2N_\tau) \, I_i(\omega/N_\tau) \, , \tag{3.54}$$

with the integrals

$$I_1(y) = \iint_{\Omega^{FP}(y)} \mathrm{d}x_2 \mathrm{d}x_3 \, F(y, x_2, x_3) \, \delta^2(y, x_2, x_3) \, , \tag{3.55}$$

$$I_2(y) = \iint_{\Omega^{FP}(y)} \mathrm{d}x_2 \mathrm{d}x_3 \, F(y, x_2, x_3) \, d^{FP}(y, x_2, x_3) \, . \tag{3.56}$$

The definition for the various functions appearing here can be found again in Appendix B. The relations between the spectral function for a definite meson channel and σ_i are the same as in the Wilson case Eq.(3.32).

3.2.4 The binning Procedure

To transform the three dimensional momentum integral analytically into a one dimensional integral over the energy, the dispersion relation has to be a strictly increasing function of the momenta. For the case of Wilson fermions with $r \neq 1$ or the contribution from the second pole of the FP action this is no longer true for the entire Brillouin zone. Hence, one has to divide the zone into intervals in which this condition is fulfilled and perform the transformation in every interval separately. This can be avoided if one assumes the validity of the continuum kernel and transform the integral with the delta function. Then one can write the meson correlation function generically in the form

$$\tilde{G}_H(\tau T) \;=\; \int \mathrm{d}^3k \; \mathcal{F}(\mathbf{k}) \; \cosh(2E(\mathbf{k})N_\tau(\tau T - 1/2)) \;, \tag{3.57}$$

with the known dispersion relation $E(\mathbf{k})$. Then one rewrites the integral as

$$\tilde{G}_H(\tau T) \;=\; \int\limits_0^\infty \mathrm{d}\tilde{\omega} \; \tilde{\sigma}^{lat}(\tilde{\omega}) \, \frac{\cosh(\tilde{\omega}(\tau T - 1/2))}{\sinh(\tilde{\omega}/2)} \;, \tag{3.58}$$

with

$$\tilde{\sigma}^{lat}(\tilde{\omega}) \;=\; \int \mathrm{d}^3k \; \delta(\tilde{\omega} - 2E(\mathbf{k})N_t) \; [\mathcal{F}(\mathbf{k}) \; \sinh(N_\tau E(\mathbf{k}))] \;. \tag{3.59}$$

For the actual computations, one smears the delta function by partitioning the energy interval into finite elements ω_n with $\omega_{n+1} - \omega_n = \Delta\omega$ to obtain

$$\tilde{\sigma}_n \;=\; \sum_{\mathbf{k}} \Theta(2N_\tau E(\mathbf{k}) - \omega_{n-1}) \; \Theta(\omega_n - 2N_\tau E(\mathbf{k})) \; [\mathcal{F}(\mathbf{k}) \; \sinh(N_\tau E(\mathbf{k}))] \;, \tag{3.60}$$

where $\tilde{\sigma}^{lat}(\tilde{\omega}) \hat{=} \tilde{\sigma}_n$ for $\tilde{\omega} \in [\tilde{\omega}_{n-1}, \tilde{\omega}_n]$. In the limit of $\Delta\tilde{\omega} \to 0$ this equations becomes exact. The SPF presented below has been obtained using 500 bins where each bin contains about 10^5 different momenta. It has been checked, that this method indeed leads to the same SPF as the explicit expression in Eqs.(3.31) and (3.54).

3.3 Discussion of the Cut-off Effects

Having obtained the analytic results for the correlation and spectral functions for two different fermion discretization schemes, their cut-off dependence is discussed in this chapter. This is done only for the pseudoscalar channels as an example. For massless quarks the other channels are degenerate in the continuum limit[3]. Differences on finite lattices to the pseudoscalar channels will be explained in the context of the explicit chiral symmetry breaking of the fermion formulations. The values for N_τ, m_q, r etc. chosen in these discussions are relevant for actual lattice QCD calculations which are still usually performed in the quenched approximation.

---

[3] Admittedly, by the definition of Eq.(3.1) this is only true up to a factor which is divided out from now on.

3.3.1 Cut-off Effects of the Correlation Function

Cut-off effects are discussed first for correlation functions by comparing them to the continuum results. As the first step, the influence of the infrared cut-off is investigated which is introduced by a finite volume. At fixed temperature the volume is controlled by the aspect ratio N_σ/N_τ. In the correlation functions only the large distance part is sensitive to these effects. Therefore, the pseudoscalar correlation function in the chiral limit at the largest distance $\tau T = 0.5$ is listed in Table 3.3 for some lattice sizes used in Chapter 4 together with the values obtained in the thermodynamic limit, i.e., through the replacement

$$\frac{1}{N_\sigma^3}\sum_{\mathbf{k}} \quad \rightarrow \quad \frac{1}{(2\pi)^3}\int \mathrm{d}^3k \equiv \frac{1}{(2\pi)^3}\iiint_{-\pi}^{\pi} \mathrm{d}^3k \; .$$

They indicate, that for the Wilson action an aspect ratio of 4 already reproduces the $N_\sigma \rightarrow \infty$ limit for fixed N_τ within the given accuracy, whereas an aspect ratio of 2 shows large deviations from it. The same pattern is observed for the FP action, but the deviations are always smaller. Differences between the two discretizations show up in the approach to the continuum value which is 1 for this quantity. The free Wilson action approaches this continuum value as expected with N_τ^{-2}. The FP action, however, approaches this value from below. Together with finite volume effects this could sometimes lead to values even closer to the continuum result.

$N_\sigma^3 \times N_\tau$	N_σ/N_τ	W	FP
$64^3 \times 24$	$2\frac{2}{3}$	1.016	1.007
$64^3 \times 16$	4	1.018	0.998
$48^3 \times 16$	3	1.021	1.000
$32^3 \times 16$	2	1.088	1.064
$48^3 \times 12$	4	1.033	0.996
$32^3 \times 8$	4	1.076	0.992
$\infty \times 8$	4	1.076	0.992
$\infty \times 12$	-	1.033	0.996
$\infty \times 16$	-	1.018	0.998
$\infty \times 24$	-	1.008	0.999

Table 3.3: The values of $G_P(\tau T = 0.5)/T^3$ for different lattice sizes.

To investigate the influence of finite N_τ for the complete correlation function in more detail, only the infinite volume limit is considered from now on. This has the advantage

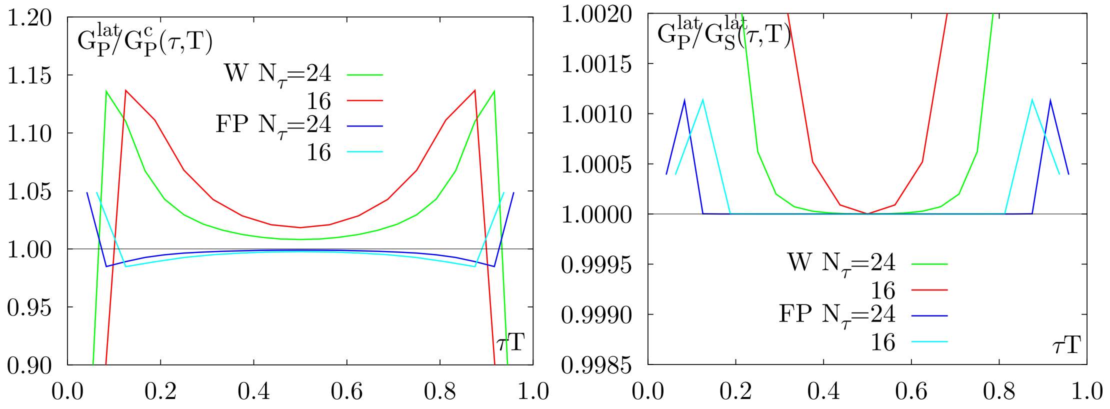

(a) (b)

Figure 3.4: Cut-off effects for the Wilson and FP fermion action.

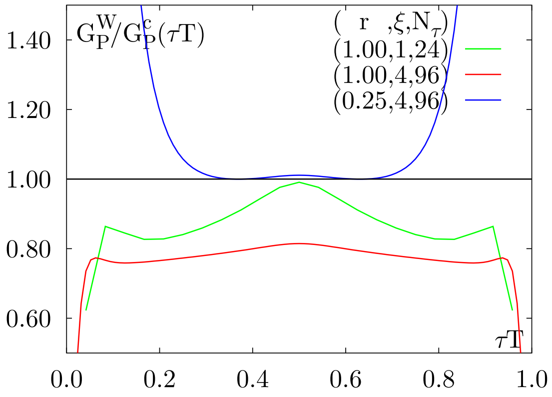

Figure 3.5: Cut-off effects for the Wilson action with $m_q/T = 4.8$.

that cut-off effects can be investigated without an admixture of finite volume effects. First, the deviation from the continuum result is investigated. As can be seen from Fig. 3.4, the ratio of the Wilson correlation function G_P^W and the continuum one G_P^c decreases only slowly with increasing distances, whereas both correlation functions differ by almost 15% at $\tau/a = 2$, independent of the N_τ values shown here. The large distance behavior is considerably improved for larger N_τ but still show deviations of about 1% at the largest distance $\tau T = 0.5$ for $N_\tau = 24$. For the FP-action deviations from unity show up only for short distances $\tau/a \leq 2$ and are smaller than 5%. At long distances, the deviations become negligible even for $N_\tau = 16$. Furthermore one can explore the influence of chiral symmetry breaking. The correlation functions, depicted in Fig. 3.4, are calculated with zero quark masses, i.e., in the chiral limit. In the continuum limit this leads to the equivalence of all mesonic channels up to an overall factor. Therefore, deviations of the ratio G_P/G_S from 1 show up only due to the explicit chiral symmetry breaking on finite lattices. For the Wilson case this ratio reaches one only at the largest distances for reasonable N_τ values and its convergence is again greatly improved if N_τ is increased. In contrast, for the FP-action the ratio stays close to one for moderately large distances $\tau/a \geq 3$, and even at small distances the deviations are only about 1‰. This shows the great improvement of the FP-action with respect to chiral symmetry.

Finally we compare isotropic and anisotropic lattices for the case of the Wilson action. It turns out that the main advantage of using anisotropic lattices in the chiral limit consists in the presence of additional points in the correlation function. This may be however different in the case of massive quarks. Here we take $m_q/T = 4.8$ as an example. For temperatures slightly above the deconfining transition, this mass corresponds to heavy quark bound states like J/ψ. As these are important observables for experimental investigations of the QGP transition[79], they are also often analyzed in lattice simulations. Hence cut-off effects in this quark mass region are also of interest. But for these heavy quark masses, a new source of discretization errors enters due to the new scale am_q. For anisotropic actions, one could have expected to reduce their influence to $\mathcal{O}(a_\tau m_q)$, which is not true in this case. Also in this case the error is rather proportional to am_q which is of the order of one for the charm quark mass and currently accessible lattice spacings. These corrections also appear in the improvement coefficients like the Sheikoleslami-Wohlert coefficient c_{sw}

which depend on am_q even at tree level of perturbation theory[80]. For this reason, it was proposed[81] to tune the spatial parameter r to reduce the quark mass effect on the improvement parameters. It was shown that one can eliminate the am_q dependence at tree level completely, if one chooses $r = 1/\xi$. This choice with $\xi = 4$ has been used in recent lattice studies [82, 54] for heavy quarks. Therefore in Fig. 3.5 the ratio of the lattice correlation functions to the free one for the isotropic and the anisotropic case with $\xi = 4$ and the choices $r = 1$ and $r = 1/\xi$ is shown. As one can see, the latter one reduces the cut-off effects at large distance but with the drawback of introducing huge cut-off effects at short distances. Hence all choices are strongly affected by cut-off effects.

3.3.2 Cut-Off effects of the SPF

The discussion of cut-off effects given above for correlation functions can be repeated in a similar way for spectral functions. As can be seen from Eq.(3.31) for the Wilson action and from Eq.(3.54) for the FP action the cut-off effects in this quantity are controlled by the energy scale $\tilde{\omega}/N_\tau = \omega a_\tau$. Consider therefore first the limit of massless quarks on isotropic lattices with $\xi = 1$ and the spatial Wilson parameter $r = 1$. The corresponding pseudoscalar spectral function is shown in Fig. 3.6 together with the continuum spectral function to highlight the cut-off effects. For the FP action two SPF are shown. The first one is labeled FP_1 and is given by Eq.(3.54) and includes only the contribution from the first pole. The second SPF FP_{12} includes the contributions from both poles, i.e., represents the full SPF. By comparing them, one sees that the second pole only contributes to high frequencies as already concluded from the correlation functions. Additional an explicit N_τ dependence for these contribution show up which results in an increase of the maxima of the FP_{12} SPF with N_τ.

The main difference between the two fermion formulations discussed here is however the

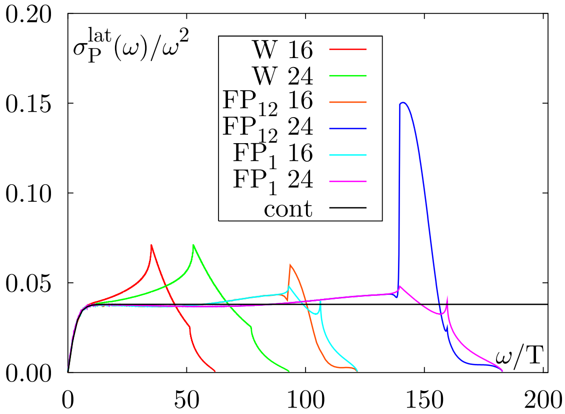

Figure 3.6: Spectral function with different cut-off. The numbers in the legend are the number of time slices whereas the letters note the action. W stand for the Wilson action and FP for the FP-action. For the latter action the contributions from the different poles, with the notation introduced in Section 3.2.2, to the SPF are discriminated.

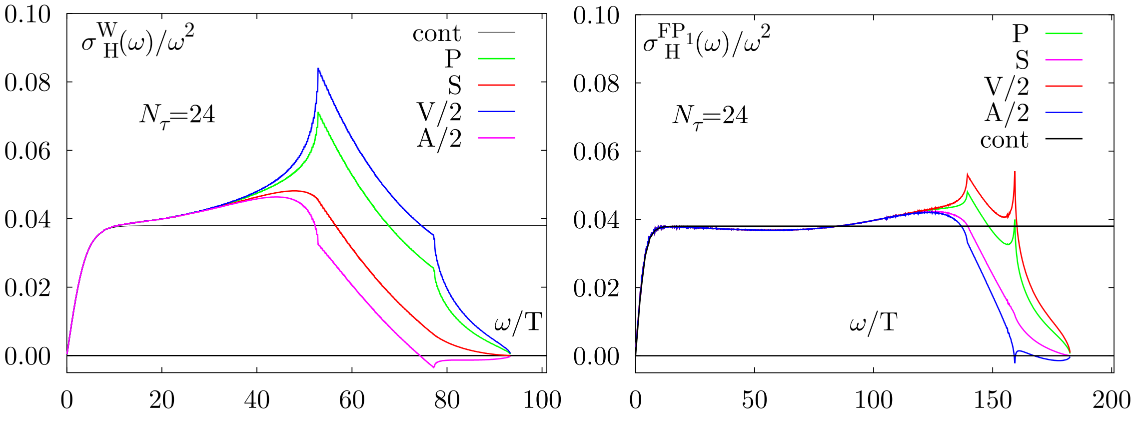

(a) (b)

Figure 3.7: Spectral function for the different meson channels calculated with the Wilson action (a) and from the first pole of the truncated FP action (b).

large shift of the ultraviolet cut-off for the FP action. The maximal available energy for the Wilson case is given by Eq.(3.30) and is limited to approximately $4N_\tau$ whereas for the FP action it is $7.5N_\tau$ which is a shift nearly by a factor two. The second difference is the deviation from the continuum within the support. For the Wilson action, deviations of more than 15% occur already at $\omega a \simeq 1.5$, whereas for the FP-action the SPF deviates less than 15% from the continuum result up to $\omega a \simeq 4.8$. The most prominent features of both spectral functions are however the characteristic peaks and cusps. They all appear at energies which correspond to the edges of the Brillouin zone. The sudden restriction of the momentum space available for the fermions leads to strong cut-off effects at the corresponding energies in the spectral function. Another cut-off effect shows up in the distortion of chiral symmetry. This is shown in Fig. 3.7 for different quantum number channels. In the low energy region the different channels fall on top off each other which indicates a remanent of chiral symmetry although it is explicitly broken for the Wilson action. As a consequence of this the axial vector spectral function is not strictly positive. In both formulations the SPF gets negative in the high energy region.

Consider now the case of anisotropic lattices, $\xi = a/a_\tau \neq 1$, in the chiral limit and for $r = 1$. Here only the Wilson action is discussed, because the parameters ρ, λ (Eqs. (3.40) and (3.41)) for the FP action have not been determined for this case. The ultraviolet cut-off for the anisotropic Wilson action is still given by Eq.(3.30). Fixing the ratio $aT = \xi/N_\tau$ and taking the limit $(N_\tau, \xi) \to \infty$ one can derive from this equation, that the maximal available energy is $\omega_{max} \to 12(N_\tau/\xi)$ which corresponds to a maximal shift to a three times larger cut-off as compared to the isotropic case. Also in this case the cut-off effects are controlled by $\omega a_\tau = \tilde{\omega}/N_\tau$ as can be seen from Eq.(3.31). In Fig. 3.8(a) the typical case $\xi = 4$ and $N_\tau = 96$ is taken as an example for an anisotropic SPF and is compared to the corresponding isotropic one. The anisotropic SPF deviates less than 15% from the continuum one until $\omega a \simeq 3.0$ (see Fig. 3.8(a)). This is a shift by a factor two, as compared to the isotropic case. Also the peak induced by the first Brillouin zone is shifted by a factor 1.4, whereas the ultraviolet cut-off is shifted again by nearly a factor 2 to higher

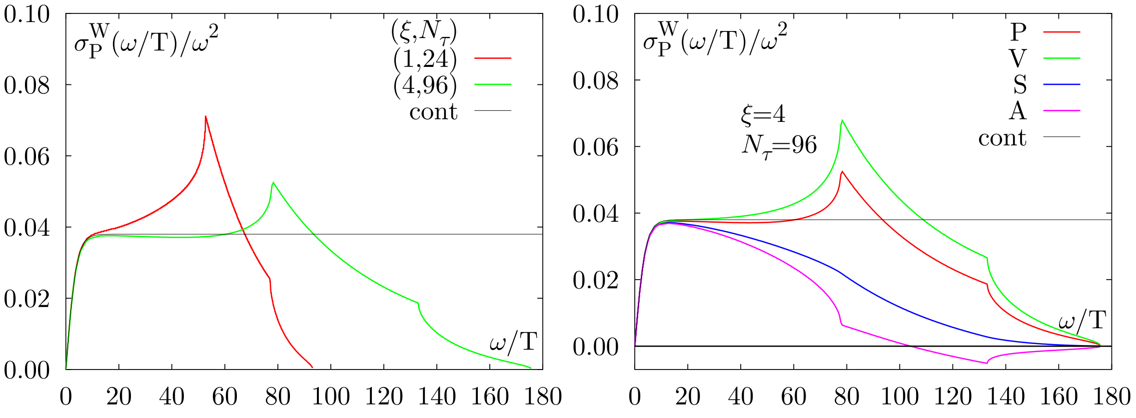

(a) (b)

Figure 3.8: (a) Pseudoscalar SPF for the isotropic and anisotropic lattice. (b) SPF for the different channels on an anisotropic lattice for $N_\tau = 96$ and $\xi = 4$.

energies. Considering, however, all channels in the anisotropic case (see Fig. 3.8(b)), the chiral symmetry breaking effects set in at even lower energies as compared to isotropic case (Fig.3.7(a)) and deviations of more than 15% from the continuum SPF in the axial vector and scalar cases appear already at $\omega a \simeq 1.4$.

The next example is given for $r = 1/\xi \neq 1$. The motivation for this particular choice has been given in Section 3.2.2 in the case of massive quarks. Nevertheless, the main observation for this choice of parameters can be made already for massless quarks. Investigating the dispersion relation, obtained with these parameters, leads to the conclusion (see Fig. 3.9(a)) that the maximum of the dispersion relation does no longer reside in the corner corresponding to momentum (π, π, π) of the Brillouin zone. This leads to a reduction of the mass splitting between the physical quark and the spatial doublers. Hence, for every set of parameters a detailed investigation of the influence of doublers is necessary. The influence of these doublers increases with increasing ξ and in the limit $\xi \to \infty$ the naive fermion formulation with degenerate doublers is recovered. The increase of time slices N_τ, obtained by increasing ξ and keeping simultaneously temperature T and volume V constant, is therefore limited. Additionally the maximal energy of a quark and therefore also for the meson is suppressed in the case of $r \neq 1$, i.e., the ultraviolet cut-off is reduced.

These effects directly translate into the cut-off effects visible in the spectral function. This is demonstrated for the pion spectral function for $N_\tau = 24$ and $r = 1/\xi = 1/4$ in Fig. 3.9(b). The vertical lines, drawn in the figure, indicate the energy of special points in the dispersion relation. The light blue line indicates the energies at the edges of the Brillouin zone. Note that the energy at the edge (π, π, π) no longer gives the ultraviolet cut-off. This is now given by the maximum appearing in the dispersion relation along the $(1, 1, 1)$ direction, shown in Fig. 3.9(a). The maxima along the other two directions are also indicated by a pink vertical line. The red lines corresponds to various energies in the dispersion relation, where in one direction of the momentum a maximum is located and in

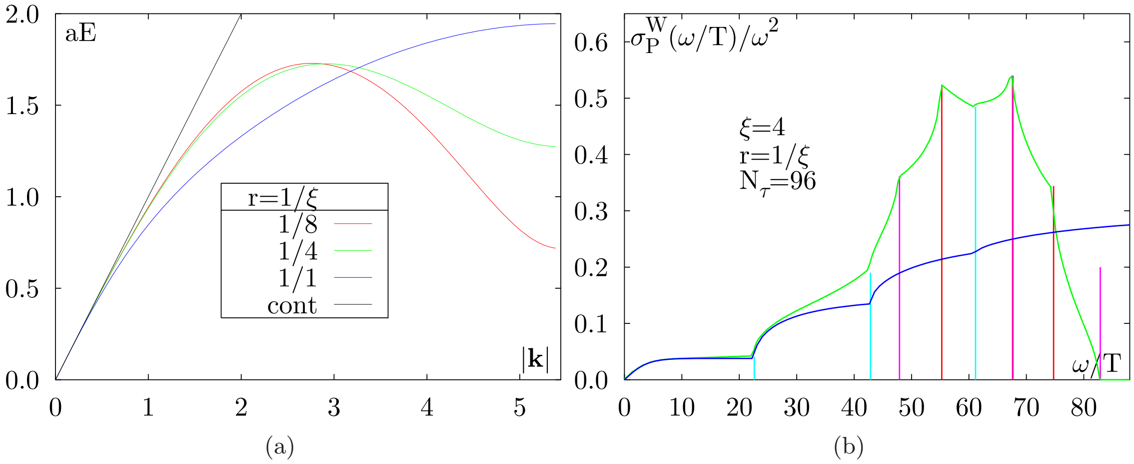

(a)

(b)

Figure 3.9: (a) Dispersion relation for different anisotropies along the $\mathbf{k} = (1, 1, 1)$ direction for the choice $r = 1/\xi$. (b) The corresponding pseudoscalar SPF for $N_\tau = 96$.

others the edge of the Brillouin zone is reached. All these lines indicate a peak or a cusp in the SPF and shows the close connection between the dispersion relation and the SPF. The blue line is obtained by adding the contribution to the SPF, obtained from the massless continuum and appropriate multiples of free continuum SPF with masses corresponding to the spatial Wilson doublers. The large deviations from the continuum which can therefore be explained by a large contribution from the spatial Wilson doublers.

Finally we discuss the case of massive quarks. As done in the discussion of the correlation function, the quark mass is fixed to $m_q/T = 4.8$. In Fig. 3.10 three different Wilson SPF with different parameter sets are shown. The $\xi = 1/r = 4$ case is improved for small frequencies which comes, however, with the price of very large deviations for $\omega a \geq 1$. These deviations can be approximately 50 times larger than the continuum value. For the two other parameter sets, significant deviations set in already at very low energies, but

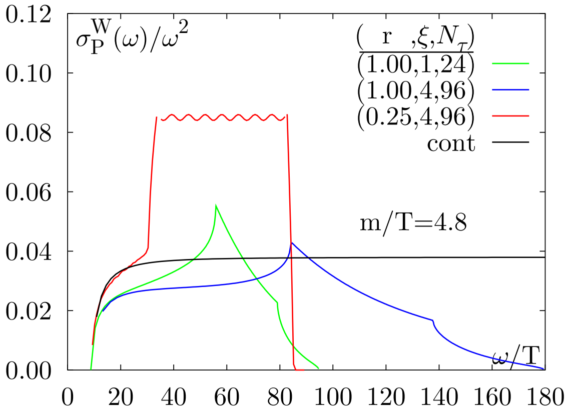

Figure 3.10: Wilson SPF for different r, ξ and N_τ with a quark mass of $m/T = 4.8$. Here the SPF with $\xi = 1/r = 4$ is cut by a wavy line for better visibility.

they stay closer to the continuum for larger energies as compared to the former one. In the end it may be advantageous to use anisotropic lattices and $r = 1/\xi$, if one is interested in the SPF in the low ω region, but one has to investigate very carefully the contributions from the spatial doublers.

3.3.3 Improved Meson Operators

To reduce the influence of excited states in the mesonic currents, see Section 2.4.2, extended meson operators have often been used. In the infinite temperature limit, considered here, gauge fixing of these operators is not necessary and an analytic calculation even for the exponential sources becomes feasible. Restricting to isotropic lattices, performing the Fourier transform of Eq.(2.65) and going to the thermodynamic limit leads to the correlation function for Wilson fermions

$$\frac{G_H^W(\tau T)}{T^3} = N_c N_\tau^3 \int \mathrm{d}^3k \;\; w_1(\mathbf{k}) w_2(\mathbf{k}) \;\mathrm{Tr}\; \left[\Gamma_H S^W(\tau,\mathbf{k}) \Gamma_H^\dagger \gamma_5 S^{W\dagger}(\tau,\mathbf{k})\gamma_5\right] \;, \tag{3.61}$$

with the Wilson quark propagator $S^W(\tau,\mathbf{k})$, Eq.(3.18), and the Fourier transformed weight functions

$$\begin{aligned} w_i(\mathbf{k}) &= \int \mathrm{d}\mathbf{x} \;\; w_i(\mathbf{x}) \; \exp(i\mathbf{k}\mathbf{x}) & (3.62) \\ &= \begin{cases} \cos(\mathbf{k}\mathbf{R}) \\ \exp(-\mathbf{k}^2/4) \\ 1 \end{cases} \quad \text{with } w_i(\mathbf{x}) = \begin{cases} \delta(\mathbf{x}-\mathbf{R}) \\ \exp(-\mathbf{x}^2) \\ \delta(\mathbf{x}) \end{cases} \quad , & (3.63) \end{aligned}$$

where the first row describes also the fuzzed sinks in a consistent notation. For the exponentially smeared operators only the case of Gaussian weight, i.e., $a = 1$ and $b = 2$ (see Eq.(2.66)) are considered as an example. The influence of these improved operators on the spectral functions is demonstrated in Fig. 3.11 again for the pseudoscalar channel. As expected already from the weight functions, Eq.(3.62), the high frequencies are suppressed. As these contain most of the lattice artefacts, the continuum spectral function is reproduced over a larger energy interval. For the fuzzing technique, however, already at $R = 1$ the spectral function gets negative for large ω/T.

Although the direct connection with continuum calculations, where only local operators are considered, gets lost[49], these operators can help to reduce the cut-off effects. Another disadvantage may be, that also physical contributions to the high energy region of the SPF may be suppressed.

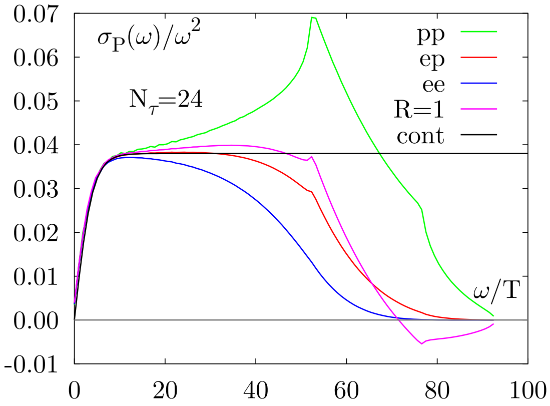

Figure 3.11: Lattice spectral function with different meson operators.

Chapter 4

Meson Properties at Finite Temperature

> *There's a long tradition in theoretical physics, which by no means affected everyone but certainly affected me, that said the strong interactions are too complicated for the human mind.*
>
> Steven Weinberg

In this chapter, the temperature dependence of meson properties is explored. This is done by using correlation functions as well as spectral functions which are reconstructed from them with the maximum entropy method. Special emphasis is put in both investigations on the influence of cut-off effects. In the beginning, the general settings of the simulations are given. Then the renormalization of the investigated currents is discussed, results for the current quark masses are presented, and a brief review of the maximum entropy method is given. Furthermore, the results for the spectral functions and the meson masses, as obtained from the correlation functions and spectral functions, are presented. Finally, the dilepton and photon rates in the deconfined phase are calculated.

4.1 Simulation Parameter

The previous chapter was devoted to the investigation of non-interacting lattice fermions. In this chapter, interactions with the gluonic heat bath are taken into account. This is done by simulating QCD in the quenched approximation. The setup for these simulations is described in this section in detail.

β	$N_\tau \times N_\sigma$	κ	N_c
6.000	$24^3 \times 16$	0.1324,0.1332,0.1342,0.1348	60
6.136	$16^3 \times 16$	0.13460,0.1354	240
6.136	$24^3 \times 16$	0.13300,0.13400,0.13460,0.13540	60
6.136	$32^3 \times 16$	0.13300,0.13400,0.13460,0.13495,0.13540	120
6.499	$16^3 \times 16$	0.13450	40
6.499	$24^3 \times 16$	0.13300,0.13400,0.13460,0.13540	120
6.499	$32^3 \times 16$	0.13300,0.13400,0.13460,0.13531,0.13540	120
6.499	$48^3 \times 16$	0.13300,0.13460	25
6.499	$48^3 \times 12$	0.13558	80
6.640	$48^3 \times 12$	0.13525,0,13536	65
6.872	$32^3 \times 8$	0.13495	65
6.872	$64^3 \times 16$	0.13495	40
7.192	$64^3 \times 24$	0.13440	80
7.192	$48^3 \times 12$	0.13440	85
7.457	$32^3 \times 8$	0.13390	70
7.457	$32^3 \times 16$	0.13390	60
7.457	$64^3 \times 16$	0.13390	80

Table 4.1: Parameters for the simulations.

To investigate cut-off effects various lattice sizes $N_\sigma^3 \times N_\tau$ and couplings $\beta = 6/g^2$ have to be explored. On anisotropic lattices a precise calibration procedure is necessary for every new coupling β. This presents a huge amount of additional work which can be avoided if one uses isotropic lattices. This is done in all our investigations. To avoid large finite size effects isotropic lattices with quite large N_τ, necessary for the maximum entropy method, and fairly large spatial lattice sizes, at least above T_c, have been used. A collection of the parameters used in our calculations are presented in Table 4.1. The runs in to the hadronic phase have been performed mostly on the APE machines in Bielefeld and the one above T_c on the Cray T3E in Jülich. For the generation of gauge field configurations the standard plaquette gauge action has been used. Subsequent configurations are separated by approximately 500 sweeps of 5 overrelaxation and one heatbath steps each. The use of the standard plaquette gauge action allows us to use the non-perturbatively determined improvement coefficient for the SW-action calculated in [40] and hence to shift the cut-off effects in the fermion action also to full $\mathcal{O}(a)$ improvement (see Section 2.3.2). To define the temperature of the lattice, the scale has to be set. Here we rely on the zero temperature calculations which have been collected and performed by Edwards et. al.[83]. They parameterized the string tension in the range $5.6 \leq \beta \leq 6.5$ by

$$(a\sqrt{\sigma})(g) \quad = \quad f(g^2)\left(1 + c_2\hat{a}(g)^2 + c_4\hat{a}(g)^4 + c_6\hat{a}(g)^6\right) / \frac{\lambda}{\sqrt{\sigma}} \tag{4.1}$$

$$\hat{a}(g) \quad \equiv \quad \frac{f(g^2)}{f(g^2(\beta = 6.0))} \tag{4.2}$$

with the constants $c_2 = 0.2731, c_4 = 0.01545, c_6 = 0.01975$ and $\lambda = 0.01364$ and the function $f(g^2)$ defined by Eq.(2.85). The validity of the parameterization up to couplings of $\beta = 7.457$ can be safely assumed. Using $T_c/\sqrt{\sigma} = 0.630(5)$, as obtained in [84], the

β	N_τ	T/T_c	a[fm]	a^{-1}GeV	κ_c
6.000	16	0.441	0.104	1.905	0.13520
6.136	16	0.553	0.083	2.389	0.13571
6.499	16	0.929	0.049	4.012	0.13558
6.499	12	1.238	0.049	4.012	0.13558
7.192	24	1.456	0.021	9.435	0.13437
6.640	12	1.487	0.041	4.817	0.13536
6.872	16	1.489	0.031	6.432	0.13495
7.192	12	2.912	0.021	9.435	0.13437
7.457	16	2.977	0.015	12.86	0.13396
6.872	8	2.978	0.031	6.432	0.13495
7.457	8	5.955	0.015	12.86	0.13396

Table 4.2: Estimated scales, temperatures and κ_c for the parameter used.

temperature T in terms of the critical one is obtained now from

$$\frac{T}{T_c} = \left(\frac{T}{\sqrt{\sigma}}\right)\left(\frac{\sqrt{\sigma}}{T_c}\right) \tag{4.3}$$

and is listed in the third column of Table 4.2 for the different couplings. Fixing the critical temperature to $T_c = 270$MeV [32], the scale a can be set and is listed again in Table 4.2. The last column contains the critical hopping parameter κ_c as obtained from interpolating the $T = 0$ results from [40], where κ_c has been determined over a large β range by investigating the vanishing of the unrenormalized current quark mass. The couplings are chosen to cover the whole temperature regime from the hadronic regime at nearly zero temperature ($0.4T_c$) to the high temperature regime ($6T_c$), accessible by refined perturbative calculations like, for instance, the Hard Thermal Loop resummation scheme. The quoted errors are, unless stated otherwise, obtained from a Jackknife analysis (see Section 2.6).

4.2 Renormalization Group Constant

As mentioned in Section 2.3.1 the currents, defined in Section 2.4, have to be multiplicatively renormalized. The calculation of the renormalization constants Z_H is presented here.

The starting point of the perturbative calculation of renormalization constants is the one loop order expression from lattice perturbation theory

$$Z_H(g^2, a\mu) = 1 - \frac{g^2}{12\pi^2}[\gamma_{H0}\ln(a\mu) + C_F\Delta_H] \tag{4.4}$$

in the chiral limit. Here γ_{H0} is the one loop coefficient of the anomalous dimension and $C_F = \frac{4}{3}$ is the Casimir coefficient of the $SU(3)$ group in the fundamental representation.

H	Δ_H	b_H	γ_{H0}
S	7.08031	0.14434	-8
P	9.38431	0.11484	-8
V	4.09381	0.11492	0
A	2.94256	0.11414	0

Table 4.3: The values $\Delta_H, b_h, \gamma_{H0}$ as given in [85, 86, 87].

β	u^4	$g^2_{\overline{\rm MS}}(1/a)$
7.457	0.91345	1.4318
7.192	0.90890	1.5417
6.872	0.90133	1.7378
6.640	0.89738	1.8476
6.499	0.89383	1.9513
6.136	0.88507	2.2294
6.000	0.87779	2.4899

Table 4.4: The calculated plaquette values and the resulting TI-couplings at $\mu = 1/a$.

Using the SW-action, Eq.(2.13), Δ_H has been calculated [87] for different quantum number channels H. The results are listed in Table 4.3. Note that in the channels A and V the renormalization factors are scale independent, as they only arise from the explicit chiral symmetry breaking of the SW action (see Section 2.3.1). Renormalization constants, calculated in bare lattice perturbation theory, often show large deviations from the non-perturbatively determined ones. Lepage and Mackenzie [85] explained these deviations by ultraviolet divergencies appearing in tadpole loops. They suggested that using "renormalized" coupling constants greatly enhances the predictive power of lattice perturbation theory. Using this tadpole improvement(TI) the renormalization constants are given as

$$Z_H(g^2, a\mu) = u^4(g^2)\left\{1 - \frac{g_P^2}{12\pi^2}[\gamma_{H0}\ln(a\mu) + C_F\Delta_H]\right\} \tag{4.5}$$

with the plaquette expectation value

$$u^4 \equiv \frac{1}{N_\sigma^3 N_\tau}\left\langle \frac{1}{3}\sum_x \text{Re Tr}\, U_{\mu\nu}(x)\right\rangle \tag{4.6}$$

which is calculated non-perturbatively on the lattice. One way to define the tadpole improved coupling[88] is given by $g_P^2 = g^2/u^4$. To obtain, however, results in the more common $\overline{\rm MS}$ scheme the coupling $g^2_{\overline{\rm MS}}$ in this scheme has to be evaluated. This computation starts with the determination of the coupling g_V which is defined by the potential $V(\mu) \equiv C_F\frac{g_V^2(\mu)}{\mu^2}$. This is related to the plaquette expectation value through

$$-\ln\langle u^4(g^2)\rangle = \frac{g_V^2(\mu^*)}{3}\left\{1 - \frac{g_V^2(\mu^*)}{4\pi}\left[\frac{66}{12\pi}\ln(6.7117/\mu^*)\right]\right\} \tag{4.7}$$

at the scale $\mu^* = 3.4018$, where the matching should be most accurate [85, 89]. Using now the non-perturbatively calculated plaquette values, listed in Table 4.4, the equation can be used to compute the coupling $g_V^2(\mu^*)$. The evaluation at the scale $\mu = 1/a$ can then be done with the standard two loop renormalization group equation given by Eq.(2.81). The conversion to the $\overline{\rm MS}$-scheme can be achieved with the relation between the scale parameters $\Lambda_{\overline{\rm MS}} = 0.6252\Lambda_V$. The results are also listed in Table 4.4. Now the renormalization factors can be calculated by using these couplings instead of g_P in Eq.(4.5). The influence of non-vanishing quark masses is given by

$$Z_H(am_q, g^2_{\overline{\rm MS}}) = Z_H(g^2_{\overline{\rm MS}}, a\mu = 1)(1 + b_H(g^2_{\overline{\rm MS}})\, am_q)\ . \tag{4.8}$$

Here the coefficients b_H can be expanded again in powers of the coupling,

$$b_H(g^2_{\overline{\rm MS}}) = 1 + C_F b_H g^2_{\overline{\rm MS}}\ , \tag{4.9}$$

and have been calculated at one loop level[86]. The results are listed in Table 4.3.

More reliable renormalization constants have to be determined non-perturbatively. In the vector and axial-vector channel the validity of the Ward identities, Eq.(2.19), can be used as a criterion to determine the renormalization constants Z_V, Z_A and b_V. Using the Schrödinger functional scheme, Lüscher et. al.[90] calculated these factors near zero quark mass at various couplings for $0 < g^2 \leq 1$ and reached an error of less than 1%. Fitting these data leads to the parameterizations

$$Z_V = \frac{1 - 0.7663g^2 + 0.0488g^4}{1 - 0.6369g^2} \tag{4.10}$$

$$Z_A = \frac{1 - 0.8496g^2 + 0.0610g^4}{1 - 0.7332g^2} \tag{4.11}$$

$$b_V = \frac{1 - 0.6518g^2 - 0.1226g^4}{1 - 0.8467g^2}. \tag{4.12}$$

In these channels, the non-perturbatively determined renormalization constants are used from now on, whereas in the other channels we rely on the values obtained from the TI perturbation theory presented above. A complete list of these perturbatively and non-perturbatively determined constants for the particular couplings and quark masses can be found in Appendix B. As can be seen there, they differ at most by 2% in those channels where both values are available. This can be used also as a guideline for error estimates in the other channels, where non-perturbative values are not available.

4.3 Quark Masses

As explained in Section 2.3.1, the quark mass can be calculated in two ways: One may make use of the vanishing pion mass in the chiral limit to compute the additive renormalization term which appears due to the explicit chiral symmetry breaking of the Wilson action. The other one utilizes the axial Ward identity. Their connection and a possible temperature dependence in this observable is discussed in this section.

The first way to compute the additive renormalization is to define the chiral limit at the quark mass value where the pion mass vanishes. Extrapolating the pion mass to this regime by utilizing the GMOR relation, Eq.(1.19),

$$m_\pi^2(m) \propto m_b \tag{4.13}$$

defines the appropriate subtraction from the quark mass $m_b(a) \equiv m - m_c$ with $m_c = 1/2\kappa_c(a)$ at given $m = 1/2\kappa$. This is obviously valid only below the chiral symmetry restoration temperature. In the high temperature regime, the quark mass has to be defined differently. Here one can make use of the axial Ward identity. From this one can determine a quark mass (see Sections 2.3.1 and 2.3.2),

$$2m_{AWI}(a) = \frac{\sum_{\mathbf{x}} \langle \nabla_4 \left(A_4(\mathbf{x},\tau) + ac_A \nabla_4 P(\mathbf{x},\tau) \right) P^\dagger(0) \rangle}{\sum_{\mathbf{x}} \langle P(\mathbf{x},\tau) P^\dagger(0) \rangle} \, , \tag{4.14}$$

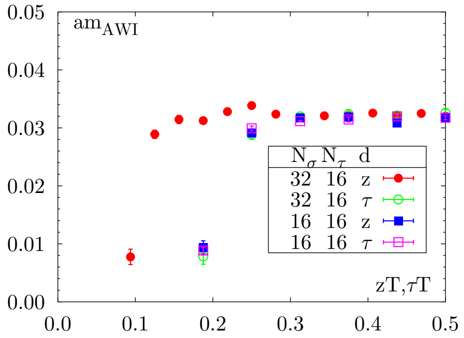

Figure 4.1: Quark mass for $\beta = 6.136$ and $\kappa = 0.1346$ for different directions and different volumes

in which the discretization effects are shifted to full order $\mathcal{O}(a^2)$[1], if the improvement constant c_A for the SW-action is chosen appropriately (see Eq.(2.40)). Here only the fourth component of the axial current is used which further enhances the overlap with the pion state. Eq.(4.14) is an operator identity and should be, apart from possible lattice artefacts, valid for all distances. That makes it possible to extract the mass from both directions, temporal and spatial, where for the spatial direction the sum over the so called funny space, which consists of the two space directions x and y and the time direction τ, is taken instead. As shown in Fig. 4.1, for $0.6T_c$ as an example, they indeed coincide in the large distance regime, independent of the volume and direction. It has also been checked that the same holds true above T_c. The plateau in the spatial direction is in any case longer than the temporal one and will be used from now on to determine the quark mass. Also note the large signal to noise ratio in the figure which is typical and allows a reliable determination of the quark mass.

In Table 4.5 the results in the hadronic phase are listed.[2] They show a significant volume dependence but this effect is only about 4%. Therefore, neglecting this effect and using only the $32^3\times 16$ lattice, where Eq.(4.14) has been evaluated for different quark masses, one can extrapolate to the chiral limit, i.e., the κ parameter where the quark mass vanishes. This leads to 0.135586(58) at $0.9T_c$ and to 0.135772(4) at $0.6T_c$ which is in good agreement with the definition of κ_c from Eq.(4.13) and the interpolated values from [40]. Hence, below T_c no temperature effect can be observed in this quantity.

Both definitions are related to the renormalized quark mass m_R with

$$\begin{aligned} m_R &= \frac{Z_A(1+b_A a m_b)}{Z_P(1+b_P a m_b)} m_{AWI} && (4.15)\\ &= Z_m(1+b_m a m_b) m_b\ . && (4.16)\end{aligned}$$

This leads to the relation

$$m_{AWI} = Z\left\{1+[b_m+(b_P-b_A)]am_b\right\} m_b \qquad (4.17)$$

---

[1] As pointed out in [91], one has to take care of the discretizing the derivative. Therefore their improved lattice derivative with errors of $\mathcal{O}(a^4)$ is used for this equation from now on.

[2] The necessary operators have not been computed for all parameters listed in Table 4.1, because of the limited programming memory of the APE machines.

β	T/T_c	$N_\sigma^3 \times N_\tau$	κ	$m_{AWI}(a)$	$m_{\overline{\mathrm{MS}}}(\bar{\mu})$[MeV]
6.136	0.55	$16^3 \times 16$	0.13460	0.0315(1)	101.7(3)
		$16^3 \times 16$	0.13540	0.0101(2)	30.7(6)
		$32^3 \times 16$	0.13300	0.0771(1)	233.2(3)
		$32^3 \times 16$	0.13400	0.0494(1)	148.5(3)
		$32^3 \times 16$	0.13460	0.0326(1)	98.4(3)
		$32^3 \times 16$	0.13495	0.0226(1)	67.4(3)
		$32^3 \times 16$	0.13540	0.0097(2)	29.4(6)
6.499	0.93	$16^3 \times 16$	0.13450	0.0337(1)	176(1)
		$32^3 \times 16$	0.13300	0.0761(2)	389(1)
		$32^3 \times 16$	0.13400	0.0476(2)	245(1)
		$32^3 \times 16$	0.13460	0.0302(2)	158(1)
		$32^3 \times 16$	0.13531	0.0094(3)	48(2)
		$32^3 \times 16$	0.13540	0.0066(3)	34(2)
		$48^3 \times 16$	0.13300	0.0758(1)	387(1)
		$48^3 \times 16$	0.13460	0.0301(2)	157(1)

Table 4.5: Quark masses as obtained from axial Ward identity below T_c in the $\overline{\mathrm{MS}}$ scheme at $\bar{\mu} \approx 2$GeV.

β	T/T_c	κ	$N_\sigma^3 \times N_\tau$	$m_{AWI}(a)$	$m_{\overline{\mathrm{MS}}}(\bar{\mu})$[MeV]
7.457	6.0	0.13390	$32^3 \times 8$	0.01045(3)	182.9(44)
7.457	3.0	0.13390	$64^3 \times 16$	0.003545(2)	62.0(4)
7.457	3.0	0.13390	$32^3 \times 16$	0.003715(17)	65.0(0)
7.192	3.0	0.13440	$48^3 \times 12$	0.00373(7)	46.8(8)
6.872	3.0	0.13495	$32^3 \times 8$	0.0095(1)	79.7(8)
7.192	1.5	0.13440	$64^3 \times 24$	0.00172(3)	21.6(3)
6.872	1.5	0.13495	$64^3 \times 16$	0.002155(7)	18.1(5)
6.640	1.5	0.13536	$48^3 \times 12$	0.003115(17)	19.4(10)
6.640	1.5	0.13525	$48^3 \times 12$	0.00635(3)	39.6(19)
6.499	1.25	0.13558	$48^3 \times 12$	0.0030(1)	15.6(5)

Table 4.6: Quark masses above T_c from the axial Ward identity.

with $Z = Z_m Z_P / Z_A$ which is valid up to order a^2. The coefficients $b_m, b_P - b_A$ and Z are calculated non-perturbatively by Guagnelli et. al.[92]. Their equivalence in the limit $g, a \to 0$ becomes obvious by using the perturbative expansion $Z = 1 + \mathcal{O}(g^2)$, $b_m = -0.5 + \mathcal{O}(g^2)$ and Eq.(4.9).

The great advantage of defining the quark mass through the current quark mass is its validity also above T_c. The results are listed in Table 4.6. Now one can utilize Eq.(4.17) to calculate the critical quark mass also above T_c from only a single current quark mass. The result is summarized in Fig. 4.2. The zero temperature points are taken from [40], where a $16^3 \times 32$ lattice has been used and the critical hopping parameter was determined from the vanishing of the axial Ward identity. The solid line is a smooth interpolation between them to guide the eye. The simulated κ values, used here, are marked with grey

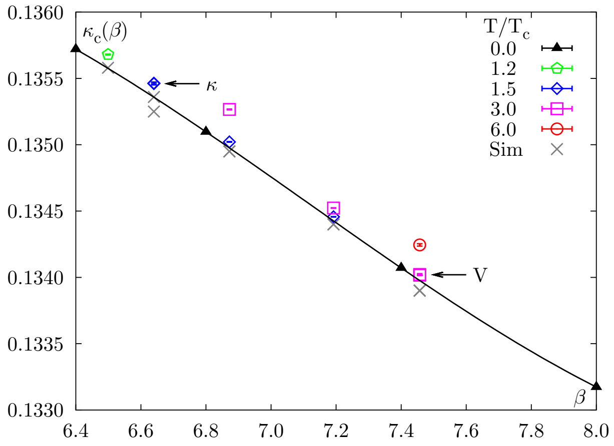

Figure 4.2: Critical hopping parameter versus β obtained from Eq.(4.17) for different temperatures and couplings.

crosses. Obvious is a shift to larger κ values for higher temperatures at constant β. This difference decreases for larger β as it should become vanish in the free theory. To exclude that this is due to possible large $\mathcal{O}(am_q)$ effects, two different κ values with the same temperature at $\beta = 6.640$ have been used to determine κ_c. As one can see, the critical hopping parameter obtained from them agree with each other. The same holds true for possible volume effects. For $\beta = 7.457$, two different volumes with otherwise equivalent parameters have been used and no significant difference could be observed. A unique interpretation of this result is, however, not possible with the present data. The first reason can be a temperature effect on κ_c. Another interpretation is a thermal quark mass, i.e., quark gets heavier with increasing temperature and the chiral limit, as determined below T_c, remains unchanged above T_c. Also a cut-off effect proportional to N_τ^{-2} is a possible explanation for the observed effect.

In the case of degenerate quark mass QCD has only two independent parameters: the coupling constant g and m_q. Both have to be renormalized and depend therefore on the scale μ and the renormalization scheme. To compare the different quark masses, obtained at the different scales $1/a$, one has to rescale them. Imposing a mass independent renormalization scheme like $\overline{\text{MS}}$, the quark mass is only a function of the scale μ and the coupling g. As for the coupling, introduced in Section 2.5, the running of the mass is described by a renormalization group equation. For the renormalized quark mass m_R it is[3]

$$\mu \frac{\partial m_R}{\partial \mu} \quad = \quad \tau(g_R)\, m_R\, . \tag{4.18}$$

The renormalization group function $\tau(g_R)$ has the perturbative expansion

$$\tau(g_R) \quad = \quad -g_R^2 \left\{ d_0 \,+\, d_1\, g_R^2 + \cdots \right\} , \tag{4.19}$$

---

[3] Note that the function τ has nothing to do with the Euclidian time τ used earlier.

where only the value of the first coefficient $d_0 = 8/(4\pi^2)$ is renormalization scheme independent. This allows to relate the running of the quark mass to the one of the coupling with

$$m_R(\mu) = M\ (2\beta_0 g_R^2(\mu))^{d_0/2\beta_0} \tag{4.20}$$

up to order g_R^4. The renormalization group invariant mass M is scale independent like the usual Λ parameter. But in contrast to Λ, whose value changes in the different renormalization schemes, the value of M can be shown to be renormalization scheme independent[93].

The usual scale for quoting the quark mass is $\mu = 2\text{GeV}$, which is approximately the lattice spacing a at $\beta = 6.0$. The other quark masses are therefore rescaled to this scale. There the coupling $g^2_{\overline{\text{MS}}}(2\text{GeV}) = 2.4288$ has been obtained. This now allows to compute the quark mass at this scale via

$$m_{\overline{\text{MS}}}(2\text{GeV}) \quad = \quad \left(\frac{g^2_{\overline{\text{MS}}}(2\text{GeV})}{g^2_{\overline{\text{MS}}}(1/a)}\right)^{d_0/2\beta_0} \frac{Z_A(g^2_{\overline{\text{MS}}}(1/a))}{Z_P(g^2_{\overline{\text{MS}}}(1/a), 1/a)} m_{AWI}(a)\ . \tag{4.21}$$

The renormalization group constants Z_H have been computed already in Section 4.2 and are listed in Appendix A.2. The resulting mass is given in the last column of Tables 4.5 and 4.6. As can bee seen, the main ordering of the quark mass is given by the temperature and not by the coupling or possible deviations from the $T = 0$ critical hopping parameter. The mismatch between values at the same temperature may be due to the mismatch of the scale, i.e., slightly different temperatures and effects of order g^4, neglected in the renormalization group equation and in the renormalization group constants. Some care has to be taken in interpretation of values given in the right column of Table 4.6 as physical or thermal quark mass. This is due to the the aforementioned interpretations of the changes in quark masses above T_c as obtained from the axial Ward identity, which includes also a dominating cut-off effect.

4.4 Maximum Entropy Method

In Section 3.2 we discussed the calculation of the spectral function from the free meson correlation function. In contrast to the free theory, a full analytic treatment of the interacting theory is not possible. In that case, only lattice simulations can be performed in which, due to the necessary Wick rotation, only static quantities like the Euclidian time meson correlation functions G_H are accessible. The direct analysis of these correlation functions will be discussed in Section 4.5.2. In this section the extraction of spectral functions with the help of the maximum entropy method (MEM) is explained.

The starting point is the relation between spectral functions and the Euclidian time correlation functions (see Section 2.4)

$$G_H(\tau,\vec{p},T) = \int \mathrm{d}^3x \, \left\langle \mathcal{J}_H(\tau,\vec{x})\mathcal{J}_H^\dagger(0,\vec{0})\right\rangle e^{i\vec{p}\vec{x}} \tag{4.22}$$

$$= \int\limits_0^\infty \mathrm{d}\omega \, \sigma_H(\omega,\vec{p},T)\, K(\tau,\omega) \tag{4.23}$$

$$K(\tau,\omega) = \frac{\cosh(\omega(\tau-\frac{1}{2T}))}{\sinh(\frac{\omega}{2T})} \tag{4.24}$$

with the integration kernel $K(\tau,\omega)$ appropriate for finite temperature. It explicitly incorporates the periodic boundary conditions needed for bosonic correlators. The inversion of this equation is an ill-posed problem, because a sensible parameterization of spectral functions consists of $\mathcal{O}(1000)$ points, whereas correlation functions are usually calculated only on $\mathcal{O}(10)$ time-slices. Moreover, correlation functions obtained in lattice calculations are not exactly known but subject to statistical errors. The problem can be handled through the use of the Maximum Entropy Method, which is a well known method in condensed matter physics and which is, for instance, also used in astronomy for image reconstruction.

For the problems described above MEM has been utilized for the first time in [94]. In the beginning it was used only to analyze data obtained from $T=0$ simulations. In this case it became feasible to extract the mass and the decay constant of the first excited state[95] which was not possible before by analyzing the correlation function only. In addition it was found that MEM also is sensitive to lattice cut-off effects. The $T=0$ spectral functions showed a broad bump at $a\omega \approx 1.7$ in the pseudoscalar channel and at $a\omega \approx 2$ in the vector channel. Because of the observed scaling with a these structures have been identified with unphysical modes arising from a bound state of a light physical and a heavy unphysical Wilson doubler. This interpretation is, however, questionable in particular in view of the results of Chapter 3.

4.4.1 Outline of the MEM Procedure

A comprehensive review of MEM as it is used in lattice calculations was given in [12] and a first explorative study at finite temperature has been performed in [51] where also details of the implementation of the MEM can be found. Therefore only a brief outline of the method is presented here.

The solution of Eq.(4.23) is not unique and therefore one can not obtain "the" spectral function but only the most probable one. The framework for this is given by Baye's theorem. It states that the posterior probability of a spectral function $\tilde{\sigma}$ describing given data G and prior knowledge expressed by the symbol H is given by

$$P[\tilde{\sigma}|GH] = \frac{1}{P[G|H]}\, P[G|\tilde{\sigma}H]\;\; P[\tilde{\sigma}|H]\,. \tag{4.25}$$

The probability to find the data set G given the prior knowledge H, i.e. $P[G|H]$, is independent of the spectral function and hence only a normalization factor. With the central limit theorem, on the other hand, one can write the likelihood function $P[G|\tilde{\sigma}H] \propto \exp(-L)$ in terms of the χ^2 distribution

$$L = \frac{1}{2}\chi^2 \equiv \frac{1}{2}\left(\sum_{i,j}(\tilde{G}(\tau_i) - G(\tau_i))C_{ij}^{-1}(\tilde{G}(\tau_j) - G(\tau_j))\right) \tag{4.26}$$

$$C_{ij} \equiv \frac{1}{N_c(N_c-1)}\sum_{n=1}^{N_c}(G(\tau_i) - G^n(\tau_i))(G(\tau_j) - G^n(\tau_j)) \tag{4.27}$$

with the covariance matrix C_{ij}, which has already been introduced in Section 2.6. $G^n(\tau_i)$ denotes the value of the correlation function on the i-th time slice calculated on the n-th configuration and $G(\tau_i)$ is its average. $\tilde{G}$ is the correlation function obtained from the trial spectral function $\tilde{\sigma}$ by

$$\tilde{G}(\tau_i) \equiv \int_0^\infty K(\tau_i,\omega)\tilde{\sigma}(\omega)d\omega \mathrel{\hat{=}} \sum_{j=0}^{j_{max}} K(\tau_i,\omega_j)\tilde{\sigma}(\omega_j)\Delta\omega \qquad \omega_j = j\cdot\omega\ . \tag{4.28}$$

Minimizing only the likelihood function corresponds to the usual χ^2 fitting procedure which is applicable only, if the number of parameters is smaller than the number of data points. The new ingredient of MEM is the additional prior probability $P[\tilde{\sigma}|H]$ in Eq.(4.25). It depends on the prior knowledge on the spectral function and is entailed in an entropy S by $P[\tilde{\sigma}|H] \propto \exp(\alpha S(\tilde{\sigma}))$. The constant α specifies the relative weight between the likelihood function, which represents the influence of the data, and the entropy, which represent the default model in the fit routine. The treatment of this α dependence is explained below. Using locality, coordinate invariance, system independence and scaling one can axiomatically construct the most general form of the entropy

$$S(\sigma) = \int_0^\infty \left[\sigma(\omega) - m(\omega) - \sigma(\omega)\log\left(\frac{\sigma(\omega)}{m(\omega)}\right)\right]d\omega \tag{4.29}$$

$$\mathrel{\hat{=}} \sum_{j=0}^{j_{max}} \left[\sigma(\omega_j) - m(\omega_j) - \sigma(\omega_j)\log\left(\frac{\sigma(\omega_j)}{m(\omega_j)}\right)\right]\Delta\omega \tag{4.30}$$

which is called “Shannon-Jaynes” entropy. Here the so called default model $m(\omega)$ has been introduced which is constructed on the basis of the prior knowledge H, e.g. the positivity of the spectral function and its asymptotic form at large ω. This form has three desirable features: It enforces the positivity of σ, requires only correlations in σ necessary to reproduce the data and allows to introduce prior knowledge about the spectra, like exact results at high frequencies[96]. One suggestion made in [12], was to use the known continuum high energy behavior of the spectral function which for the meson is $m(\omega) = \sigma_c\omega^2$ (see Section 3.1). Another choice is to use the free lattice spectral function computed in Chapter 3 which has the advantage of representing more accurately the high energy behavior of the correlation functions and fixing $\omega_{max} = \omega_{j_{max}}$, whereas this is for a free parameter the other default model [12]. For the moment ω_{max} is considered as a fixed value. The most probable spectral function is then obtained by maximizing $P[\tilde{\sigma}|GH] = P[\tilde{\sigma}|G\alpha m]$, i.e. the solution of

$$\left.\frac{\delta P[\tilde{\sigma}|G\alpha m]}{\delta\tilde{\sigma}}\right|_{\tilde{\sigma}=\sigma} \;\tilde{=}\; (\alpha\nabla_{\tilde{\sigma}}S - \nabla_{\tilde{\sigma}}L)\,|_{\tilde{\sigma}=\sigma} \;=\; 0\,. \tag{4.31}$$

This equation can be solved numerically with an ordinary Newton search.

Now the treatment of the α dependence has to be specified. This is done by a weighted average over σ and α

$$\begin{aligned} \sigma &= \int d\alpha \int [d\sigma]\ \sigma\ P[\sigma|G\alpha m]P[\alpha|Gm] && (4.32)\\ &\simeq \int d\alpha\ \sigma_\alpha P[\alpha|Gm]\,, && (4.33) \end{aligned}$$

where in the second line it is assumed that $P[\sigma|G\alpha m]$ is sharply peaked around σ_α which is satisfied for data with small errors. Using the identity

$$P[G|m\alpha] = \int [d\sigma]P[G|\sigma m\alpha]P[\sigma|m\alpha] \tag{4.34}$$

and utilizing Bayes theorem again leads to

$$\begin{aligned} P[\alpha|Gm] &= \int [d\sigma]P[G|\sigma m\alpha]P[\alpha|m]P[\sigma|m\alpha]/P[G|m] && (4.35)\\ &\propto P[\alpha|m]\int [d\sigma]\exp(\alpha S - L)\,. && (4.36) \end{aligned}$$

For the second line the same approximation as for Eq.(4.32) is made. Taking Jeffreys rule $P[\alpha|m] = 1/\alpha$ [97], the spectral function can now be reconstructed.

An error estimate has only a meaning over a certain interval $I = [\omega_i, \omega_f]$. For given α, the average and the error for this interval are given by

$$\begin{aligned} \langle\sigma_\alpha\rangle_I &\simeq \frac{\int_I \mathrm{d}\omega\ \sigma_\alpha(\omega)}{\int_I \mathrm{d}\omega} \simeq \frac{\sum\limits_{j\in I}\sigma_\alpha(\omega)\Delta\omega}{(f-i)\Delta\omega} && (4.37)\\ \langle(\delta\sigma_\alpha)^2\rangle_I &= \int [\mathrm{d}\sigma]\int_{I\times I}\mathrm{d}\omega\mathrm{d}\omega'\ \delta\sigma(\omega)\delta\sigma(\omega')P[\sigma|Gm\alpha]\bigg/\int_{I\times I}\mathrm{d}\omega\mathrm{d}\omega' && (4.38) \end{aligned}$$

with $\delta\sigma = \sigma(\omega) - \sigma_\alpha(\omega)$. The final average and error is then again given after integrating out the α dependence.

4.4.2 Test of the Maximum Entropy Method

A lot of tests have been presented in [51] and [12] to check the reliability of the above outlined procedure. They utilized the continuum default model, i.e., $m(\omega) = \sigma_c \omega^2$ and tested the influence of varying N_τ, ω_{max}, σ_c and the quality of the data. The common idea behind all these tests is to start with a given spectral function. For $T = 0$ realistic SPF consist for example of delta functions, Gaussian or Breit-Wigner peaks and a continuum contribution. Once a SPF is chosen in this limit, the corresponding correlation function can be calculated via Eq.(4.23). In the $T = \infty$ limit, the free lattice correlation function has directly been utilized [51]. With this correlation function mock data are created by adding Gaussian noise with the variance

$$v(\tau) \quad = \quad \begin{cases} b\, G(\tau)\tau & \text{if } \tau \leq N_\tau/2 \\ b\, G(\tau)(N_\tau - \tau) & \text{if } \tau > N_\tau/2 \end{cases} . \tag{4.39}$$

This form is inspired by data as obtained from simulations. The prefactor b controls the noise level which is typically chosen in the range $0.0001 - 0.1$ and represents the quality of the data. In this way, it has been shown that one can indeed reconstruct the spectral function, if the noise level is not too large and that decreasing b at fixed N_τ is more important than increasing the number of points, N_τ in the correlation function. The general observation was that increasing N_τ and the quality of the data only reduces the width and increases the height of the reconstructed spectral function if a delta function has been used as the original SPF. No dependence on ω_{max} has been observed for $T < T_c$ once it has been chosen large enough. One finds that an ω_{max} has to be chosen larger than the ultraviolet lattice cut-off which is for Wilson fermions, Eq.(3.30), $\omega_{max} \simeq 4N_\tau$. Moreover, a modified lattice kernel

$$K^{cont}(\tau,\omega) = \frac{\cosh(\omega(\tau - \frac{1}{2T}))}{\sinh(\frac{\omega}{2T})} \rightarrow K^{lat}(\tau,\omega,N_\tau) = \frac{2\omega}{N_\tau} \sum_{n=0}^{N_\tau - 1} \frac{\exp(-i\; 2n\pi\tau/N_\tau)}{4\sin^2(n\pi/N_\tau) + \omega^2} \, , \tag{4.40}$$

has to be used in order to reproduce the free continuum spectral function. It is derived by using the Matsubara frequencies for a boson on a finite lattice, i.e. $\omega_{n,lat} = 2\sin(n\pi/N_\tau)$. This kernel reproduces the continuum spectral function already with only a few points in the correlation functions, i.e. , $N_\tau \geq 8$. Tests of the influence of the value of σ_c have also been performed and it has been demonstrated that it is negligible for reasonable data sets.

A quite common approach followed to enhance the quality of the signal in the data, is to use extended meson operators, which should yield a cleaner projection onto the ground state. One possibility is the so called fuzzing technique which is suitable for a meson wave function of a definite radius R (see Eq.(2.63)). For this technique it has been demonstrated in the $T = 0$ case that the broad bump at $a\omega \approx 2$, present in all spectral functions otherwise, can indeed be completely eliminated. At finite temperature, on the other hand, the separation into ground and excited states is more difficult and in the extreme limit $T \rightarrow \infty$ only a continuum contribution exists and any correlation between two quarks has to vanish. Using the correlation function for such operators to generate mock data in this limit, it has been demonstrated [51] that MEM generates spectral functions which, for

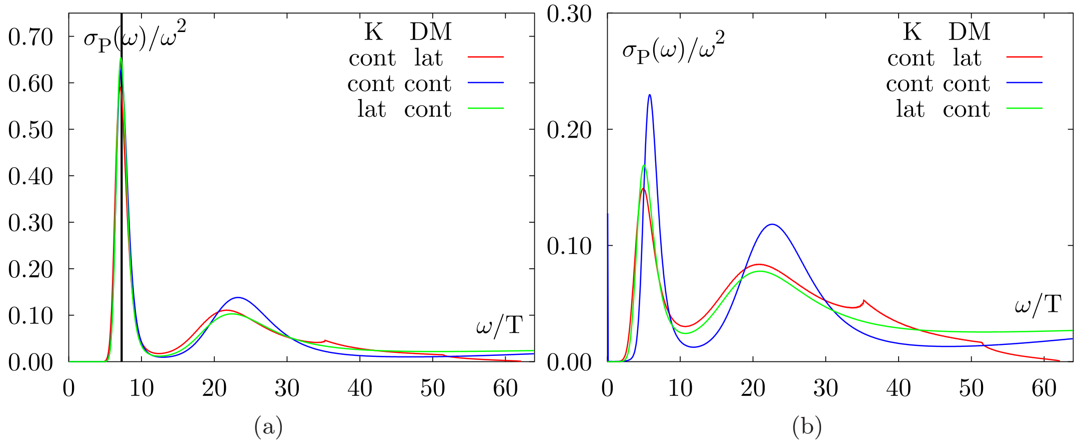

(a) (b)

Figure 4.3: Pseudoscalar spectral function obtained with different choices of the default model (DM) and the kernel (K) at $T = 0.6T_c$ (a) and at $T = 1.5Tc$ (b).

$R \neq 0$, immediately deviate from the correct result and show, already for $R = 3$, sharp and pronounced peaks which can easily be misinterpreted as bound states. The correct spectral function in this limit has been calculated in Section 3.3.3. For the fuzzed operators the result is a negative SPF at high frequencies in all channels. This simple method thus is inadequate to be used in a MEM analysis. When using exponentially smeared sources, Eq.(2.66), these problems do not occur (see Fig. 3.11). However, as the currents are no longer gauge invariant, a gauge fixing is required. Due to the additional computational overhead this approach has not been followed by us so far and therefore only point like sources have been used.

As already stated in the beginning of this section, all tests discussed so far have been made with the continuum default model. In the following we will dicuss further tests of the MEM approach using free lattice spectral functions as the default model. The different results obtained by using the different kernels (K) and default models (DM) are shown in Fig. 4.3. There the spectral functions in the pseudoscalar channel for two different temperatures, obtained with the continuum/lattice kernel and continuum/lattice default model, are shown. In Fig. 4.3(a) the effects in the hadronic region are demonstrated at $T = 0.6T_c$. All spectral functions almost coincide up to the UV cut-off. Only the choice of a continuum kernel and continuum default model shows small deviations at $\omega/T \approx 25$ where the characteristic bump for $N_\tau = 16$ is located (see discussion above). This is commonly regarded as an lattice artefact. Fig. 4.3(b) shows the spectral functions at $T = 1.5T_c$ and is chosen to represent the deconfined temperature region. Here the resulting SPF's are more sensitive to the choice of default model and integration kernel. Differences are more pronounced and start already in the low energy region which results also in a shift of the peak position. Even at lower temperatures, this deviation can sometimes be observed. This and the experience gained from the reconstruction of the infinite temperature spectral function shows the necessity to account for lattice artefacts in the MEM procedure, if one reconstructs finite temperature spectral functions. In former studies, the lattice kernel is used in order to get a more continuum like spectral function. This is, however, questionable

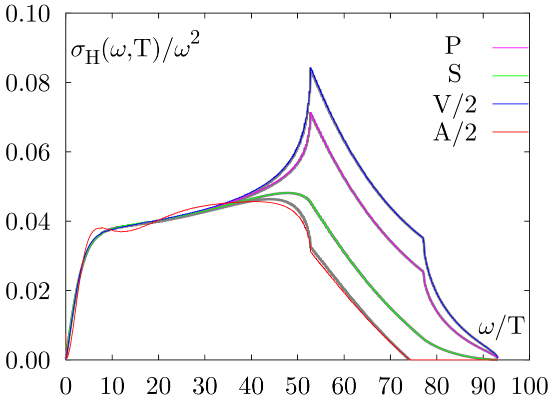

Figure 4.4: Reconstructed lattice spectral function for different quantum number channels with $N_\tau = 24$

in view of the result of Chapter 3. There it is shown that the continuum kernel is unaltered by lattice effects and the distortion due to a finite lattice spacing can be found only in the SPF. Hence, here the free lattice spectral function is taken as the default model. This choice also has the advantage to fix the high energy behavior, ω_{max} and σ_c, and only with this continuum kernel, a clean identification of lattice artefacts in the SPF is possible.

Having chosen the default model to be the lattice default model it is desirable to repeat the test, whether MEM is able to reproduce correctly the spectral function in the $T \to \infty$ limit from the free lattice correlation functions. This is demonstrated in Fig. 4.4. The original default model in all quantum number channels is drawn as a black line and is almost undistinguishable from the reconstructed spectral function which verifies that the default model is indeed the correct lattice spectral function. As also can be seen, this is not the case for the axial-vector channel. But this is due to the fact that this spectral function is not positive definite. In the default model this has been circumvented by replacing the negative contribution by a tiny positive constant. The obvious difference between the reconstructed spectral function and the default model reminds us that one has to be careful when trying to reconstruct spectral functions which are not strictly positive. Alternatively one could use an entropy function as proposed in [98] which does not rely on this positivity restriction.

Finally we discuss the influence of the statistic on the reconstruction of SPF's. If the statistic is good, the correlations between the different time slices should be taken into account. This is done by using the full covariance matrix in Eq.(4.26). In realistic cases however the statistic is sometimes rather limited. This induces spurious tiny eigenvalues in the covariance matrix. To handle such datasets and still take some of the correlations into account, one should isolate these eigenvalues by the singular value decomposition and replace them by the average over the smallest eigenvalues (for details see Section 2.6). The number of eigenvalues which are not considered to be small determine the level of these smoothing procedure. Thus taking the full covariance matrix corresponds to the maximal smoothing level (SL) $SL = N_\tau/2 \hat{=} f$ which may have to be reduced appropriately. The consequences of taking too many or to few eigenvalues into account is demonstrated for

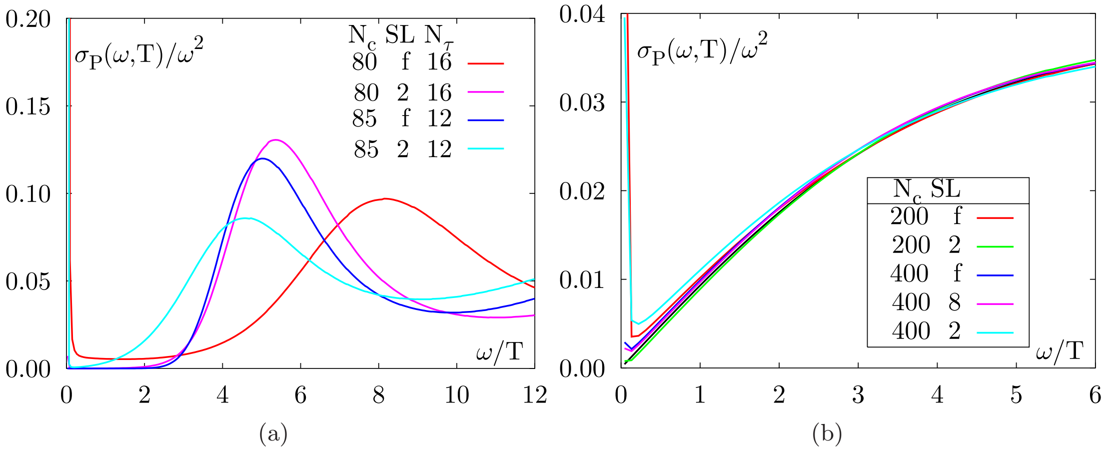

Figure 4.5: Dependence of the spectral function on the covariance matrix for the $T = 3.0T_c$ (a) and the free case (b).

the pseudoscalar channel at $T \approx 3.0T_c$(left) and in the $T \to \infty$ limit (right) in Fig. 4.5. For the latter datasets with 200 and 400 configurations, 24 time slices and a variance with $b = 0.01$, have been created. Then spectral functions have been reconstructed with different smoothing levels. With 200 configurations a perfect reconstruction is possible with a smoothing level $SL = 2$ whereas taking the full covariance matrix leads to a large entry in the first bin of the spectral function although no δ like contribution at $\omega = 0$ is present in this channel. Using two times more configurations, the situation has changed. Now for the smoothing level 2 large entries not only in the lowest bin suddenly occur. If the reconstruction is performed with more maintained eigenvalues this behavior disappears and the expected spectral function is obtained again. In the interacting case the same pattern can be observed. In general it is, however, difficult to formulate a unique criterion which allows to select the "correct" smoothing level for a given data set. The SPFs generally show additionally a large broadening of the peak and a shift is accompanying the infrared behavior of the SPF. Also a dependence on the number of time slices can be observed which can not be interpreted as a finite volume effect, because for both cases, $N_\tau = 16$ and $N_\tau = 12$, an aspect ratio of 4 has been used which results in the same physical volume. With the "correct" smoothing level, 2 for the $N_\tau = 16$ and the full covariance matrix for the $N_\tau = 12$ case, the cut-off dependence is small.

In general the statistics should, of course, be increased until the full covariance matrix of the spectral functions could be maintained in the MEM. However, since our statistic is limited we decided to start our data analysis with the lowest smoothing level and increase it as long as the spectral function is insensitive under small changes of the smoothing level.

4.5 Temperature Dependence of Meson Properties

The temperature dependence of meson properties have been studied for a long time. At zero temperature results for meson masses have been extrapolated to the continuum limit and deviations of the masses calculated on the lattice from the experimentally measured one, are expected to arise from the quenched approximation [34]. Simulations at finite temperature, however, are still contaminated by lattice artefacts. Due to the limited N_τ value which can be afforded in the simulation at fixed T, also the range of values for lattice spacing a which introduces the artefacts in these calculations, is limited.

4.5.1 Screening Masses

Due to the finite extent of the lattice in the time direction spatial rather than temporal correlation functions are often analyzed. This allows to reach the large distance regime where a clean separation of the ground state becomes possible. As discussed in Section 2.4.3, the screening masses m^z_H, obtained from these correlation functions generally differ from pole masses and may give informations on modifications of dispersion relations. In a simple model the screening mass can be related to the pole masses m_H by $m^z_H(T) = m_H(T)/A(T)$ with $A(T) \simeq 1$ at low temperatures (see Section 2.4.3). Special emphasis is put in the following on the influence of lattice artefacts, which extents the investigation in [99].

Screening Masses below T_c

The screening masses considered here, are extracted from a fit including one and two poles, Eq.(2.58), in order to absorb possible contaminations from excited states (see discussion in Section 2.4.2). At larger distances the fit results from the two pole ansatz agree with the one obtained from the one pole ansatz. If the fitted masses of both ansätze is plotted over the fit range a common plateau is formed. The screening masses listed in Tables A.3 and A.4 are then obtained from a weighted average over this plateau. At $T < T_c$, zero modes in the fermion matrix $\mathcal{M}$ prohibit calculations directly at zero quark mass. Therefore, the masses have to be extrapolated to the chiral limit. This is done by assuming for the quark mass dependence of the meson masses, the validity of lowest order chiral perturbation theory

$$\begin{aligned} {m^z_P}^2(\kappa) &= s_P \left(\frac{1}{\kappa} - \frac{1}{\kappa_c} \right) && (4.41) \\ m^z_H(\kappa) &= m^z_H + s_H \left(\frac{1}{\kappa} - \frac{1}{\kappa_c} \right), \qquad \text{H=S,V} \; . && (4.42) \end{aligned}$$

The first equation is used to obtain the proper quark mass subtraction κ_c which is listed for the different temperatures in Table 4.7. Once κ_c is fixed the pseudoscalar(P) mass, the vector(V) and scalar(S) screening mass can be obtained from the second equation. Corrections to these equations are twofold: In the heavy quark mass regime, where the binding energy between the two quarks might be neglected in a first approximation, the screening masses in all channels should roughly be equal to twice the quark mass. In the limit of vanishing quark masses quenched chiral perturbation theory predicts the occurrence of so called "quenched chiral logs". As shown in Fig. 4.6 for the vector channel as an example, none of these corrections have to be taken into account in the investigated mass interval, because the ratio ${m_V^z} T_c/{m_P^z}^2$ follows a straight line as predicted by Eq.(4.41). The blue line in the figure indicates a linear fit to the $T = 0.4T_c$ data which indeed ends in the physical $T = 0$ mass ratio and is shown to guide the eye. Performing the extrapolations to the chiral limit, one obtains the screening masses listed in Table 4.7, where the results for $N_\sigma = 24$ and $N_\sigma = 32$ are given. The former have already been published in [51]. The critical hopping parameter values obtained in this way show only small finite size effects of about 3‰ and are in good agreement with the current quark mass estimates (see Section 4.13), although the definitions allow for differences of order $\mathcal{O}(a)$. Hence, only small cut-off effects could be observed in this observable. For the lowest temperature of $0.4T_c$, corresponding to $\beta = 6.00$, the $T = 0$ meson mass of 770MeV could be reproduced within the error. For the other temperatures $T = 0.6T_c$ and $T = 0.9T_c$, corresponding to $\beta = 6.136$ or 6.499 respectively, two different lattice sizes have been utilized and indeed systematic finite size effects, i.e., larger vector meson masses in smaller volumes (see discussion is Section 2.4.2), can be observed. The same effect is observed between the $N_\sigma = 32$ and the $N_\sigma = 48$ masses at fixed κ. Restricting to one lattice size, one can observe a systematic increase of the vector meson mass with temperature, as can already be infered from Fig. 4.6. By fixing the lattice size, however, the volume becomes smaller, when the temperature is increased, which could partly explain why the vector mass increases with temperature. However, it seems that a temperature effects remains, indicated by comparing the $0.4T_c$ mass, obtained on a $N_\sigma = 24$ lattice, with the $0.6T_c$ mass, obtained on the $N_\sigma = 32$ lattice, which have approximately the same volume. Another source of uncertainty does arise from to the determination of a which is also of order 5%. Considering the scalar masses at all temperatures such systematic finite volume effects could not be observed but may be hidden in the fairly large statistical errors.

Screening Masses above T_c

In the high temperature limit the screening masses approach the value $2\pi T$. This is due to the antiperiodic boundary conditions in the time direction. The smallest "energy" for the single quark is therefore the lowest fermionic Matsubara frequency πT which leads to $2\pi T$ for the meson correlator. Hence, the screening masses above T_c have to be compared with this value to discuss medium effects. This value however gets modified on finite lattices. This has to be taken into account, in order to get the correct $T \to \infty$ limit. This is done

T/T_c	N_σ	κ_c	$m_V^z a$	m_V^z[GeV]	$m_S^z a$	m_S^z[GeV]	L[fm]
0.9	32	0.13559(6)	0.226(7)	0.907(3)	0.355(29)	1.424(116)	1.57
	24	0.13592(11)	0.246(12)	0.987(48)	0.255(31)	1.023(124)	1.18
0.6	32	0.13571(9)	0.345(7)	0.824(17)	0.670(47)	1.601(112)	2.656
	24	0.13613(6)	0.369(16)	0.882(38)	0.442(78)	1.056(186)	1.992
0.4	24	0.13551(5)	0.398(18)	0.758(34)	0.387(226)	0.737(430)	2.496

Table 4.7: Screening masses and κ_c as obtained from $N_\tau = 16$ lattices with the different volumes and temperatures below T_c.

by taking the effective masses of the free theory at the distance $z = N_\sigma/4$, to obtain the lowest frequency on the lattice. The screening masses, corrected with this value, are listed in Table 4.8. As can be seen, they differ at fixed temperature for different volumes. The opposite order of this finite volume effect, in contrast to the $T < T_c$ one, is solely due to the aforementioned correction procedure as can be infered from the uncorrected masses in lattice units listed in Table A.4. As supported by the analysis of the free correlation functions in time direction an aspect ratio of $N_\sigma/N_\tau \approx 4$ yields only minor finite size effects, and these are expected to be even smaller in an interacting theory. As for the largest available lattice the aspect ratio is $N_\sigma/N_\tau \geq 4$ at all temperatures, one can assume that finite size effects are not severe in these cases. Another possible source of errors arises from finite quark masses as discussed in Section 4.3. To exclude such effects, at $1.5T_c$, a twice as large quark mass has been analyzed for which results agree with the smaller quark mass within errors. The influence of finite quark masses on screening masses has also been discussed in more detail in [99] with the same result. A finding in [100] was, that finite a effects are the dominant source of errors in the behavior of the screening masses. By comparing the different cut-offs at different temperatures, for example at $3T_c$, where three different lattice spacings are available, these findings could not be confirmed.

Having identified and estimated the lattice artefacts, medium effects can now be discussed. Regarding the temperature dependence of the screening masses, one can observe that in the vector and axial-vector channel the masses are much closer to the free $q\bar{q}$-behavior than in other channels. Their masses agree with each other above $1.2T_c$. This effect is even more pronounced, if one compares the scalar and pseudoscalar channels for which masses also agree with each other within the errors at $1.5T_c$. This can be interpreted as an effective $U_A(1)$ symmetry restoration. All screening masses deviate from the free case, which hints at strong medium effects even at $6T_c$. However, a continuous approach to $2\pi T$ can be observed.

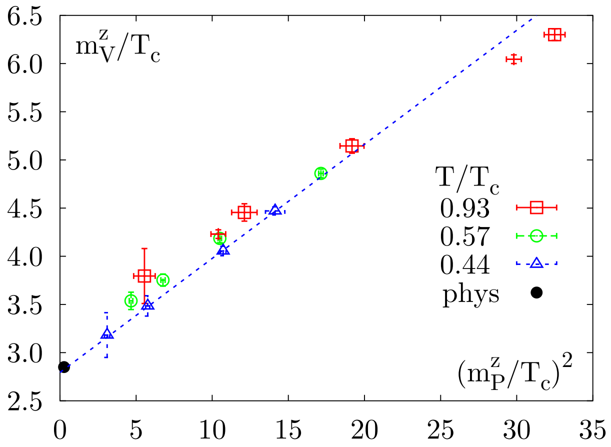

Figure 4.6: Ratio of the screening masses as obtained from the $N_\sigma = 32$ lattice.

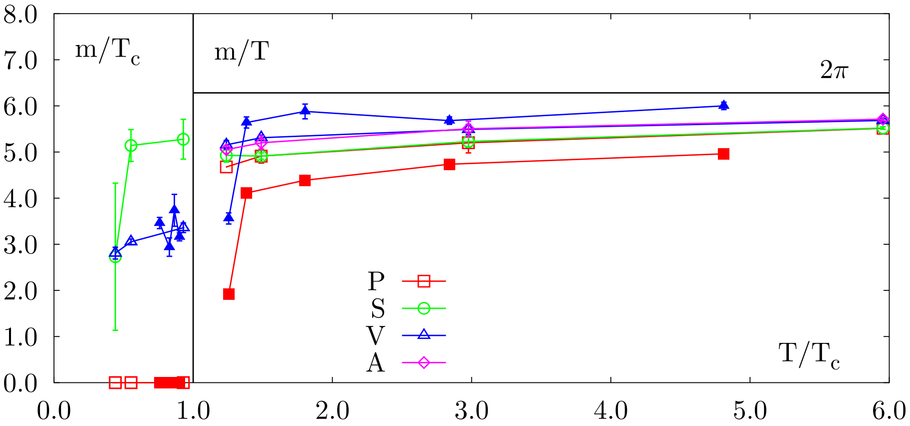

Figure 4.7: Temperature dependence of the screening masses above and below T_c as obtained from the Wilson(open symbols) and staggered fermion action(filled symbols).

Summary of Results on Screening Masses

The complete findings are summarized in Fig. 4.7. In the left part of the figure the meson masses are given in units of T_c, whereas above T_c the masses are plotted in units of the temperature. In both cases only the values for the largest lattices are plotted. Additionally, the screening masses obtained with the staggered fermion discretization are included[101]. They have been obtained at similar volumes but with $2-4$ times larger lattice spacing. Below T_c, they have also been extrapolated to the chiral limit, whereas above T_c the simulations have been performed at a bare quark mass of $m_q a = 0.02$. As one can observe below T_c, the results from the staggered and Wilson formulation differ only little, whereas above T_c strong deviations can be observed. To be more quantitative, for the staggered fermions the ratio of pion to vector masses is 0.75(2) at $1.8T_c$ whereas for the Wilson formulation a ratio of 0.93(3) can be observed already at $1.5T_c$. This value is in agreement with other investigations with Wilson fermions, where extended meson operators have been used [52, 99]. In [52] even a 3.5 times larger volume has been obtained by the use of anisotropic lattices which supports the result that finite volume effects could not explain

T/T_c	N_τ	N_σ	m_P/T	m_S/T	m_V/T	m_A/T	L[fm]
6.0	32	8	5.51(4)	5.52(3)	5.68(4)	5.71(4)	0.48
3.0	64	16	5.24(8)	5.24(7)	5.49(11)	5.49(12)	0.96
	48	12	5.37(3)	5.39(2)	5.59(3)	5.57(5)	1.01
	32	16	4.71(4)	4.71(4)	5.12(4)	5.04(6)	0.48
	32	8	5.34(4)	5.36(5)	5.57(6)	5.54(8)	0.99
1.5	64	24	4.64(8)	4.62(8)	5.06(8)	5.10(7)	1.34
	64	16	4.93(7)	4.91(7)	5.31(14)	5.20(15)	1.98
	48	12	5.04(6)	5.04(6)	5.30(6)	5.31(10)	1.97
1.24	48	12	4.68(10)	4.93(15)	5.16(9)	5.05(8)	2.35

Table 4.8: Screening masses above T_c for different lattice sizes.

the difference. The fact that these investigations have been performed with standard Wilson [52] or tree level improved SW-action [99], in contrast to the non-perturbative improved SW-action used here, also excludes large a effects which is in agreement with our findings. Hence, the screening masses, obtained with the Wilson fermion action, do not seem to be influenced strongly by lattice artefacts. Why the staggered screening masses show a strong deviation from these results remains still an open question, in particular as similar volumes have been used. A remaining possibility is a large $\mathcal{O}(a^2)$ effect in the staggered discretization which has to affect the pion and the vector channel differently in magnitude and in the opposite way and thus makes this explanation unlikely [99]. However, a more detailed investigation clearly is needed.

4.5.2 Modifications obtained from Temporal Correlation Functions

The analysis of the pole masses can, in principle, be performed in the same way at it has been done in the case of screening masses. But due to the limited temporal extent at finite temperatures, the correlation functions are contaminated by large contributions from excited states or, at even higher temperatures, from continuum contributions. This makes an extraction of the ground state mass rather difficult. Anyhow, some attempts have already been presented in [51] and in [52], where usual two state fits, similar to the method described in Section 4.5.1, have been performed. Here the problem is addressed with other methods.

Correlation Functions below T_c

The first method uses the behavior of the midpoint of the correlation function. This method is motivated by the observation that the smallest disturbances in the correlation function, from the excited states and the continuum, are expected at the midpoint $G_H(\tau = 1/2T)$. This makes this quantity particularly suited for the extraction of information on the ground state mass. The starting point for the relation between this quantity and the ground state mass is its spectral representation

$$G_H(\tau = 1/2T) \quad = \quad \int_0^\infty \mathrm{d}\omega \, \frac{\sigma(\omega, T)}{\sinh(\omega/2T)} \; . \tag{4.43}$$

Additionally, a one pole ansatz for the spectral function $\sigma(\omega) = |\langle 0|O_H|H\rangle|^2 \delta(\omega^2 - m_H^2)$ is utilized here. This ansatz is justified again by the fact that this point in the correlation function should have the smallest contaminations from excited states. Additional continuum contributions can be neglected, if the onset, σ_c, is large enough (see Section 2.4.2). In any case, this procedure has the additional advantage, as opposed to the commonly used susceptibilities, Eq. (2.60), that $G_H(\tau = 1/2T)$ is an ultraviolet safe quantity due to

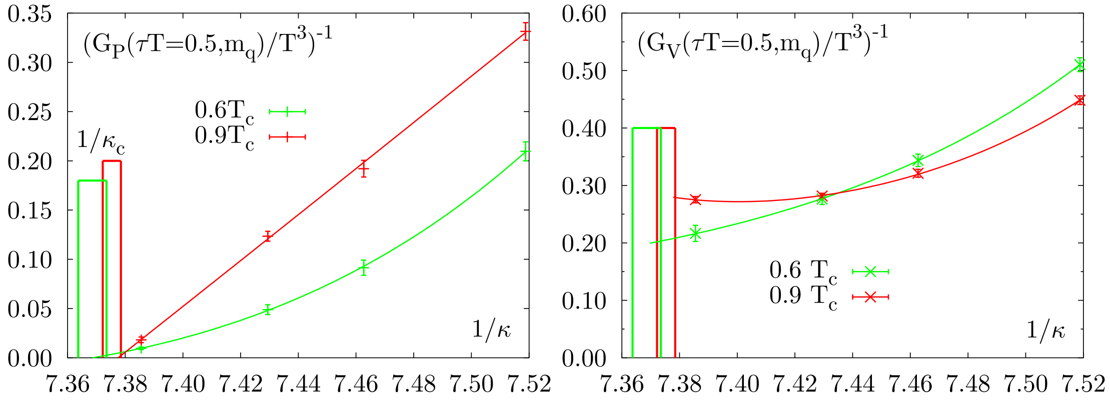

(a) (b)

Figure 4.8: Quark mass dependence of the midpoint of the correlation function together with the fits with Eq.(4.44).

the exponential suppression appearing from the denominator. Using this ansatz, together with the mass dependency of the matrix element, as explained in Section 2.4, one obtains

$$\left(\frac{G_P(\tau T=0.5,\kappa)}{T^3}\right)^{-1} \propto \frac{m_P(\kappa)}{T}\sinh\left(\frac{m_P(\kappa)}{2T}\right) \overset{\kappa\to\kappa_c}{\longrightarrow} \frac{m_q}{T}, \tag{4.44}$$

$$\left(\frac{G_H(\tau T=0.5,\kappa)}{T^3}\right)^{-1} \propto \frac{\sinh(m_H(\kappa)/2T)}{(m_H(\kappa)/T)^3}\,, \quad H=S,V,A\,. \tag{4.45}$$

As discussed in Section 3.2.2, the drawback of this quantity is its sensitivity to finite volume effects. The extrapolation to the thermodynamic limit has therefore to be done and is successfully performed with the simple ansatz $G_H(\tau = 1/2T, V) = a + b/V$. After this extrapolation, the quark mass dependence of the meson masses $m_H(\kappa)$ is parameterized as usual, with the chiral perturbation theory formulas, Eq.(4.41). The result for the pion and the vector meson is depicted in Fig. 4.8, where the boxes indicate the critical quark masses, as obtained from the vanishing of the pseudoscalar screening mass. The figure shows that κ_c, obtained from the temporal pion correlator, is compatible with the one obtained from the screening masses and has the values of $\kappa(0.6T_c) = 0.13571(3)$ and $\kappa(0.9T_c) = 0.13555(3)$. The quoted errors result from the fits because a jackknife analysis which includes correlations between the different quark masses has not been performed. The vector masses, defined by the fit parameter which represents the meson mass at the chiral limit, are $m_V = 1.39(62)$GeV at $0.6T_c$ and $m_V = 1.30(6)$GeV at $0.9T_c$, where again the errors are sole fit errors. These results are subject to large errors but show in the vector channel, at least at $0.9T_c$, significant deviations from the screening masses which is another indication of temperature effects in this channel. A temperature dependence of the ground state mass, however, can not be verified from this analysis alone, as such effects can also be explained by a modified dispersion relation.. Nevertheless, the assumption that the pion remains a Goldstone boson even up to $0.9T_c$, is supported by this analysis.

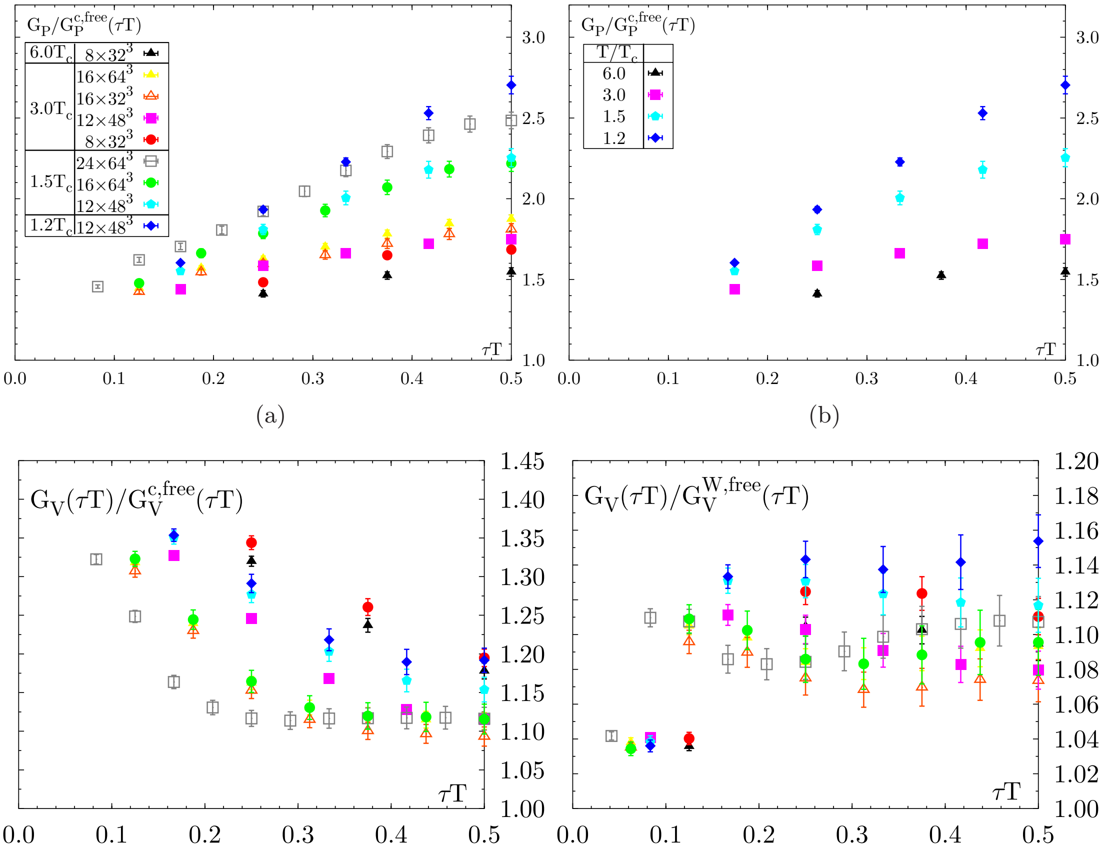

(a) (b)

(c) (d)

Figure 4.9: Ratio of the correlation function over the free one, Eq.(3.7), for the pseudoscalar channel (a) and the vector channel (c) for various temperatures and lattice sizes.(b) The ratio of the pseudoscalar correlation functions for the $48^3 \times 12$ lattice for various temperatures. (d) The vector correlation function normalized to the free lattice correlation function, Eq.(3.19). The legend is the same in all figures.

Correlation Functions above T_c

Another way to investigate thermal modifications of meson properties, is to consider the correlation functions themselves. To get information about the interaction in a given channel, they can be compared with the free correlation functions. Deviations of this ratio from one signals the influence of interactions. More details of the properties of this ratio can be found in the review [49]. The investigation, presented here, largely extends the one presented in [51] in the discussion of lattice artefacts. Here, this ratio is investigated only above T_c, to avoid complications arising from a non-vanishing quark mass.

First, the temperatures dependence in the pseudoscalar channel is discussed. The correlation functions in this channel, obtained from the $48^3 \times 12$ lattice at the temperatures between $1.2 \leq T/T_c \leq 3$ and from the $32^3 \times 8$ at $6T_c$, normalized to the continuum free correlation function, are shown in Fig. 4.9(b). The first observation is a reduction of this ratio with increasing temperature as it is expected. However, even at $6T_c$ the ratio strongly deviates from unity which leads to the conclusion that interactions still play a significant role in this channel even at this high temperatures. A more detailed analysis, at $T = 3.0T_c$, allows to investigate the finite volume effects by comparing the two different correlation functions for $N_\tau = 16$ and $N_\sigma = 32$ and 64, respectively. They differ from each other only in the volume which leads to a statistically significant but small difference at large distances. From this, one can infer that the infrared contributions are only slightly enhanced in larger volumes. Furthermore, investigating the three different correlation functions with an aspect ratio $N_\sigma/N_\tau = 4$, also at $T = 3T_c$, a finite a effect can be observed which leads to an increase of the correlation function at decreasing a. One has, however, to be careful not to interpret this effect as a discretization effect alone, because a change in a also leads to a change in temperature. To be sure that calculations at different N_τ and a really have the same temperature, a precise knowledge of the β-function, Eq.(2.84), is needed. As this is at present not the case a possible mismatch between β and a remains and might explain the observed differences in simulations with different N_τ at similarly chosen temperatures. This mismatch also renders the correlation functions at $1.5T_c$, and the two simulations with the same aspect ratio agree with each other, so that this effect has to be small. Its influence, however, may be stronger at smaller volumes which could to some extent explain the large deviation of the $N_\tau = 24$ correlation function to the aforementioned other two. In addition, β-depending effect comes from the value of the renormalization group factors constants Z_H. As they enter multiplicatively, they have direct influence on these ratios and could also explain some of the discrepancies between the different correlation functions at $1.5T_c$.

The situation is different in the vector channel, shown in Fig. 4.9(c), where these factors are known non-perturbatively and uncertainties in them should be small. But as the deviations at $\tau T = 0.5$ from one are only between 10% and 20%, cut-off effects, which in the free case are about 9% (see Table 3.3.1), become more important. Investigating the large distance behavior of these ratios, the largest deviations from one show up on lattices with $N_\tau = 8$, independently of the temperature. As it is demonstrated with Fig. 4.9(d), the discrepancies between all the different channels can be absorbed by a normalization with the free lattice correlation function. The deviations between the different lattice sizes can therefore be explained by cut-off effects and the ratios scale with the temperature. This is additional evidence for a behavior closer to free $q\bar{q}$-propagation. After that, only the $T = 1.2T_c$ result deviates from the others which may reflect the increasing influence of the phase transition.

Summary of Results on Correlation Functions

Below T_c, one can demonstrate, through investigation of the midpoint of the correlation function, that the pseudoscalar remains a Goldstone boson up to $0.9T_c$. In the vector channel, however, the method is afflicted with large errors, so that a definite conclusion is difficult. However, comparing the results together with screening masses a further support

of a temperature effect in this channel can be obtained.
Above T_c, the pseudoscalar correlation functions still show a pronounced temperature dependence and, neglecting the $N_\tau = 24$ correlation function, only small finite a and volume effects can be observed. In the vector channel their value is of the same absolute magnitude. But as they deviate much less from the free behavior this effect is more pronounced in the ratios shown. Taking the cut-off effects of the free correlators into account, almost no temperature dependence remains in this channel, apart from a small shift at $1.2T_c$. The most important feature of these correlation functions is, however, an enhancement of about 10% over the free ones which persists even at $6T_c$. This is in strong contrast to predictions obtained from HTL-resummed perturbation theory or quasiparticle models. In the former the vector correlation function can not be computed due to a strong IR divergence in the spectral function[74], whereas the latter leads to a suppression of the correlator, as compared to the free case[102, 103].

4.5.3 Meson Properties from the SPF

Another way to get access to the meson mass at finite temperature arises through the analysis of spectral functions. This method has also been introduced in [51]. Here this analysis is extended in the direction of higher statistics, more quark masses and larger volumes. Moreover, the way, this method is implemented in our analysis, has changed somewhat as described in Section 4.4.

SPF below T_c

Some examples of SPF below T_c are shown in Fig. 4.10 for $0.6T_c$ and $0.9T_c$ for the pseudoscalar and vector meson. In this figure only SPF in the region of the ground state peak are shown. The arrows indicate the location of the corresponding screening masses. For all SPF the peak position moves, as expected, with the quark mass, while the peak height decreases with increasing quark mass. Additionally, this height reduces systematically in the pseudoscalar channel by a factor of 2 when the temperature is changed from $0.6T_c$ to $0.9T_c$. In the vector channel the peak height is generally lower and reduces only slightly between these temperatures. Comparing the peak position with the screening masses, one can conclude that they coincide at $0.6T_c$ for both channels. At $0.9T_c$, the pseudoscalar pole and screening mass show only minor deviations whereas in the vector case the difference is more pronounced. The pole masses, obtained from the SPF, are collected in Table A.5 for every single quark mass and for the different channels. Extrapolating these values for the two different volumes separately to the chiral limit leads to the masses listed in Table 4.9.

The scalar mass at $0.4T_c$ is not given in the table, because at the light quark masses no clear peak shows up in the SPF, and the extrapolation to the chiral limit is not possible. The critical hopping parameter, obtained from the vanishing pion mass, only shows a small volume dependence. In the other channels the masses, obtained in different volumes,

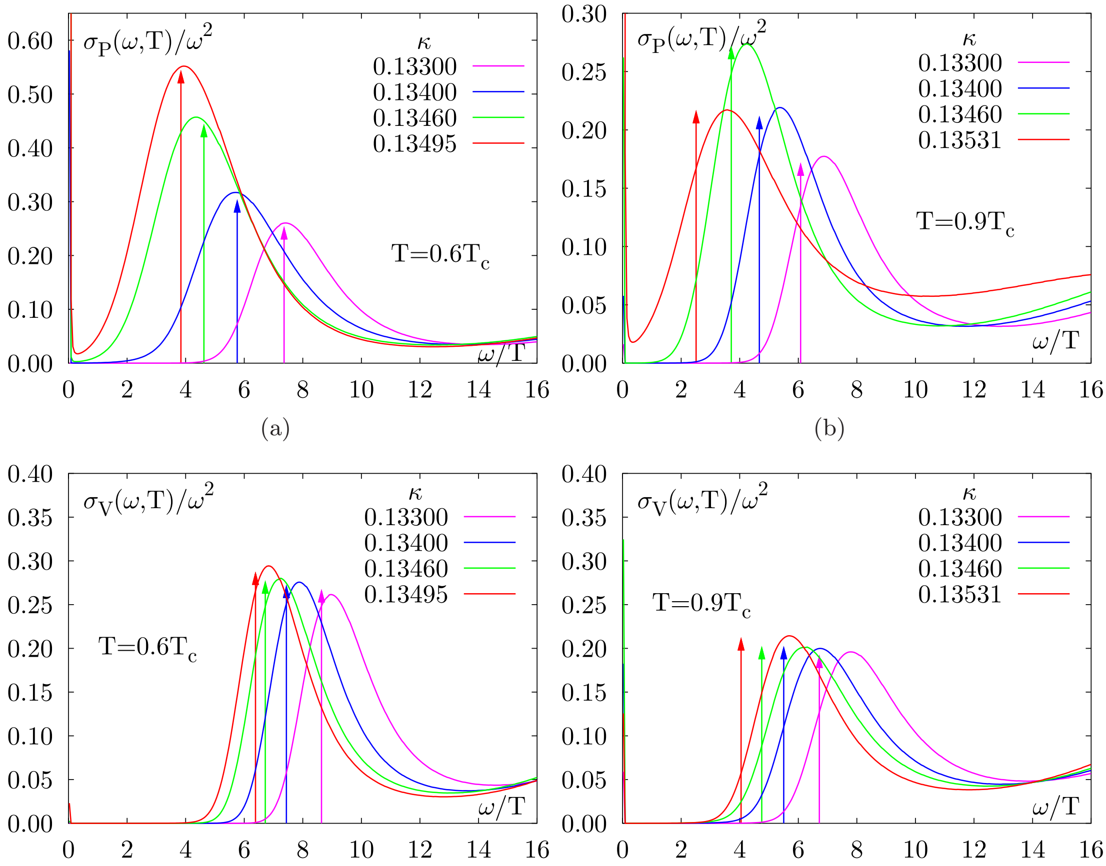

(a) (b)

(c) (d)

Figure 4.10: SPF at $T = 0.6T_c$ (left) and at $0.9T_c$ (right) for the pseudoscalar (top) and the vector meson (bottom), obtained from the $N_\sigma = 32$ lattice. The arrows indicate the location of the screening mass.

differ by about 10%. However, no systematic effect can be observed. In the scalar channel the masses fluctuate also with temperature around a mass of 1.3GeV, whereas in the vector channel the increase with temperature from 0.8GeV at $0.4T_c$ to about 1.2GeV at $0.9T_c$ is systematic. We stress again that the physical volume decreases with increasing temperature, the related finite size effects are also expected to lead to an increasing mass. Although this effect seems to be smaller than the observed one, it hampers a definite

T/T_c	N_σ	κ_c	$m_V a$	m_V[GeV]	$m_S a$	m_S[GeV]
0.9	32	0.13555(5)	0.297(24)	1.192(96)	0.339(8)	1.360(32)
	24	0.13574(4)	0.324(7)	1.300(28)	0.280(10)	1.123(40)
0.6	32	0.13546(4)	0.397(1)	0.948(2)	0.614(11)	1.467(26)
	24	0.13588(1)	0.360(3)	0.860(7)	0.558(14)	1.333(33)
0.4	24	0.13553(12)	0.428(5)	0.815(10)	-	-

Table 4.9: Pole masses in the chiral limit as obtained from the SPF.

statement on a possible temperature dependence of the increasing vector meson mass below T_c.

SPF above T_c

The maximum entropy method is particular useful for calculating SPF at temperatures close to but above the phase transition. In this temperature regime, the coupling is still large and perturbative methods are not applicable. Even phenomenologically it is not clear, whether a correlated $q\bar{q}$-state exists, which would lead to a resonance like structure of the SPF as below T_c. Therefore, little is known about the spectral shape and an approach which does not rely on prior knowledge is necessary. The MEM is such an ansatz. The inherent errors of this method are shown in Fig. 4.11. There the vector SPF at $3.0T_c$ is shown for different lattice sizes (a). Statistical errors in different energy intervals are shown in (b). In (a) the SPF is shown only for the peak region, as the higher energy regions are not even expected to be similar on different size lattices due to the different ultraviolet cut-off (see discussion in Chapter 3). In this region, one can infer from the similarity of the SPFs, obtained on lattices with different spatial extent, $N_\sigma = 32^3$ and $N_\sigma = 64^3$ and fixed $N_\tau = 16$, that they are insensitive to the infrared cut-off. Also the dependence on the ultraviolet cut-off seems to be weak, as the SPF with the same volume, i.e., fixed aspect ratio $N_\sigma/N_\tau = 4$, are also similar. This is in contrast with statements made in [82], where a minimal number of $N_\tau = 30$ was estimated to obtain a reliable SPF. As their numerical set up differs in many details from the one presented here, a direct comparison is, however, difficult. In particular, it is questionable whether their specific approach, i.e., removing points in the short or long distance part from the correlation function allows to draw such a conclusion. Indeed another test performed in [54] at $T = 0$, where points at intermediate steps have been removed systematically, showed that one obtains correct results already for $N_\tau \geq 10$. It thus seems to be important to keep all

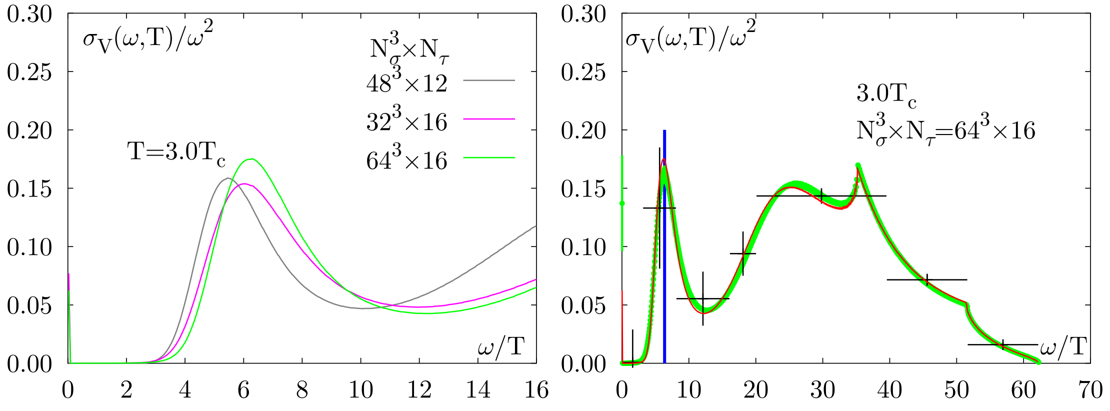

(a) (b)

Figure 4.11: Error estimate for the vector SPF. Systematic errors (a) and statistical one (b). The position and width of the blue line indicate the screening mass and its error.

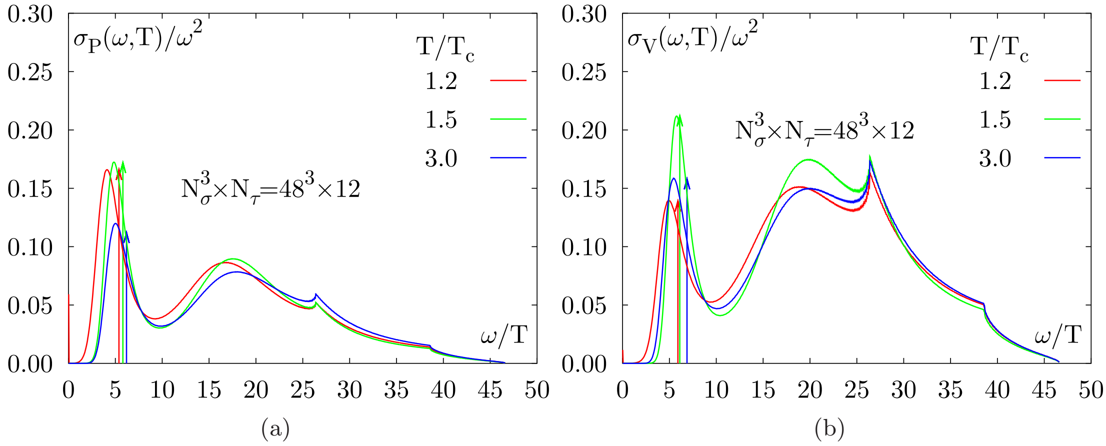

Figure 4.12: Pseudoscalar (a) and vector (b) SPF for different temperatures above T_c, obtained on a $48^3 \times 12$ lattice.

the information available on the correlation functions in the entire time interval $(0, 1/T)$. The size of statistical errors is also shown in Fig. 4.11 (b). There two types of statistical errors are shown. One is the MEM-error, obtained with the covariance matrix of the SPF, Eq.(4.37), which is shown as crosses. The height of the horizontal lines of these crosses represent the mean value, obtained by averaging over the energy bin represented by the extension of this line. The vertical lines present the error on this value. These errors stem from the fact that due to limited statistics the reconstructed SPF is not unique. The pure statistical error can be obtained again from a Jackknife analysis (see Section 2.6) and is shown as a green band.

After having checked that the systematic and statistical errors inherent to this method are under reasonable control, the SPF at $1.2T_c$, $1.5T_c$ and $3.0T_c$ for the pseudoscalar and vector channel have been analyzed. Results are shown in Fig. 4.12. The arrows in the figure again indicate the position of the corresponding screening masses. A general feature

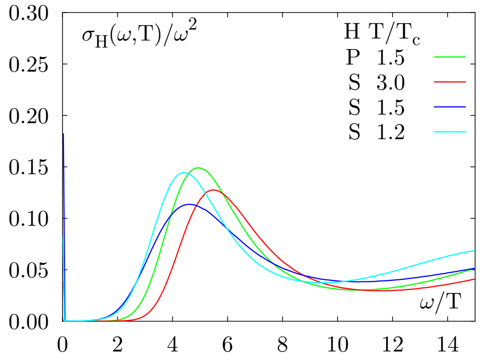

Figure 4.13: Scalar SPF for different temperatures together with the pseudoscaler SPF at $1.5T_c$.

of all these SPF is a pronounced peak between $3 \leq \omega/T \leq 10$ and a broad bump around $\omega/T \simeq 18$ in the pseudoscalar channel and $\omega/T \simeq 20$ in the vector channel. The latter agree with those observed below T_c [95]. The ultraviolet regime, $\omega/T \geq 25$, of these SPF is dominated by the default model, as indicated by the shape and cusps which originate from the free lattice SPF (see Chapter 3). An additional common feature is the scaling of more or less the whole SPF with temperature. For both channels the main difference between the different temperatures is the height of the peak structure in the low energy regime. As already discussed in Section 4.4.2, this depends on details of the MEM analysis, the statistics, N_τ etc.. A clear temperature effect, especially when taking into account the MEM-error, can not be infered. While the peak heights at small ω are at least of the same magnitude in both channels, the broad bump in the SPF above $\omega/T \simeq 10$ is enhanced by a factor of two in the vector channel. As the bump is considered to be a lattice artefact, this supports the finding of Section 4.5.2 that the UV cut-off is more important in the vector channel than in the pseudoscalar channel. At last, the SPF in the scalar channel is shown in Fig. 4.13. In this channel the peak is similar at all temperatures which indicates a temperature scaling also for this channel. The SPF for the pseudoscalar channel at $T = 1.5T_c$ is also given in the figure. It stresses the similarity of correlation functions in these two channels and indicate the effective restoration of the $U_A(1)$ symmetry.

Summary of Medium Effects in the SPF

The temperature dependence of SPF is summarized in Fig. 4.14, where the SPF's from the whole temperature range between $0.4T_c$ and $3T_c$ are shown as functions of the energy in fixed physical units ω/T_c. The quark masses below T_c are chosen to obtain a fixed finite pion mass. At these masses a slight shift of the peak in the vector SPF can be observed. Moreover, the observation that the peak position and the corresponding screening mass disagree, see Fig. 4.10, is itself a signal for medium effects. Hints in this direction have

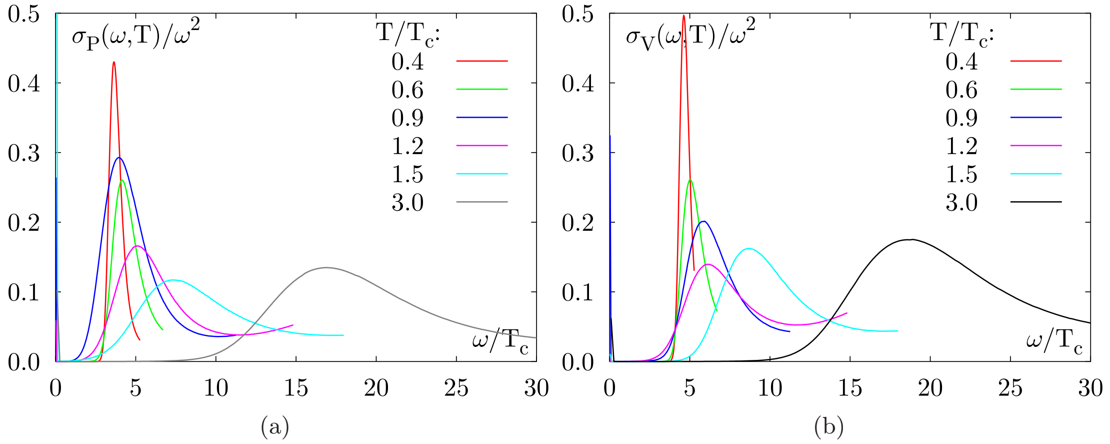

Figure 4.14: SPF at fixed peak in the pseudoscalar channel below T_c and in the chiral limit above T_c for the pseudoscalar channel (a) and the vector channel (b).

already been found in [51]. All this is, however, in contrast with the findings of earlier investigations [52, 99], where no such modifications in the masses have been found. As this effect seems to be small and the correlation functions at $0.9T_c$ indicate for small quark masses frequent exceptional configurations, a more detailed analysis of this effect is still needed.
Above T_c, the MEM results seems to be free from large lattice effects in the low energy regime and provides a unique tool to obtain information of the spectral shape. The main features of the results for all channels are a peak in the low energy regime which indicates that correlations between the $q\bar{q}$-pair still exist above T_c. Another observation is that the entire SPF seems to scale with temperature, which is in contradiction with [82], where a significant change between $1.4T_c$ and $1.9T_c$ has been found. The most important change of their SPF between the two different temperature is a divergence of the SPF in the low energy regime $\omega/T \lesssim 1$ which, however, was not statistically significant. The influence of such a divergence on the high energy behavior and its appearance due to some details of the MEM approach has already been discussed in Section 4.4.2.

4.6 Dilepton Production in Heavy Ion Collisions

One important experimental observable in heavy ion collisions is the dilepton production as already discussed in the introduction. An excess of the dilepton rate in the region of low invariant mass M of the dilepton, $250\text{MeV} \leq M \leq 770\text{MeV}$, has been found and attributed to non-perturbative effects[104] at $T < T_c$. The most conventional explanations consider in-medium modifications of the ρ meson properties. One suggestion was that the ρ meson mass drops near T_c[105] whereas other explanations are based on a broadening of the ρ resonance[4]. The results, obtained in Section 4.5, disfavor the first explanation.The second explanation can in principle also be checked within a statistical apporach based on the maximum entropy method. The broadening, however, is expected to be due to interactions with pions which are, at least, not present with ther full dynamics in the quenched approximation, i.e., dynamical simulations are necessary. These are however at present completely unaffordable in computing time. Another excess in the dilepton rate has been seen in the intermediate mass region of $1\text{GeV} \leq M \leq 3\text{GeV}$[10]. A model calculation in [106] suggest, that contributions from the QGP play an important role in this region. Although medium effects are estimated to be small, at least the low energy region in the perturbative calculations is not under control[106, 107]. Hence a non-perturbative calculation of this rate, especially at low energies, is desirable and will be presented in the following.

4.6.1 The thermal Dilepton Rate from the Lattice

The dilepton rate can be written as [7]

$$\frac{\mathrm{d}^8 N}{\mathrm{d}^4 x \mathrm{d}^4 q} = \frac{\mathrm{d}^4 W}{\mathrm{d}q^4} = L_{\mu\nu}(q) H^{\mu\nu}(q) \qquad (4.46)$$

where the lepton tensor $L_{\mu\nu}$ encodes the propagation of a virtual photon and its decay to a lepton pair. It is in lowest order in α given for vanishing lepton masses by

$$L_{\mu\nu}(q) \quad = \quad -\frac{\alpha^2}{6\,\pi^3 M^2}\left(g_{\mu\nu} - \frac{q_\mu q_\nu}{M^2}\right) \,, \tag{4.47}$$

with $q^2 = M^2$, the invariant mass of the lepton pair. The hadron tensor is given by

$$H_{\mu\nu}(q) \quad = \quad \int \mathrm{d}^4x\; e^{iqx} \langle \mathcal{J}^\mu_{em}(0)\mathcal{J}^\nu_{em}(x)\rangle \tag{4.48}$$

$$= \quad -2\,\frac{1}{\exp(\omega/T)-1}\;\mathrm{Im}\;\Pi^{\mu\nu}_{em}(q) \,, \tag{4.49}$$

where $\mathcal{J}^\mu_{em}$ is the electromagnetic current. Contracting the imaginary part of the electromagnetic propagator, $\mathrm{Im}\;\Pi^{\mu\nu}_{em}$, leads to the dilepton production rate

$$\frac{\mathrm{d}^4W}{\mathrm{d}^4q} \quad = \quad -\frac{\alpha^2}{\pi^3 M^2}\frac{1}{\exp(\omega/T)-1}\;\mathrm{Im}\;\Pi_{em}(\omega,\mathbf{q},T) \tag{4.50}$$

$$= \quad \frac{5\,\alpha^2}{27\,\pi^3\omega^2}\frac{1}{\exp(\omega/T)-1}\sigma_V(\omega,\mathbf{q},T) \,, \tag{4.51}$$

where, for the second line, the two flavor case and vector dominance[108] has been assumed. To obtain the total yield,

$$\frac{\mathrm{d}N^{th}}{\mathrm{d}M} \quad = \quad \int\limits_{\tau_0}^{\tau_f} \mathrm{d}\tau\; V(\tau) \int \mathrm{d}^3q\; \frac{M}{\omega}\;\frac{\mathrm{d}^4W}{\mathrm{d}^4q} \,, \tag{4.52}$$

the rate has to be integrated over the momentum and evolved over the space-time history of the system. Here, τ is the proper time of the system of volume V formed at τ_0. At τ_f, the chemical freeze-out is reached and the abundances are fixed. This evolution is model dependent[109, 110, 111] and will not be performed in this work.

Here we will concentrate on the differential dilepton rate, which is directly computed with the vector SPF as given in Eq.(4.50). The free continuum vector spectral function $\sigma(\omega) = 0.75(\omega/\pi)^2\tanh(\omega/4T)$ in the chiral limit and at vanishing momentum $\mathbf{p} = \mathbf{0}$, Eq.(3.6) leads to the Born rate

$$\frac{\mathrm{d}W^{Born}}{\mathrm{d}\omega\mathrm{d}^3p}(\omega,\mathbf{p}=\mathbf{0}) \quad = \quad \frac{5\alpha^2}{36\pi^2}\frac{1}{(\exp(\omega/2T)+1)^2} \tag{4.53}$$

and is shown in Fig. 4.16. The SPF's which are shown in Fig. 4.15 and Fig. 4.11 with errors, lead to the thermal dilepton rate also shown in this figure. These rates, obtained in the interacting case, show two pronounced features. One is a suppressed dilepton production in the IR region below $\omega/T \leq 3-4$ and an enhancement between $4 \leq \omega/T \leq 8$. Both features are due to the pronounced peak shape of all the SPF's in this region which is significant with the errors shown. As already explained above, hints for both features have additionally been obtained from the correlation function and are, as discussed above,

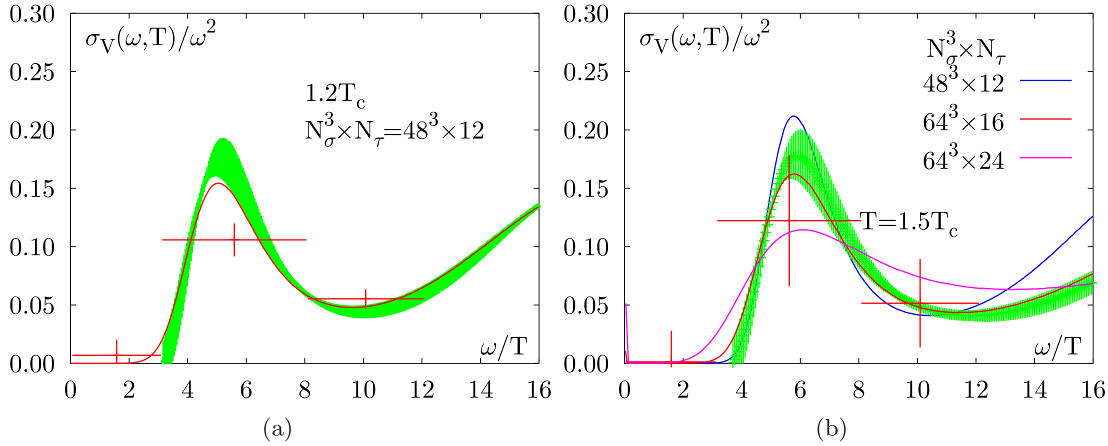

Figure 4.15: Vector SPF for $1.2T_c$ (a) and $1.5T_c$ (b) for different lattice sizes and different errors.

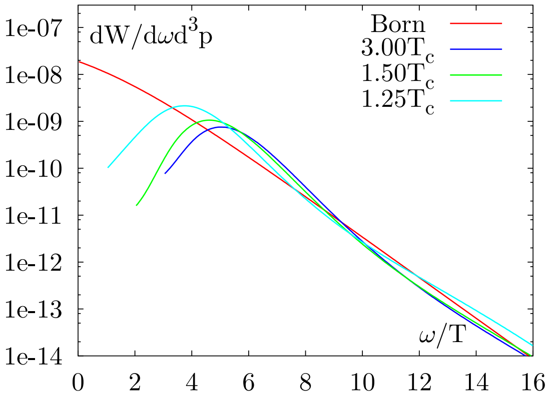

Figure 4.16: Thermal Dilepton Production Rate in the QGP phase.

in contrast to perturbative calculations. The high energy region above $\omega/T \geq 8$ is, as expected, close to the Born rate.

A careful study of the systematics of the MEM analysis shows that with increasing temporal lattice size, N_τ, or decreasing lattice spacing a the analysis becomes more sensitive to the UV-structure of the default model. This technical problem is explained in more detail in the Section 4.6.3. It also is the reason why the $N_\tau = 24$ data have been neglected so far in our analysis of the dilepton rate.

4.6.2 Criticism of the approach

It has been pointed out by G. Moore[112] that the electrical conductivity, which is given by

$$\sigma_{el} = \lim_{\omega\to 0} \frac{\sigma_V(\omega, \mathbf{p}=0)}{6\omega} , \qquad (4.54)$$

should be non-vanishing in the QGP-phase. This requires that $\sigma_V(\omega) \propto \omega$ which necessarily leads to a diverging dilepton rate at low ω. This behavior is estimated to be correct up to energies of oder $\omega/T \simeq 1$ [113]. As the maximum entropy method is not able to reproduce these behavior, it is interpreted as a failure of the maximum entropy method due to an infrared insensivity of the lattice. However, a large contribution at small ω would also lead to a significant contribution in the correlator at the largest distances. This can be checked with the data shown in Fig.4.9(d) in which no such contribution is present. A further check of this infrared sensitivity has been made on a $64^3 \times 8$ lattice at $3.0T_c$, which increases the volume by a factor 64 compared to the $32^3 \times 16$ lattice and also does not show the expected IR contributions[114]. Thus, also a finite volume effect can not be responsible for infrared insensitivity of the lattice. In [115] it has been pointed out, however, that the very low ω region of the SPF, i.e., $\omega \ll T$, contributes only to a τ independent constant to the correlation functions. Therefore, one has to reconstruct the behavior of the SPF in this region from a single constant alone which leads to serious difficulties in extracting quantities like transport coefficients within this approach. Additional difficulties in the calculation of such quantities arise with sensitivity of the smallest bin to some details in the MEM approach. (see Section 4.4). Both considerations show that calculations of dilepton rates at very small energies require additional efforts and puts some doubts of the transport coefficients obtained in [116].

4.6.3 Implications for the Dilepton Rate from the Correlation Function

To understand the UV-sensitivity of SPF in calculations with large N_τ it is helpful to consider the contributions of different energy ranges to the correlation function. A first estimate can be obtained by using the free lattice SPF. Relating in this approximation the contribution to the correlation function for a given energy range I to the one obtained

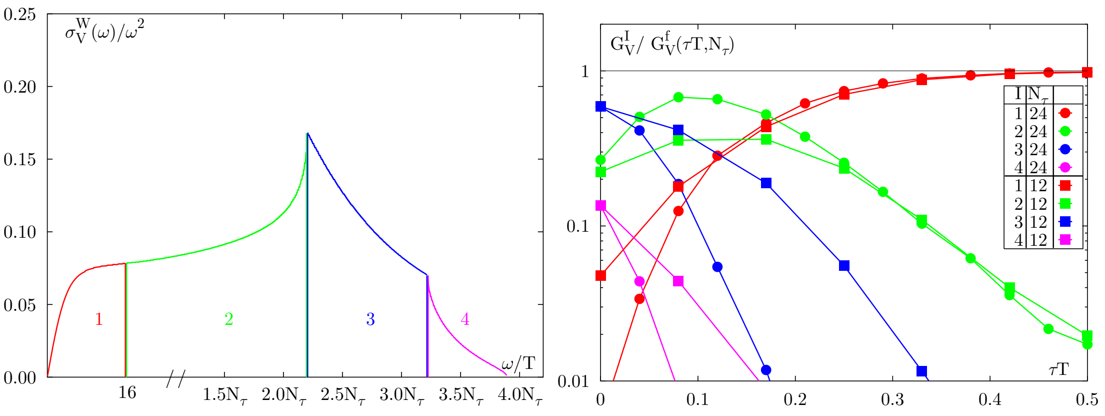

(a) (b)

Figure 4.17: Contribution of the different regions of the SPF (a) to the correlation function (b).

T/T_c	N_τ	N_σ^3	$\frac{G_V}{G_V^W}(\tau T=\frac{1}{2})$
6.00	8	32^3	1.095(10)
3.00	16	64^3	1.093(11)
	16	32^3	1.075(12)
	12	48^3	1.080(11)
	8	32^3	1.110(10)
1.50	24	64^3	1.107(15)
	16	64^3	1.096(19)
	12	48^3	1.117(16)
1.24	12	48^3	1.154(15)

Table 4.10: $G_V/G_V^W(\tau T = 0.5)$ for different lattice sizes and different temperatures.

from the full energy range leads to Fig. 4.17(b), where the ratio

$$\frac{G_V^I}{G_V^f}(\tau T) \equiv \int\limits_I \sigma(\omega)\, K(\omega,\tau T)\, \mathrm{d}\omega \Bigg/ \int\limits_0^{\omega_{max}} \sigma(\omega)\, K(\omega,\tau T)\, \mathrm{d}\omega \quad I \subset [0,\omega_{max}] \tag{4.55}$$

is plotted (b). The first interval, $0 \le \omega/T \le 16$, is chosen to contain the peak appearing in the SPF shown in Fig 4.11. The others are bounded by the edges of the Brillouin zones. As one can see, the region $I = 1$, where in interacting case the peak is located, contributes over 98% to the large distance part of the correlation function independent of N_τ. In the short distance part, up to $\tau T \le 0.3$, the dominant contribution comes from the region $I = 2$ and at least one other region of nearly the same importance, which changes from $I = 3$ to $I = 1$ with the increasing distance. Apart from $\tau a = 1$ in the $N_\tau = 24$ case, the UV-region $I = 4$ contribution is dominated by contributions of every other single region. On small lattices even the shortest distance thus is dominated by the contribution from the IR regime (I=1) while with increasing N_τ all the other regions start gaining importance.

This allows us to relate the correlation function at long distances, especially the value of $G_V(\tau T = 0.5)$ listed in Table 4.10, to the low ω region, $I = 1$, of the SPF. As the correlation function shows an enhancement of approximately 10% as compared to the free one, see Fig. 4.9(d), this has to come from an enhancement of the SPF, also compared to the free one, in this energy interval. This can indeed be observed in Fig. 4.11 for $3.0T_c$ and in Fig. 4.15 for $1.2T_c$ and $1.5T_c$. Moreover, this behavior of the correlation function is almost independent of temperature, at least for the values analyzed here. It also is independent of the UV- or IR lattice cut-off. This is also reflected in the aforementioned SPF. Another statement can be infered from the fact that the correlation function shows almost no volume dependence, although the volume of the lattices analyzed differs by a factor 100. Hence, one can safely expect, that the correlation function also stays finite in the thermodynamic limit. The SPF thus has to vanish in the IR limit, which can be seen, if one assumes an IR behavior of $\sigma_V(\omega) \propto \omega^r$. The correlation function calculated

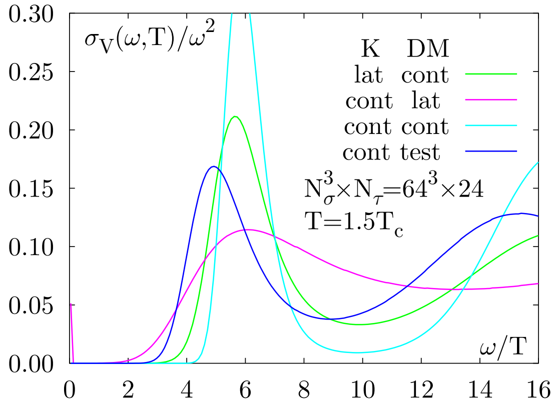

Figure 4.18: Influence of the default model and the choice of the kernel on the vector SPF with $N_\tau = 24$.The abbreviations are the same as Fig.4.3.

at $\tau T = 0.5$ would diverge for $r \leq 0$:

$$G_V(\tau T = 0.5) \overset{a<b\ll 1}{>} \lim_{a\to 0} \int_a^b \frac{\sigma_V(\omega, T)}{\omega/T}\, \mathrm{d}\omega = \left\{ \begin{array}{ll} \frac{1}{r} \lim\limits_{a\to 0} (b^r - a^r)\ , & r < 0 \\ \lim\limits_{a\to 0} \left(\log \frac{b}{a}\right)\ , & r = 0 \end{array} \right\} \longrightarrow \infty \quad (4.56)$$

This simple fact is already in contrast with the 2-loop perturbative calculations [117] or the HTL resummed perturbation theory [118], where a diverging spectral function has been found.

Now the mentioned problem with the $N_\tau = 24$ data can be discussed. From Fig. 4.15 one can conclude that a large systematic N_τ effect is visible and may lead to a vanishing of the peak at this temperature, although this feature is not shared by the SPF at the temperatures above or below. This is also in contradiction with the expectation that the peak height should increase with N_τ as explained in Section 4.4.2 and is mostly due to difficulties which occured with decreasing a, i.e. for our $N_\tau = 24$ data. Already in the pseudoscalar channel large deviations from results obtained with smaller N_τ, have been observed (see Fig. 4.9). As noted above the UV $I = 4$ contribution, in contrast to the IR $I = 1$ one, becomes more important for the short distance regime with increasing N_τ. This explains why the $N_\tau = 24$ SPF is more sensitive to the UV-part of the default model. For large N_τ the MEM analysis thus becomes sensitive to details in a much larger energy regime. To suppress the UV-sensitive part, which is strongly influenced by lattice effects, we have omitted the first point in the SPF[4]. Nevertheless, the level of the covariance matrix smoothing (see Section 4.4.2) which can be used for the $N_\tau = 24$ data remains unsatisfactory. A more detailed investigation of this interpretation is presented in Fig.4.18, where the effect of using different kernels and default models, including a test model where the free lattice SPF is replaced by a constant of 0.75 above $\omega/T = 75$, is shown. They all give a stable peak, however, the peak heights and widths differ significantly between the various combinations of the default model and kernel. This demonstrates the sensitivity of the SPF on the default model in the deep UV-region and may be a hint, that the tree

---

[4] This is the same procedure as has been utilized in [82] for all SPF.

level calculation of the SPF seems to be improvable even for these high energies. This is, however, the “worst case”, as all other SPF are much less sensitive to these details.

4.6.4 Calculating the Photon Rate

Every process, which can produce a dilepton pair can, in principle, also produce a photon, which from an experimental point of view has the same favorable features as dileptons, i.e., a mean free path long enough to escape the medium without further interactions. As they are closely related to each other, it is not surprising that also an excess of direct photons[5] has been found by the WA80 collaboration [119] in central S+W collisions. In the case of the photon rate, the analog of the cocktail in the dilepton rate is considered as an additional background contribution. 90% of the produced photons at full SPS energies stem from π and η decays[4] included in these background contributions. Therefore, the rate is expected to be two orders of magnitudes less sensitive to in medium effects as compared to the dilepton rate. Hence, these rates have to be measured experimentally very precisely to obtain the wanted information.

---

[5] “Direct” means, the photon is produced in the interacting phase of the fireball.

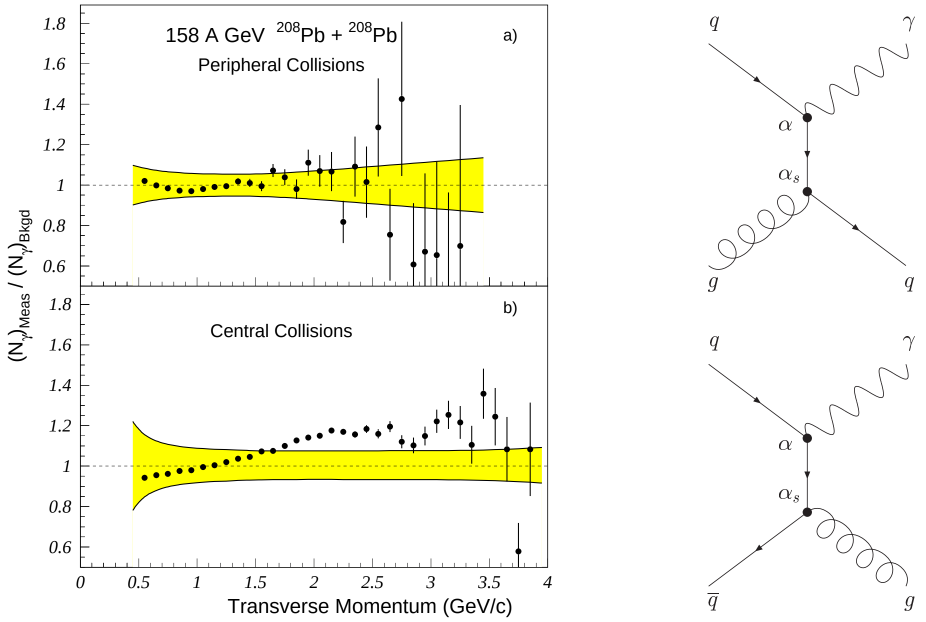

(a) (b)

Figure 4.19: (a) Direct photon excess measured in Pb+Pb collisions[120] at 158AGeV. The errors in the data points include the statistical errors only. The systematical errors are shown by the yellow band. (b) Lowest order photon production processes.

The calculation of the photon rate is analogous to Eq.(4.46)

$$\frac{\mathrm{d}^8N^\gamma}{\mathrm{d}x^4\mathrm{d}q^4} = \frac{\mathrm{d}^4R^\gamma}{\mathrm{d}q^4} = P_{\mu\nu}H^{\mu\nu} , \tag{4.57}$$

with the photon tensor [121]

$$P_{\mu\nu} = 4\pi\alpha \int \frac{\mathrm{d}^3p}{(2\pi)^3 2p_0} \sum_\lambda \epsilon_\mu(\lambda,p)\epsilon_\nu(\lambda,p)\delta^4(p-q) . \tag{4.58}$$

This photon rate can be rewritten as

$$\omega\frac{\mathrm{d}^3R^\gamma}{\mathrm{d}q^3} = \frac{\alpha}{4\pi^2}g_{\mu\nu}H^{\mu\nu}(\mathbf{p}) \tag{4.59}$$

$$= \frac{5\alpha}{6\pi^2}\frac{1}{\exp(\omega/T)-1}\sigma_V(\omega=|\mathbf{p}|,T) , \tag{4.60}$$

where vector meson dominance and the two flavor case have been assumed again. This formula is correct to first order in α and to all orders in α_s. Perturbatively, the lowest order processes for photon production are shown in Fig. 4.19 and are of order $\alpha\alpha_s$, i.e., there is no photon production in the free field theory, i.e., $\alpha_s = 0$. This can also be seen from the vector spectral function in the continuum theory for vanishing quark mass [122]

$$\begin{aligned}\sigma_V(\omega,\mathbf{p}) &= \frac{3}{4\pi^2}(\omega^2-\mathbf{p}^2)\left\{\Theta(\omega^2-\mathbf{p}^2)\frac{2T}{p}\ln\frac{\cosh(\frac{\omega+p}{4T})}{\cosh(\frac{\omega-p}{4T})}\right.\\ &\quad\left.+\Theta(\mathbf{p}^2-\omega^2)\left[\frac{2T}{p}\ln\frac{\cosh(\frac{\omega+p}{4T})}{\cosh(\frac{\omega-p}{4T})}-\frac{\omega}{T}\right]\right\} ,\end{aligned} \tag{4.61}$$

which vanishes at the photon point $\omega^2 = \mathbf{p}^2$. Kapusta et. al.[121], computed the photon rate within the HTL-resummation scheme and found a photon rate for two quark flavors

$$\omega\frac{\mathrm{d}^3R^\gamma}{\mathrm{d}q^3} = \frac{5\alpha\alpha_s}{18\pi^2}T^2e^{-\omega/T}\ln\left(1+\frac{2.912}{4\pi\alpha_s}\frac{\omega}{T}\right) \quad \text{with} \quad \alpha_s(T) = \frac{6\pi}{33\ln(8T/T_c)} , \tag{4.62}$$

which should be valid for $\omega/T \gg 1$. A more detailed calculation (see [123] for a review of this topic) yields only a slightly enhanced rate.

The computation in the free lattice theory starts, as in Chapter 3, with the computation of the free lattice correlation function

$$\tilde{G}_V^W(\tau,\mathbf{p}) = \int_{-\infty}^{\infty} \mathrm{d}^3k \sum_\mu \gamma_5\gamma_\mu S^W(\tau,\mathbf{k}+\mathbf{p})\gamma_\mu^\dagger\gamma_5 S^{W\dagger}(\tau,\mathbf{k}) \tag{4.63}$$

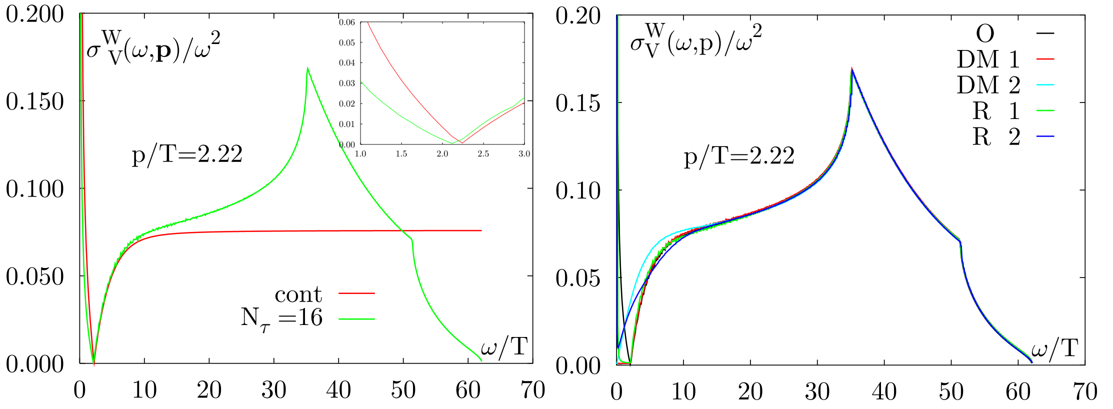

(a) (b)

Figure 4.20: (a) Free continuum vector SPF together with the free lattice SPF for $|\mathbf{p}|/T = 2.22$. The insertion shows these SPF in the region around the photon point in more detail. (b) The reconstructed SPF from the free lattice correlation function obtained with MEM with different default models.

which, together with the lattice quark propagator $S^W(\tau,\mathbf{k})$, Eq.(3.18), leads to

$$\begin{aligned}
\tilde{G}^W_V(\tau T,\mathbf{p}) &= \int \mathrm{d}^3k\; G^d_V(\mathbf{k},\mathbf{p})\cosh(E_d N_\tau(\tau T-0.5)) \\
&\quad + \int \mathrm{d}^3k\; G^s_V(\mathbf{k},\mathbf{p})\cosh(E_s N_\tau(\tau T-0.5))\,, \\
G^d_V(\mathbf{k},\mathbf{p}) &= \frac{K_{12}+2\tilde{M}_1\tilde{M}_2+\cosh(E_d)+3\cosh(E_s)-2\tilde{M}_1\cosh(E_2)-2\tilde{M}_2\cosh(E_1)}{\cosh(E_1N_\tau/2.0)\cosh(E_2N_\tau/2.0)\tilde{M}_1\tilde{M}_2\sinh(E_1)\sinh(E_2)}\,, \\
G^s_V(\mathbf{k},\mathbf{p}) &= \frac{K_{12}+2\tilde{M}_1\tilde{M}_2+3\cosh(E_d)+\cosh(E_s)-2\tilde{M}_1\cosh(E_2)-2\tilde{M}_2\cosh(E_1)}{\cosh(E_1N_\tau/2.0)\cosh(E_2N_\tau/2.0)\tilde{M}_1\tilde{M}_2\sinh(E_1)\sinh(E_2)}\,.
\end{aligned} \tag{4.64}$$

Here the notation of Chapter 3 has been used. Additionally, the short hand notations $\mathcal{B}_i$, if a function depends on $\mathbf{k}+\mathbf{p}$ $(i=1)$ and $\mathbf{k}$ $(i=2)$, and $\tilde{M}_i = 1+M_i$ have been introduced. This expression allows the usage of the binning procedure described in Section 3.2.4 to obtain the free lattice SPF. The result is shown in Fig. 4.20(a) together with the continuum SPF at the meson momentum of $|\mathbf{p}|/T = 2.22$. The insertion shows the relevant region around the photon point in more detail. In Fig. 4.20(b) the reconstruction of the SPF from the free lattice correlation function with the MEM is shown. The mock data are generated for a $N_\tau = 16$ lattice with a noise of $b = 0.01$ (see Section 4.4.2) for 400 datasets. Utilizing these data, the SPF are reconstructed with a default model (DM 1) with the free lattice SPF above the photon point and a tiny constant value below and with the default model of the free lattice SPF at vanishing meson momentum (DM 2). The correct SPF is also shown for comparison and labeled with (O), which is perfectly reproduced if it is chosen as the default model itself. For both other default models, the reconstructed SPF coincide with the correct SPF in the UV regime. For the first SPF the region of the correctly reproduced SPF extends to the photon point, whereas choosing the SPF with the wrong momentum

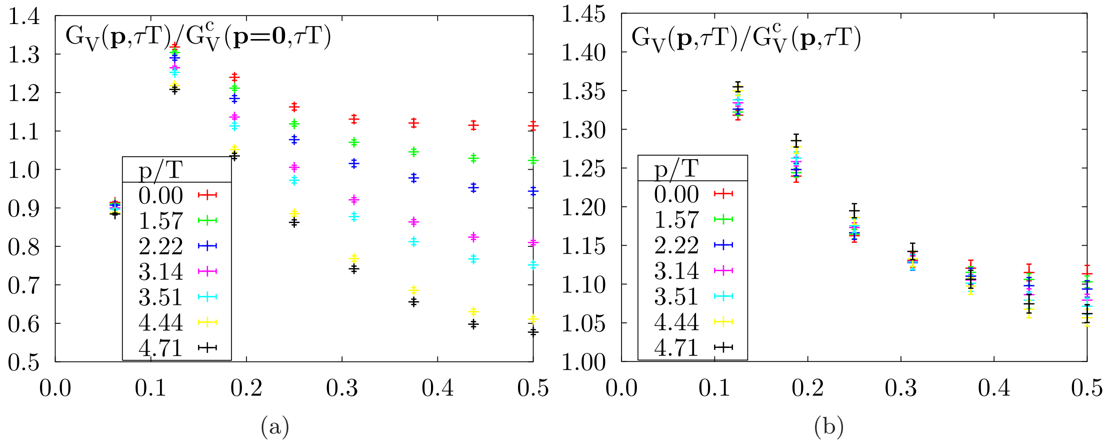

(a) (b)

Figure 4.21: Correlation function at different momenta normalized with the continuum correlation function at vanishing momenta (a) and with the correlation function with varying momenta (b).

the deviations set in already at $\omega/T \simeq 10$. In the IR region both reconstructed SPF show a diverging SPF, which lies, however, considerably below the expected one. Hence, the region around and below the photon point is strongly influenced by the default model which has to be taken into account in the discussion of the photon rate.

First the influence of non-vanishing momenta on the correlation function is investigated. Fig.4.21(a) shows it for the vector channel at $T = 3T_c$ on the $N_\sigma^3 \times N_\tau = 64^3 \times 16$ lattice for the different momenta available as an example. The correlation functions are all normalized to the continuum free correlation function at vanishing momenta for better visibility. Hence, this figure demonstrates the absolute momentum dependence and shows a smooth decrease of the midpoint of the correlation function with increasing momentum up to 50% for the largest momentum of $|\mathbf{p}|/T = 4.71$. This can not be compensated by a normalization with the continuum free correlation function at the appropriate momenta, as demonstrated with Fig. 4.21(b). Hence the interactions still play a significant role even at this temperature and at high momenta. The short distance regime is again dominated by cut-off effects but at large distances the ratio of the correlation functions with larger momenta are getting closer to one, as it is expected for correlation functions less influenced by interactions.

Using the MEM in the way done in Section 4.4.2, i.e., with the free lattice SPF as the default model, leads to the SPF shown in Fig. 4.22(a), together with the two different errors. As in the free case the interesting region around the photon points strongly dependent on the default model, this dependence is checked here also. This is done in Fig. 4.22(b) with the zero momentum SPF as the default model as the worst case. In both cases the SPF vanish at low frequencies, hence this feature is in contrast to the free theory independent of the default model.

All SPF's are obtained from now on with the "correct" default model, i.e., the free lattice SPF at the appropriate momenta. The value of the SPF's at the photon point obtained in

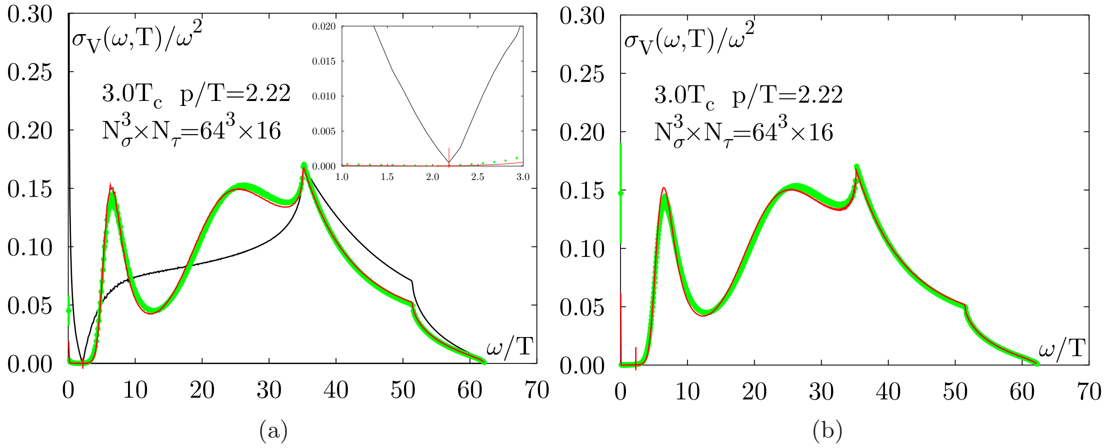

(a) (b)

Figure 4.22: The vector SPF in the free and in the interacting case for $|\mathbf{p}|/T = 2.22$ at $3T_c$ obtained from the default model at the correct momentum (a) and at vanishing momentum (b).

this way and the resulting photon rate calculated via Eq.(4.62) for the different momenta, are listed in Table 4.11 together with the statistical error. The appropriate photon point, which can be shifted by lattice artefacts, is chosen as the energy of the dip in the free lattice SPF, as this is a common feature in the SPF at this point on the lattice and in the continuum. As one can observe, the errors on these rates are quite large and therefore, the photon rate often vanishes within the statistical error. Only at large momenta, $|\mathbf{p}| \geq 4.44$ non-vanishing rates have been obtained for $N_\tau = 16$. The $N_\tau = 12$ data have large errors and are, within the errors, compatible with the $N_\tau = 16$ data and 0. Therefore, only a maximal value, obtained from the MEM average over the bin of the photon point and the two adjacent ones plus the error on the SPF, Eq.(4.37), is given in the last row of the table. Even these maximal values are, at small momenta, only 10% of the perturbative one, as obtained from Eq.(4.62). As the perturbative rates decrease with increasing momenta, they are getting closer to the non-perturbative bounds, which at fixed temperature, remain at an approximately constant level. Although these calculations are still explorative, they indicate a considerable smaller photon rate as compared to the perturbative ones. The perturbative calculations are expected to become more reliable at large momenta, where they get into contact with the upper non-perturbative bounds obtained here. Nevertheless, a detailed analysis, with largely increased statistics is necessary to show that these values are really vanishing or only very small.

T/T_c	$\vert\mathbf{p}\vert/T$	$\omega d^3R^{HTL}/dq^3$	$N_\tau\times N_\sigma^3$	σ_V	$\omega d^3R/dq^3$	$\omega d^3R^{max}/dq^3$
		[GeV^{-2}fm^{-4}]	$\times$	[GeV^{-2}]	[GeV^{-2}fm^{-4}]	[GeV^{-2}fm^{-4}]
1.5	1.57	955	16×64^3	0.3(3.4)	0.04(43)	70
			12×48^3	0.2(1.6)	0.03(20)	24
	2.22	617	16×64^3	1(16)	0.06(96)	45
			12×48^3	1(7)	0.07(38)	18
	3.14	299	16×64^3	17(65)	0.39(151)	39
			12×48^3	6(20)	0.14(46)	71
	3.51	218	16×64^3	45(84)	0.70(133)	58
			12×48^3	9(4)	0.13(37)	77
	4.44	97	16×64^3	388(185)	2.48(119)	69
			12×48^3	84(150)	0.55(97)	67
	4.71	76	16×64^3	349(156)	1.74(78)	63
			12×48^3	64(102)	0.35(55)	31
3.0	1.57	3821	16×64^3	4(2)	0.49(11)	346
			12×48^3	0.9(123)	0.12(155)	115
	2.22	2468	16×64^3	9(4)	0.56(5)	237
			12×48^3	21(52)	1.21(294)	154
	3.14	1194	16×64^3	27(10)	0.62(3)	146
			12×48^3	49(179)	1.12(408)	283
	3.51	874	16×64^3	43(15)	0.67(2)	160
			12×48^3	80(200)	1.23(308)	503
	4.44	387	16×64^3	265(90)	1.70(3)	119
			12×48^3	1122(1216)	7.30(792)	613
	4.71	304	16×64^3	261(104)	1.30(3)	112
			12×48^3	1330(1337)	7.17(721)	361

Table 4.11: Value of the SPF at $\omega = |\mathbf{p}|$ and the resulting photon rate together with the upper bound and the perturbative value from Eq.(4.62).

Conclusions

> *The world is round and the place which may seem like the end may also be the beginning.*
>
> Ivy Baker Priest

In this work, medium effects in mesonic observables have been investigated. The influence of lattice artefacts on the observables has been discussed in detail. In particular, the influence of these effects on the structure of spectral functions has been investigated in the lattice free field theory. Here, a first calculation has been presented for different fermion actions. Additionally, the maximum entropy method has been applied to thermal correlation functions which allow to calculate the meson spectral functions. In the vector channel this has lead to a first nonperturbative calculation of the thermal dilepton and photon production rate.

In the lattice free field theory, the thermal two-point correlation function arises from a three dimensional momentum integral over the current-current expectation value. After rewriting this integral as a one dimensional energy integral the integrand factorizes in two parts. One factor could be identified with the thermal continuum boson kernel and the other factor is interpreted as the free lattice spectral function, as it is analogous to the continuum spectral function in the spectral representation of the correlation function. Hence it has be found that lattice artefacts do not modify the integration kernel, but show up in the spectral function.

This analysis has been performed for two different fermion formulations: the Wilson fermion discretization scheme with an arbitrary Wilson coefficient and an improved truncated fixed point action. A close relation between the dispersion relation of free quarks on the lattice and the corresponding mesonic spectral function, has been established for all parameters of these actions. In the infrared region, a remnant of chiral symmetry, which is explicitly broken in these fermion formulations, shows up in the spectral function. In the ultraviolet region, it could be demonstrated that the lattice artefacts in the spectral function are related to a sudden restriction of the quark momenta at the corners of the Brillouin zone. Moreover, it has been shown that lattice artefacts are only controlled by the energy scale ωa and do not explicitly depend on $N_\tau = 1/Ta$ as do, for instance, bulk thermodynamic properties, e.g., the energy density

In this way, also several improvements of the correlation function on the lattice could be checked. For Wilson fermions, it has been shown that the choice $\xi = 1/r > 1$, which should improve the fermion formulation at large quark masses, indeed leads to an improved spectral function in a small infrared regime. This leads, however, also to strongly enhanced lattice artefacts at higher frequencies. An improvement of the spectral function through the usage of anisotropic lattices could be established in the vector and pseudoscalar channel, but leads to an even stronger chiral symmetry breaking effect. The truncated fixed point fermion formulation highly improves the dispersion relation and therefore also the lattice spectral function. Explicit chiral symmetry breaking and the contribution of lattice artefacts are shifted deeply in the ultraviolet region. Therefore, an investigation with this fermion formulation is promising, in particular to resolve the origin of the broad bump at $\omega a \simeq 2$, visible in all spectral functions. The analytic calculations performed in the free field theory also allow a clean separation of different frequency contributions to the correlation function and show the lattice distortion effect on these observables. This has been particularly useful, because the influence on improved meson operators could be demonstrated, i.e., we could explicitly demonstrate that ultraviolet contributions, for which the lattice artefacts dominate, are strongly suppressed in favor of an enhanced sensitivity to infrared properties on the lattice. This operators seem to be also an interesting tool to resolve the broad bump question mentioned before.

The second part of this work started with the investigation of the quark mass as obtained from the axial Ward identities in the deconfined phase. Below T_c now temperature effected could be observed, whereas above T_c deviations to the $T = 0$ results have been obtained. The interpretation of this effect, however, need more detailed investigations. Moreover, the temperature dependence of meson properties is investigated through an analysis of screening masses, the midpoint of temporal correlation functions and spectral functions. At $0.9T_c$ medium effects in the vector channel become important as could be infered from all three observables. These effects, however, seem to increase the vector meson mass rather than to decrease it, as some arguments based on chiral symmetry restoration suggested. This excludes one class of models, which assume a decreasing ρ meson mass to explain the low mass enhancement of the dilepton rate observed in relativistic heavy ion collision. To measure the magnitude of these effects, finite volume effects, which are still relevant for the currently available lattice sizes, have to be eliminated and better statistics is necessary. In the pseudoscalar channel no such temperature effect could be observed, i.e., it could be demonstrated that the pion remains a Goldsone boson up to $0.9T_c$.

Above T_c chiral symmetry restoration including effective $U_A(1)$ restorations at temperatures between $1.2 \leq T/T_c \leq 1.5$ has been observed in the screening masses by investigating the scalar/pseudoscalar and the vector/axial-vector channels. However, also the analysis presented here could not resolve the known discrepancies between screening masses obtained from staggered and Wilson fermion formulations.

In the Wilson fermion formulation, used in this work, the pion channel remains temperature dependent up to $6T_c$ whereas the vector meson channel seems to be rather close to free $q\overline{q}$-propagation for all temperatures investigated here, i.e., between $1.24T_c$ and $6.0T_c$. A slight deviation observed in the temporal correlation function at $1.24T_c$ from the signals at higher temperatures suggests a stronger modification at lower temperatures. Hence, investigations closer to the deconfinement transition will be interesting. The spectral function, however, seems to scale with temperature and thus seems to be less sensitive to the small temperature effects visible in the correlation function.

Although correlation functions and spectral functions in the vector channel are close to the free case, which is reflected in their scaling with T, the remaining small correlation between the $q\overline{q}$ pair leads to significant deviations from the free spectral functions in the infrared regime. These deviations consist in a suppression of the spectral function below $\omega/T \lesssim 4$ and a small but significant peak around $4 \lesssim \omega/T \lesssim 8$. The ultraviolet region, $\omega/T \gtrsim 16$ is strongly influenced by cut-off effects. The first two features can be directly related to the dilepton production in the quark gluon plasma phase.

Finally, the relation of the vector spectral function to properties of electromagnetic probes has been used to compute also the thermal photon rate. There, spectral functions for $p \neq 0$ have been calculated and an almost vanishing spectral function at the photon point ($\omega = |\mathbf{p}|$) also leads to a vanishing or rather small photon rate in the quark gluon plasma phase. As the statistical errors are still quite large, an upper bound has been presented which still is in conflict with perturbative calculations. However, also the latter are rather difficult at these temperatures. Once these problems are solved, the rate below T_c could be calculated which is important for background contributions to the photon rate.

Ideally, all the investigations presented here should be performed including the full dynamics, i.e., including light dynamical quarks in the lattice simulation, as their contributions are expected to be relevant for the calculated electromagnetic rates. As large N_τ values, used within this work, are necessary for the application of the maximum entropy method, this may not become possible for quite some time.

Appendix A

Conventions & Tables

A.1 Dirac Matrices

The Euclidian γ matrices in the non-relativistic representation are selfadjoint ($\gamma_\mu = \gamma_\mu^\dagger$) and obey the anti-commutation relation $\{\gamma_\mu, \gamma_\nu\} = 2\,\mathbb{1}_{\mu\nu}$,

$$\gamma_1 = \begin{pmatrix} 0 & 0 & 0 & i \\ 0 & 0 & i & 0 \\ 0 & -i & 0 & 0 \\ -i & 0 & 0 & 0 \end{pmatrix} \quad \gamma_2 = \begin{pmatrix} 0 & 0 & 0 & 1 \\ 0 & 0 & -1 & 0 \\ 0 & -1 & 0 & 0 \\ 1 & 0 & 0 & 0 \end{pmatrix} \quad \gamma_3 = \begin{pmatrix} 0 & 0 & i & 0 \\ 0 & 0 & 0 & -i \\ -i & 0 & 0 & 0 \\ 0 & i & 0 & 0 \end{pmatrix}$$

$$\gamma_4 = \begin{pmatrix} 1 & 0 & 0 & 0 \\ 0 & 1 & 0 & 0 \\ 0 & 0 & -1 & 0 \\ 0 & 0 & 0 & -1 \end{pmatrix} \quad \gamma_5 = \begin{pmatrix} 0 & 0 & 1 & 0 \\ 0 & 0 & 0 & 1 \\ 1 & 0 & 0 & 0 \\ 0 & 1 & 0 & 0 \end{pmatrix} \quad = \quad \gamma_1\gamma_2\gamma_3\gamma_4$$

They can be converted to the Bjorken and Drell conventions by $\gamma_i = i\gamma^i_{BD}, \gamma_4 = \gamma^0_{BD}$ and $\gamma_5 = \gamma^5_{BD}$.

A.2 Renormalization Group Factors

κ_c	am_q	Z	κ_c	am_q	Z	κ_c	am_q	Z	H
$\beta = 6.000$			$\beta = 6.136$			$\beta = 6.499$			
0.1324	0.081(3)	0.79	0.1330	0.07715(1)	0.81	0.1330	0.0761(2)	0.83	S
		0.70			0.74			0.78	P
		0.86			0.87			0.89	V
		0.871			0.873			0.889	V
		0.90			0.90			0.91	A
0.1332	0.058(3)	0.77	0.1340	0.0494(1)	0.78	0.1340	0.0476(2)	0.80	S
		0.70			0.72			0.75	P
		0.84			0.84			0.86	V
		0.845			0.841			0.859	V
		0.87			0.87			0.88	A
0.1342	0.058(3)	0.74	0.1346	0.0326(1)	0.76	0.1346	0.0302(2)	0.78	S
		0.67			0.70			0.73	P
		0.81			0.83			0.84	V
		0.813			0.822			0.841	V
		0.84			0.85			0.87	A
0.1348	0.058(3)	0.72	0.1349	0.0226(1)	0.75	0.13531	0.0094(3)	0.76	S
		0.66			0.70			0.72	P
		0.79			0.82			0.82	V
		0.794			0.812			0.819	V
		0.82			0.84			0.84	A
			0.1354	0.0097(3)	0.74	0.1354	0.0066(3)	0.76	S
					0.68			0.71	P
					0.80			0.82	V
					0.79			0.817	V
					0.83			0.84	A

Table A.1: Current renormalization factors below T_c as obtained from Eq.(4.8) and Eq.(4.10).

β	S	P	V	V	A	A
6.499	0.75	0.71	0.81	0.811	0.84	0.828
6.640	0.77	0.72	0.82	0.818	0.84	0.836
6.872	0.78	0.74	0.83	0.829	0.85	0.847
7.192	0.80	0.76	0.84	0.842	0.86	0.859
7.457	0.81	0.78	0.85	0.851	0.87	0.868

Table A.2: Current renormalization factors above T_c.

A.3 Meson Masses

A.3.1 Screening Masses

β	κ	N_σ	$m_P a$	$m_V a$	$m_S a$
6.000	0.13240	24	0.534(5)	0.637(6)	0.733(52)
	0.13320	24	0.458(5)	0.576(7)	0.633(81)
	0.13420	24	0.342(6)	0.495(14)	0.545(167)
	0.13480	24	0.254(8)	0.453(31)	0.808(101)
6.136	0.13300	32	0.460(3)	0.540(5)	0.683(43)
		24	0.488(3)	0.572(7)	0.716(27)
	0.13400	32	0.360(3)	0.469(5)	0.590(84)
		24	0.398(5)	0.506(11)	0.622(35)
	0.13460	32	0.289(3)	0.424(4)	0.505(101)
		24	0.337(6)	0.464(10)	0.579(47)
	0.13495	32	0.241(4)	0.399(10)	0.686(33)
	0.13540	32	0.158(10)	0.405(23)	1.004(247)
		24	0.237(9)	0.424(21)	0.695(107)
6.499	0.13300	48	0.361(4)	0.402(3)	0.493(17)
		32	0.381(4)	0.421(4)	0.500(19)
		24	0.412(7)	0.452(7)	0.543(18)
	0.13400	32	0.294(5)	0.344(5)	0.424(28)
		24	0.326(8)	0.378(6)	0.438(16)
	0.13460	48	0.219(8)	0.280(9)	0.323(73)
		32	0.234(7)	0.300(5)	0.410(46)
		24	0.273(8)	0.339(9)	0.385(16)
	0.13531	32	0.158(11)	0.259(16)	0.483(70)
	0.13540	32	0.146(10)	0.251(27)	0.128(56)
		24	0.177(17)	0.284(15)	0.353(121)

Table A.3: Screening masses as obtained from the two exponential fit.

T/T_c	N_τ	N_σ	$m_P a$	$m_V a$	$m_S a$	$m_A a$
6.0	32	8	0.775(5)	0.779(5)	0.776(4)	0.803(5)
3.0	64	16	0.381(6)	0.398(8)	0.381(5)	0.399(9)
	48	12	0.516(3)	0.537(3)	0.517(2)	0.535(5)
	32	16	0.397(3)	0.431(3)	0.397(3)	0.425(5)
	32	8	0.751(6)	0.783(9)	0.753(7)	0.779(11)
1.5	64	24	0.245(4)	0.267(4)	0.244(4)	0.269(4)
	64	16	0.356(9)	0.386(6)	0.357(5)	0.378(11)
	48	12	0.484(6)	0.509(6)	0.484(6)	0.510(10)
1.25	48	12	0.449(10)	0.495(9)	0.473(14)	0.485(8)

Table A.4: Screening masses above T_c for different lattice sizes.

A.3.2 MEM masses

β	κ	N_σ	$m_P a$	$m_V a$	$m_S a$
6.499	0.13300	32	0.431(2)	0.487(1)	0.542(15)
		24	0.438(5)	0.509(11)	0.564(14)
	0.13400	32	0.338(2)	0.427(1)	0.457(15)
		24	0.346(6)	0.435(3)	0.464(11)
	0.13460	32	0.260(2)	0.361(1)	0.416(16)
		24	0.283(8)	0.387(3)	0.394(14)
	0.13531	32	0.224(1)	0.357(1)	0.645(38)
6.136	0.13300	32	0.464(3)	0.561(5)	0.723(11)
		24	0.494(3)	0.572(8)	0.716(29)
	0.13400	32	0.357(2)	0.494(6)	0.668(12)
		24	0.398(3)	0.498(14)	0.653(35)
	0.13460	32	0.272(3)	0.453(3)	0.646(11)
		24	0.327(6)	0.453(8)	0.631(38)
	0.13495	32	0.246(58)	0.431(3)	0.649(15)
6.000	0.13240	24	0.516(10)	0.657(5)	0.697(61)
	0.13320	24	0.442(16)	0.601(2)	0.612(125)
	0.13420	24	0.331(15)	0.527(3)	–
	0.13480	24	0.250(14)	0.475(4)	–

Table A.5: Pole masses as obtained from the SPF.

Appendix B

Auxiliary Functions for the Free Lattice Field Theory

In this appendix, various definitions and functions, needed in Chapter 3, are listed in order of their appearance.

The first ones are sum rules for the introducing a finite N_τ for the quark propagator, Eq.(3.42). With $f(n) = (-1)^{|n|} e^{-E|t+N_\tau n|}$, it is easily shown that the following equations hold

$$\begin{aligned}
\sum_{n=-\infty}^{\infty} f(n) &= \frac{\sinh(2EN_\tau(t/N_\tau - 0.5))}{\cosh(EN_\tau/2)} \;, \\
\sum_{n=-\infty}^{\infty} \mathrm{sgn}(t+N_\tau n) f(n) &= \frac{\cosh(2EN_\tau(t/N_\tau - 0.5))}{\cosh(EN_\tau/2)} \;, \\
\sum_{n=-\infty}^{\infty} (-1)^{|t+N_\tau n|} f(n) &= (-1)^t \frac{\sinh(2EN_\tau(t/N_\tau - 0.5))}{\cosh(EN_\tau/2)} \;, \\
\sum_{n=-\infty}^{\infty} (-1)^{|t+N_\tau n|} \mathrm{sgn}(t+N_\tau n) f(n) &= (-1)^t \frac{\cosh(2EN_\tau(t/N_\tau - 0.5))}{\cosh(EN_\tau/2)} \;.
\end{aligned} \tag{B.1}$$

Note that the last two equations are true only for even N_τ.

Definitions for the Wilson action

In the derivation of the Wilson spectral function in Section 3.1.3, the three functions A, B, C_i are used to define the integral over the two remaining degrees of freedom from the three momentum integral of Eq.(3.33). They are defined as

$$\begin{aligned}
A(\mathbf{z}) &= \xi \, \frac{\xi + 2z(x + z_2 + z_3) + m_q}{1 + 2z(z_2 + z_3) + m_q - 2\xi z} \;, && \text{(B.2)}\\
B(\mathbf{z}) &= \left(1 + 2\xi^{-1} z(x + z_2 + z_3) + \xi^{-1} m_q\right)^{-2} \;, && \text{(B.3)}\\
C_1(\mathbf{z}) &= \left(x \; z_2 \; z_3 \; (1 - zx) \; (1 - zz_2) \; (1 - zz_3)\right)^{-1/2} \;, && \text{(B.4)}\\
C_2(\mathbf{z}) &= \frac{4}{\xi^2} \frac{x(1 - zx) + z_2(1 - zz_2) + z_3(1 - zz_3)}{\left(x \; z_2 \; z_3 \; (1 - zx) \; (1 - zz_2) \; (1 - zz_3)\right)^{1/2}} \;. && \text{(B.5)}
\end{aligned}$$

Definitions for the FP-Action

The following functions are needed for the fermion FP-propagator, Eq.(3.43). With the shorthand notation $\hat{c}_i = \cos k_i$ and $\hat{s}_i = \sin k_i$ they are

$$\alpha_1(\mathbf{k}) = 2\hat{s}_1(\rho_1 + 2\rho_2(\hat{c}_2 + \hat{c}_3) + 4\rho_3\hat{c}_2\hat{c}_3) \;, \tag{B.6}$$
$$\alpha_2(\mathbf{k}) = 2\hat{s}_2(\rho_1 + 2\rho_2(\hat{c}_1 + \hat{c}_3) + 4\rho_3\hat{c}_1\hat{c}_3) \;, \tag{B.7}$$
$$\alpha_3(\mathbf{k}) = 2\hat{s}_3(\rho_1 + 2\rho_2(\hat{c}_1 + \hat{c}_2) + 4\rho_3\hat{c}_1\hat{c}_2) \;, \tag{B.8}$$

$$\beta_1(\mathbf{k}) = 4\hat{s}_1(\rho_2 + 2\rho_3(\hat{c}_2 + \hat{c}_3) + 4\rho_4\hat{c}_2\hat{c}_3) \;, \tag{B.9}$$
$$\beta_2(\mathbf{k}) = 4\hat{s}_2(\rho_2 + 2\rho_3(\hat{c}_1 + \hat{c}_3) + 4\rho_4\hat{c}_1\hat{c}_3) \;, \tag{B.10}$$
$$\beta_3(\mathbf{k}) = 4\hat{s}_3(\rho_2 + 2\rho_3(\hat{c}_1 + \hat{c}_2) + 4\rho_4\hat{c}_1\hat{c}_2) \;, \tag{B.11}$$

$$\delta(\mathbf{k}) = 2\rho_1 + 4\rho_2(\hat{c}_1 + \hat{c}_2 + \hat{c}_3) + 8\rho_3(\hat{c}_1\hat{c}_2 + \hat{c}_2\hat{c}_3 + \hat{c}_1\hat{c}_3) + 16\rho_4\hat{c}_1\hat{c}_2\hat{c}_3 \;, \tag{B.12}$$

and

$$\kappa_1(\mathbf{k}) = \lambda_0 + 2\lambda_1(\hat{c}_1 + \hat{c}_2 + \hat{c}_3) + 4\lambda_2(\hat{c}_1\hat{c}_2 + \hat{c}_2\hat{c}_3 + \hat{c}_1\hat{c}_3) + 8\lambda_3\hat{c}_1\hat{c}_2\hat{c}_3 \;, \tag{B.13}$$
$$\kappa_2(\mathbf{k}) = 2\lambda_1 + 4\lambda_2(\hat{c}_1 + \hat{c}_2 + \hat{c}_3) + 8\lambda_3(\hat{c}_1\hat{c}_2 + \hat{c}_2\hat{c}_3 + \hat{c}_1\hat{c}_3) + 16\lambda_4\hat{c}_1\hat{c}_2\hat{c}_3 \;. \tag{B.14}$$

With the relation

$$2\rho_1 + 12\rho_2 + 24\rho_3 + 16\rho_4 = 1 \;, \tag{B.15}$$
$$\lambda_0 + 6\lambda_1 + 12\lambda_2 + 8\lambda_3 = 1 \;, \tag{B.16}$$
$$2\lambda_1 + 12\lambda_2 + 24\lambda_3 + 16\lambda_4 = -1 \;, \tag{B.17}$$

valid for $m_q = 0$, it is easy to show that d^{FP} and δ^2, Eq.(3.50), reach one in the continuum limit.

In Chapter 3, only the contribution of the first pole to the meson correlation function is discussed. The contribution from the second pole, appearing in Eq.(3.48), can be divided into two parts

$$\Delta G_H^{E_2}(\tau) = G_{H2}(\tau) + G_{H12}(\tau) \tag{B.18}$$

H	$g_H^{FP_{12}}$	H	$g_H^{FP_{12}}$
P	$d_1^{FP_{12}} + d_2^{FP_{12}}$	S	$-d_1^{FP_{12}} + d_2^{FP_{12}}$
V_0	$d_1^{FP_{12}} + d_2^{FP_{12}}$	A_0	$d_1^{FP_{12}} - d_2^{p3}$
$\sum_{i=1}^3 V_i$	$d_1^{FP_{12}} + 3d_2^{FP_{12}}$	$\sum_{i=1}^3 A_i$	$d_1^{FP_{12}} - 3d_2^{p3}$
$\sum_{\mu=0}^3 V_\mu$	$2d_1^{p3} + 4d_2^{FP_{12}}$	$\sum_{\mu=0}^3 A_\mu$	$2d_1^{FP_{12}} - 4d_2^{FP_{12}}$

Table B.1: The explicit form of the functions $g_H^{FP_{12}}$ appearing in Eq.(B.20). The functions $d_1^{FP_{12}}(\mathbf{k})$ and $d_2^{FP_{12}}(\mathbf{k})$ are defined in Eqs.(B.22) and (B.23).

with

$$\begin{aligned}
G_{H2}(\tau) &= N_c\left(\frac{N_\tau}{N_\sigma}\right)^3\sum_{\mathbf{k}}\frac{c_H^{FP2}(\mathbf{k})\cosh[2E_2(\mathbf{k})N_\tau(\tau-1/2)]+d_H^{FP2}(\mathbf{k})}{(P^2-QR)\cosh^2(E_2(\mathbf{k})N_\tau/2)}\ , && \text{(B.19)}\\
G_{H12}(\tilde\tau) &= N_c\left(\frac{N_\tau}{N_\sigma}\right)^3\sum_{\mathbf{k}}\frac{(-1)^{\theta(-Q)\tau+1}}{(P^2-QR)\cosh(E_1(\mathbf{k})N_\tau/2)\cosh(E_2(\mathbf{k})N_\tau/2)} && \text{(B.20)}\\
&\quad\Big[g_H^{FP12}(\mathbf{k})\big\{\cosh[E_s(\mathbf{k})N_\tau(\tilde\tau-1/2)]-\cosh[E_d(\mathbf{k})N_\tau(\tilde\tau-1/2)]\big\}\\
&\quad+\ \delta^2(\mathbf{k})\big\{\cosh[E_s(\mathbf{k})N_\tau(\tilde\tau-1/2)]+\cosh[E_d(\mathbf{k})N_\tau(\tilde\tau-1/2)]\big\}\Big]\ .
\end{aligned}$$

Here the second term represents a mixed contribution from both poles with the energies $E_s = E_1 + E_2$ and $E_d = E_1 - E_2$. The functions c_H^{FP2} and d_H^{FP2} are exactly defined as $c_H^{FP}$and d_H^{FP}, if one replaces

$$d^{FP2} \equiv d^{FP2}(\mathbf{k}) = \frac{(\mathcal{K}_1 + \mathcal{K}_2\,\mathrm{sgn}(Q)\cosh E_2)^2}{\sinh^2 E_2}\ . \tag{B.21}$$

g_H^{FP12} is defined in Table B.1 with

$$\begin{aligned}
d_1^{FP12} &= \frac{\mathcal{K}_1^2\,\mathrm{sgn}(Q)+\mathcal{K}_2^2\cosh E_1\cosh E_2+\mathcal{K}_1\mathcal{K}_2(\cosh E_2+\mathrm{sgn}(Q)\cosh E_1)}{\sinh E_1\sinh E_2}\ , && \text{(B.22)}\\
d_2^{FP12} &= \frac{\kappa_1^2\,\mathrm{sgn}(Q)+\kappa_2^2\cosh E_1\cosh E_2+\kappa_1\kappa_2(\cosh E_2+\mathrm{sgn}(Q)\cosh E_1)}{\sinh E_1\sinh E_2}\ . && \text{(B.23)}
\end{aligned}$$

Now only the auxiliary function F appearing in Eq.(3.55) remains to be defined

$$F(\omega,x_2,x_3) = \frac{dx_1}{dy}\frac{1}{\prod\limits_i\sqrt{1-x_i^2}}\frac{1}{QR-P^2}\ . \tag{B.24}$$

To obtain an analytical expression for $x_1(y)$ rewrite the functions

$$\begin{aligned}
P(\mathbf{x}) &= P_1(x_2,x_3)\ +\ x_1P_2(x_2,x_3)+x_1^2P_3(x_2,x_3)\ , && \text{(B.25)}\\
Q(\mathbf{x}) &= Q_1(x_2,x_3)\ +\ x_1Q_2(x_2,x_3)+x_1^2Q_3(x_2,x_3)\ , && \text{(B.26)}\\
R(\mathbf{x}) &= R_1(x_2,x_3)\ +\ x_1R_2(x_2,x_3)+x_1^2R_3(x_2,x_3)\ , && \text{(B.27)}
\end{aligned}$$

and define

$$N_i(y, x_2, x_3) \;=\; R_i(x_2, x_3) \,+\, 2yP_i(x_2, x_3) \,+\, y^2 Q_i(x_2, x_3) \;\;,\; i = \;1,\; 2,\; 3\;. \tag{B.28}$$

This leads finally to the definition of

$$x_1(y, x_2, x_3) \;=\; -\frac{N_2 - \sqrt{N_2^2 - 4N_1N_2}}{2N_3} \tag{B.29}$$

and gives the necessary inversion of the dispersion relation. This in addition allows one to write down the boundary of the integration as

$$\Omega^{FP}(y) = \left\{ [1, \cosh E_1^{max}] \cap \{-2N_3 \geq N_2 + \sqrt{N_2^2 - 4N_3N_1} \geq 2N_3\} \right\} \;. \tag{B.30}$$

Bibliography

[1] U. W. Heinz and M. Jacob, “Evidence for a new state of matter: An assessment of the results from the CERN lead beam programme,” `nucl-th/0002042`.

[2] H. Satz, “Limits of confinement: The first 15 years of ultra- relativistic heavy ion studies,” *Nucl. Phys.* **A715** (2003) 3–19, `hep-ph/0209181`.

[3] K. J. Eskola, “High energy nuclear collisions,” `hep-ph/9911350`.

[4] R. Rapp and J. Wambach, “Chiral Symmetry Restoration and Dileptons in Relativistic Heavy-Ion Collisions,” *Adv. Nucl. Phys.* **25** (2000) 1, `hep-ph/9909229`.

[5] F. Karsch *et al.*, “Where is the chiral critical point in 3-flavor QCD?,” `hep-lat/0309116`.

[6] **CERES** Collaboration, G. Agakishiev *et al.*, “Enhanced production of low mass electron pairs in 200-GeV/u S - Au collisions at the CERN SPS,” *Phys. Rev. Lett.* **75** (1995) 1272–1275.

[7] L. D. McLerran and T. Toimela, “Photon and Dilepton Emission from the Quark - Gluon Plasma: some general Considerations,” *Phys. Rev.* **D31** (1985) 545.

[8] E. V. Shuryak, “Quark - gluon plasma and hadronic production of leptons, photons and psions,” *Phys. Lett.* **B78** (1978) 150.

[9] **CERES/NA45** Collaboration, G. Agakishiev *et al.*, “Low-mass e+ e- pair production in 158-A-GeV Pb Au collisions at the CERN SPS, its dependence on multiplicity and transverse momentum,” *Phys. Lett.* **B422** (1998) 405–412, `nucl-ex/9712008`.

[10] **HELIOS/3** Collaboration, A. L. S. Angelis *et al.*, “Excess of continuum dimuon production at masses between threshold and the J/psi in S W interactions at 200-GeV/c/nucleon,” *Eur. Phys. J.* **C13** (2000) 433–452.

[11] **NA38** Collaboration, M. C. Abreu *et al.*, “Dimuon and charm production in nucleus nucleus collisions at the CERN-SPS,” *Eur. Phys. J.* **C14** (2000) 443–455.

[12] M. Asakawa, T. Hatsuda, and Y. Nakahara, “Maximum Entropy Analysis of the Spectral Functions in Lattice QCD,” *Prog. Part. Nucl. Phys.* **46** (2001) 459–508, `hep-lat/0011040`.

[13] **Particle Data Group** Collaboration, K. Hagiwara *et al.*, "Review of Particle Physics," *Phys. Rev.* **D66** (2002) 010001.

[14] R. E. Marshak, "Conceptual Foundations of Modern Particle Physics,". Singapore, Singapore: World Scientific (1993) 673 p.

[15] M. Gell-Mann, R. J. Oakes, and B. Renner, "Behavior of current divergences under SU(3) x SU(3)," *Phys. Rev.* **175** (1968) 2195–2199.

[16] E. Witten, "Current algebra theorems for the U(1) 'Goldstone Boson'," *Nucl. Phys.* **B156** (1979) 269.

[17] G. Veneziano, "U(1) without Instantons," *Nucl. Phys.* **B159** (1979) 213–224.

[18] E. V. Shuryak, "Two scales and phase transitions in quantum chromodynamics," *Phys. Lett.* **B107** (1981) 103.

[19] A. Peikert, "QCD thermodynamics with 2+1 quark flavours in lattice simulations,". PhD thesis, Bielefeld (2000).

[20] R. D. Pisarski and F. Wilczek, "Remarks on the chiral phase transition in chromodynamics," *Phys. Rev.* **D29** (1984) 338–341.

[21] G. Boyd *et al.*, "Thermodynamics of SU(3) Lattice Gauge Theory," *Nucl. Phys.* **B469** (1996) 419–444, `hep-lat/9602007`.

[22] F. Karsch, C. Schmidt, and S. Stickan, "Common features of deconfining and chiral critical points in QCD and the three state Potts model in an external field," *Comput. Phys. Commun.* **147** (2002) 451–454, `hep-lat/0111059`.

[23] F. Karsch, E. Laermann, and A. Peikert, "Quark mass and flavor dependence of the QCD phase transition," *Nucl. Phys.* **B605** (2001) 579–599, `hep-lat/0012023`.

[24] F. Karsch and E. Laermann, "Susceptibilities, the Specific Heat and a Cumulant in Two Flavor QCD," *Phys. Rev.* **D50** (1994) 6954–6962, `hep-lat/9406008`.

[25] F. Karsch, E. Laermann, A. Peikert, C. Schmidt, and S. Stickan, "Flavor and Quark Mass Dependence of QCD Thermodynamics," *Nucl. Phys. Proc. Suppl.* **94** (2001) 411–414, `hep-lat/0010040`.

[26] C. Schmidt, *The Phase Diagram and Equation of State of Improved Lattice QCD for High Temperatures and small Chemical Potential.* PhD thesis, Univesity of Bielefeld, 2003.

[27] E. Laermann, "Chiral transition in 2 flavor staggered QCD," *Nucl. Phys. Proc. Suppl.* **60A** (1998) 180–187.

[28] R. V. Gavai, S. Gupta, and R. Lacaze, "Quenched QCD at finite temperature with chiral Fermions," *Phys. Rev.* **D65** (2002) 094504, `hep-lat/0107022`.

[29] P. Vranas, "Dynamical lattice QCD thermodynamics and the $U(1)_A$ symmetry with domain wall fermions," `hep-lat/9903024`.

[30] I. Montvay and G. Munster, "Quantum Fields on a Lattice,". Cambridge, UK: Univ. Pr. (1994) 491 p. (Cambridge monographs on mathematical physics).

[31] R. Gupta, "Introduction to lattice QCD," `hep-lat/9807028`.

[32] F. Karsch, "Lattice QCD at High Temperature and Density," *Lect. Notes Phys.* **583** (2002) 209–249, `hep-lat/0106019`.

[33] K. G. Wilson, "Confinement of quarks," *Phys. Rev.* **D10** (1974) 2445–2459.

[34] **CP-PACS** Collaboration, S. Aoki *et al.*, "Quenched Light Hadron Spectrum," *Phys. Rev. Lett.* **84** (2000) 238–241, `hep-lat/9904012`.

[35] K. Symanzik, "Mathematical Problems in Theoretical Physics," *Lecture notes in Physics.* Springer-Verlag, Berlin (1982) 153.

[36] B. Sheikholeslami and R. Wohlert, "Improved continuum limit lattice action for QCD with Wilson fermions," *Nucl. Phys.* **B259** (1985) 572.

[37] H. B. Nielsen and M. Ninomiya, "No go theorem for regularizing chiral fermions," *Phys. Lett.* **B105** (1981) 219.

[38] J. B. Kogut and L. Susskind, "Hamiltonian formulation of Wilson's lattice gauge theories," *Phys. Rev.* **D11** (1975) 395.

[39] M. Bochicchio, L. Maiani, G. Martinelli, G. C. Rossi, and M. Testa, "Chiral symmetry on the lattice with Wilson fermions," *Nucl. Phys.* **B262** (1985) 331.

[40] M. Lüscher, S. Sint, R. Sommer, P. Weisz, and U. Wolff, "Non-perturbative O(a) improvement of lattice QCD," *Nucl. Phys.* **B491** (1997) 323–343, `hep-lat/9609035`.

[41] M. Guagnelli and R. Sommer, "Non-perturbative O(a) improvement of the vector current," *Nucl. Phys. Proc. Suppl.* **63** (1998) 886–888, `hep-lat/9709088`.

[42] M. G. Alford, T. R. Klassen, and G. P. Lepage, "Improving lattice quark actions," *Nucl. Phys.* **B496** (1997) 377–407, `hep-lat/9611010`.

[43] W. Bietenholz and U. J. Wiese, "Perfect Lattice Actions for Quarks and Gluons," *Nucl. Phys.* **B464** (1996) 319–352, `hep-lat/9510026`.

[44] P. Hasenfratz and F. Niedermayer, "Perfect lattice action for asymptotically free theories," *Nucl. Phys.* **B414** (1994) 785–814, `hep-lat/9308004`.

[45] C. Gattringer, "A new approach to Ginsparg-Wilson fermions," *Phys. Rev.* **D63** (2001) 114501, `hep-lat/0003005`.

[46] R. Narayanan and H. Neuberger, "A construction of lattice chiral gauge theories," *Nucl. Phys.* **B443** (1995) 305–385, `hep-th/9411108`.

[47] D. B. Kaplan, "A Method for Simulating Chiral Fermions on the Lattice," *Phys. Lett.* **B288** (1992) 342–347, `hep-lat/9206013`.

[48] P. H. Ginsparg and K. G. Wilson, “A remnant of chiral symmetry on the lattice,” *Phys. Rev.* **D25** (1982) 2649.

[49] E. V. Shuryak, “Correlation functions in the QCD vacuum,” *Rev. Mod. Phys.* **65** (1993) 1–46.

[50] M. C. Chu, J. M. Grandy, S. Huang, and J. W. Negele, “Correlation functions of hadron currents in the QCD vacuum calculated in lattice QCD,” *Phys. Rev.* **D48** (1993) 3340–3353, `hep-lat/9306002`.

[51] I. Wetzorke, *Lattice QCD Calculations of Hadron Spectra and Spectral Functions in the Vacuum and in a Thermal Heat Bath.* PhD thesis, Univesity of Bielefeld, 2001.

[52] **QCD-TARO** Collaboration, P. de Forcrand *et al.*, “Meson correlators in finite temperature lattice QCD,” *Phys. Rev.* **D63** (2001) 054501, `hep-lat/0008005`.

[53] **LHP** Collaboration, R. G. Edwards, U. M. Heller, and D. G. Richards, “Spectroscopy using the Anisotropic Clover Action,” `hep-lat/0303004`.

[54] T. Umeda, K. Nomura, and H. Matsufuru, “Charmonium at finite temperature in quenched lattice QCD,” `hep-lat/0211003`.

[55] S. Stickan, “In medium hadron properties,” `hep-lat/0301009`.

[56] R. Gupta, D. Daniel, and J. Grandy, “Bethe-Salpeter amplitudes and density correlations for mesons with Wilson fermions,” *Phys. Rev.* **D48** (1993) 3330–3339, `hep-lat/9304009`.

[57] **UKQCD** Collaboration, P. Lacock, A. McKerrell, C. Michael, I. M. Stopher, and P. W. Stephenson, “Efficient Hadronic Operators in Lattice Gauge Theory,” *Phys. Rev.* **D51** (1995) 6403–6410, `hep-lat/9412079`.

[58] **Ape** Collaboration, M. Albanese *et al.*, “Glueball masses and the loop loop correlation functions,” *Phys. Lett.* **B197** (1987) 400.

[59] T. Hashimoto, A. Nakamura, and I. O. Stamatescu, “Temperature dependent structure in the mesonic channels of QCD,” *Nucl. Phys.* **B400** (1993) 267–308.

[60] W. Florkowski and B. L. Friman, “Spatial dependence of meson correlation functions at high temperature,” *Z. Phys.* **A347** (1994) 271–276.

[61] N. Cabibbo and E. Marinari, “A new method for updating SU(N) matrices in computer simulations of gauge theories,” *Phys. Lett.* **B119** (1982) 387.

[62] A. D. Kennedy and B. J. Pendleton, “Improved heat bath method for Monte Carlo calculations in lattice gauge theories,” *Phys. Lett.* **B156** (1985) 393.

[63] S. L. Adler, “Overrrelaxation method for the Monte Carlo evaluation of the partition function for multiquadratic actions,” *Phys. Rev.* **D23** (1981) 2901.

[64] M. Creutz, “Overrelaxation and Monte Carlo Simulation,” *Phys. Rev.* **D36** (1987) 515.

[65] M. R. Hestenes and E. Stiefel,, "Conjugate Gradient," *J. Res. Nat. Bur. Standards* **49** (1952) 409.

[66] H. van der Vorst,, "A Fast and Smoothly Converging Variant of Bi-CG for the Solution of Nonsymmetric Linear Systems," *SIAM J. Sc. Stat. Comp.* **13** (1992) 631.

[67] A. Frommer, V. Hannemann, B. Nockel, T. Lippert, and K. Schilling, "Accelerating Wilson Fermion Matrix Inversions by Means of the Stabilized Biconjugate Gradient Agorithm," *Int. J. Mod. Phys.* **C5** (1994) 1073–1088, `hep-lat/9404013`.

[68] T. A. DeGrand and P. Rossi, "Conditioning techniques for dynamical fermions," *Comput. Phys. Commun.* **60** (1990) 211.

[69] N. Stanford. PhD thesis, Univesity of Edinburgh, 1994.

[70] C. Michael and A. McKerrell, "Fitting Correlated Hadron Mass Spectrum Data," *Phys. Rev.* **D51** (1995) 3745–3750, `hep-lat/9412087`.

[71] F. Karsch, E. Laermann, P. Petreczky, and S. Stickan, "Infinite temperature limit of meson spectral functions calculated on the lattice," *Phys. Rev.* **D68** (2003) 014504, `hep-lat/0303017`.

[72] I. Wetzorke, F. Karsch, E. Laermann, P. Petreczky, and S. Stickan, "Meson Spectral Functions at finite Temperature," *Nucl. Phys. Proc. Suppl.* **106** (2002) 510–512, `hep-lat/0110132`.

[73] W. Bietenholz, R. Brower, S. Chandrasekharan, and U. J. Wiese, "Progress on Perfect Lattice Actions for QCD," *Nucl. Phys. Proc. Suppl.* **53** (1997) 921–934, `hep-lat/9608068`.

[74] F. Karsch, M. G. Mustafa, and M. H. Thoma, "Finite Temperature Meson Correlation Functions in HTL Approximation," *Phys. Lett.* **B497** (2001) 249–258, `hep-ph/0007093`.

[75] D. B. Carpenter and C. F. Baillie, "Free fermion propagators and lattice finite size effects," *Nucl. Phys.* **B260** (1985) 103.

[76] J. Engels, F. Karsch, and H. Satz, "The high temperature behavior of lattice QCD with fermions," *Phys. Lett.* **B113** (1982) 398.

[77] K. G. Wilson, "The renormalization group: critical phenomena and the kondo problem," *Rev. Mod. Phys.* **47** (1975) 773.

[78] K. Orginos, W. Bietenholz, R. Brower, S. Chandrasekharan, and U. J. Wiese, "The Perfect Quark-Gluon Vertex Function," *Nucl. Phys. Proc. Suppl.* **63** (1998) 904–906, `hep-lat/9709100`.

[79] T. Matsui and H. Satz, "J / ψ suppresion by quark - gluon plasma formation," *Phys. Lett.* **B178** (1986) 416.

[80] **CP-PACS** Collaboration, M. Okamoto *et al.*, “Charmonium Spectrum from Quenched Anisotropic Lattice QCD,” *Phys. Rev.* **D65** (2002) 094508, `hep-lat/0112020`.

[81] T. R. Klassen, “Non-Perturbative Improvement of the Anisotropic Wilson QCD Action,” *Nucl. Phys. Proc. Suppl.* **73** (1999) 918–920, `hep-lat/9809174`.

[82] M. Asakawa, T. Hatsuda, and Y. Nakahara, “Hadronic Spectral Functions above the QCD Phase Transition,” `hep-lat/0208059`.

[83] R. G. Edwards, U. M. Heller, and T. R. Klassen, “Accurate Scale Determinations for the Wilson Gauge Action,” *Nucl. Phys.* **B517** (1998) 377–392, `hep-lat/9711003`.

[84] B. Beinlich, F. Karsch, E. Laermann, and A. Peikert, “String Tension and Thermodynamics with Tree Level and Tadpole Improved Actions,” *Eur. Phys. J.* **C6** (1999) 133–140, `hep-lat/9707023`.

[85] G. P. Lepage and P. B. Mackenzie, “On the Viability of Lattice Perturbation Theory,” *Phys. Rev.* **D48** (1993) 2250–2264, `hep-lat/9209022`.

[86] S. Sint and P. Weisz, “Further results on O(a) improved lattice QCD to one-loop order of perturbation theory,” *Nucl. Phys.* **B502** (1997) 251–268, `hep-lat/9704001`.

[87] M. Göckeler *et al.*, “Perturbative renormalisation of bilinear quark and gluon operators,” *Nucl. Phys. Proc. Suppl.* **53** (1997) 896–898, `hep-lat/9608033`.

[88] G. Parisi, “Recent progresses in gauge theories,”. Presented at 20th Int. Conf. on High Energy Physics, Madison, Wis., Jul 17-23, 1980.

[89] T. R. Klassen, “The (Lattice) QCD potential and coupling: How to accurately interpolate between multiloop QCD and the string picture,” *Phys. Rev.* **D51** (1995) 5130–5152.

[90] M. Luscher, S. Sint, R. Sommer, and H. Wittig, “Non-perturbative determination of the axial current normalization constant in O(a) improved lattice QCD,” *Nucl. Phys.* **B491** (1997) 344–364, `hep-lat/9611015`.

[91] G. M. de Divitiis and R. Petronzio, “Non-perturbative renormalization constants on the lattice from flavour non-singlet Ward identities,” *Phys. Lett.* **B419** (1998) 311–316, `hep-lat/9710071`.

[92] **ALPHA** Collaboration, M. Guagnelli *et al.*, “Non-perturbative results for the coefficients b(m) and b(A)-b(P) in O(a) improved lattice QCD,” *Nucl. Phys.* **B595** (2001) 44–62, `hep-lat/0009021`.

[93] **ALPHA** Collaboration, S. Capitani, M. Luscher, R. Sommer, and H. Wittig, “Non-perturbative quark mass renormalization in quenched lattice QCD,” *Nucl. Phys.* **B544** (1999) 669–698, `hep-lat/9810063`.

[94] Y. Nakahara, M. Asakawa, and T. Hatsuda, “Hadronic Spectral Functions in Lattice QCD,” *Phys. Rev.* **D60** (1999) 091503, `hep-lat/9905034`.

[95] **CP-PACS** Collaboration, T. Yamazaki *et al.*, “Spectral function and excited states in lattice QCD with maximum entropy method,” *Phys. Rev.* **D65** (2002) 014501, `hep-lat/0105030`.

[96] M. Jarrell and J. E. Gubernatis, “Maximum Entropy Analytic Continuation of Quatum Monte Carlo Data,” *Phys. Rep.* **269** (1996) 133.

[97] H. Jeffreys, “Theory of Probability,”. Oxford Univ. Press., Oxford 1998.

[98] K. Langfeld, H. Reinhardt, and J. Gattnar, “Gluon propagators and quark confinement,” *Nucl. Phys.* **B621** (2002) 131–156, `hep-ph/0107141`.

[99] E. Laermann and P. Schmidt, “Meson Screening Masses at high Temperature in quenched QCD with improved Wilson quarks,” *Eur. Phys. J.* **C20** (2001) 541–552, `hep-lat/0103037`.

[100] R. V. Gavai and S. Gupta, “Valence quarks in the QCD plasma: Quark number susceptibilities and screening,” *Phys. Rev.* **D67** (2003) 034501, `hep-lat/0211015`.

[101] G. Boyd *et al.*, “Hadron Properties just before Deconfinement,” *Phys. Lett.* **B349** (1995) 170–176, `hep-lat/9501029`.

[102] J. Kapusta, “Electron Positron Pair Production as a probe of Chiral Symmetry in a hot QCD Plasma,” *Phys. Lett.* **B136** (1984) 201–203.

[103] M. G. Mustafa, A. Schafer, and M. H. Thoma, “Non-perturbative dilepton production from a quark-gluon plasma,” *Phys. Rev.* **C61** (2000) 024902, `hep-ph/9908461`.

[104] **CERES-Collaboration** Collaboration, B. Lenkeit *et al.*, “Recent results from Pb Au collisions at 158-GeV/c per nucleon obtained with the CERES spectrometer,” *Nucl. Phys.* **A661** (1999) 23–32, `nucl-ex/9910015`.

[105] G. E. Brown and M. Rho, “Scaling effective Lagrangians in a dense medium,” *Phys. Rev. Lett.* **66** (1991) 2720–2723.

[106] R. Rapp, “Signatures of thermal dilepton radiation at RHIC,” *Phys. Rev.* **C63** (2001) 054907, `hep-ph/0010101`.

[107] C. Gale and K. L. Haglin, “Electromagnetic radiation from relativistic nuclear collisions,” `hep-ph/0306098`.

[108] J. J. Sakurai, “Vector meson dominance and high-energy electron proton inelastic scattering,” *Phys. Rev. Lett.* **22** (1969) 981–984.

[109] R. Rapp and E. V. Shuryak, “Thermal dilepton radiation at intermediate masses at the CERN-SPS,” *Phys. Lett.* **B473** (2000) 13–19, `hep-ph/9909348`.

[110] I. Kvasnikova, C. Gale, and D. K. Srivastava, "Production of intermediate-mass dileptons in relativistic heavy ion collisions," *Phys. Rev.* **C65** (2002) 064903, `hep-ph/0112139`.

[111] T. Renk, R. A. Schneider, and W. Weise, "Phases of QCD, thermal quasiparticles and dilepton radiation from a fireball," *Phys. Rev.* **C66** (2002) 014902, `hep-ph/0201048`.

[112] G. Moore Private Comunnication.

[113] F. Gelis, "QCD calculations of thermal photon and dilepton production," *Nucl. Phys.* **A715** (2003) 329–338, `hep-ph/0209072`.

[114] F. Karsch, E. Laermann, P. Petreczky, S. Stickan, and I. Wetzorke, "Meson Spectral Functions below and above the deconfining Phase Transition," *in preparation.*

[115] G. Aarts and J. M. Martinez Resco, "Transport coefficients, spectral functions and the lattice," *JHEP* **04** (2002) 053, `hep-ph/0203177`.

[116] S. Gupta, "The electrical conductivity and soft photon emissivity of the QCD plasma," `hep-lat/0301006`.

[117] T. Altherr and P. Aurenche, "Finite Temperature QCD corrections to Lepton Pair Formation in a Quark - Gluon Plasma," *Z. Phys.* **C45** (1989) 99.

[118] E. Braaten, R. D. Pisarski, and T.-C. Yuan, "Production of soft Dileptons in the Quark - Gluon Plasma," *Phys. Rev. Lett.* **64** (1990) 2242.

[119] **WA98** Collaboration, M. M. Aggarwal *et al.*, "Recent results on Pb + Pb collisions at 158-A-GeV from the WA98 experiment at CERN," *Nucl. Phys.* **A638** (1998) 147–158.

[120] **WA98** Collaboration, M. M. Aggarwal *et al.*, "Observation of direct photons in central 158-A-GeV Pb-208 + Pb-208 collisions," *Phys. Rev. Lett.* **85** (2000) 3595–3599, `nucl-ex/0006008`.

[121] J. Kapusta, P. Lichard, and D. Seibert, "High-energy photons from quark - gluon plasma versus hot hadronic gas," *Phys. Rev.* **D44** (1991) 2774–2788. Erratum-ibid.**D47**(1993) 4171.

[122] F. Karsch and E. Laermann, "Thermodynamics and in-medium hadron properties from lattice QCD," `hep-lat/0305025`.

[123] T. Peitzmann and M. H. Thoma, "Direct photons from relativistic heavy-ion collisions," *Phys. Rept.* **364** (2002) 175–246, `hep-ph/0111114`.

Acknowledgements

> *We don't accomplish anything in this world alone ... and whatever happens is the result of the whole tapestry of one's life and all the weavings of individual threads from one to another that creates something.*
>
> S. D. O'Connor

Hiermit möchte ich mich bei allen bedanken, die mir bei der Anfertigung dieser Dissertation geholfen haben. Dies gilt insbesondere für meinen Doktorvater Prof. Dr. Frithjof Karsch für seine hervorragende Betreuung und seiner Bereitschaft sich jederzeit mit meinen Fragen auseinanderzusetzen. Desweiteren danken möchte ich Prof. Dr. Edwin Laermann für die vielen Diskussionen und Anregungen. Außerdem bedanke ich mich bei Dr. Peter Petreczky und insbesondere bei Dr. Ines Wetzorke für die gute Zusammenarbeit im Rahmen unseres Projektes “Finite Temperature Meson Correlation Functions”.

Bedanken möchte ich mich darüber hinaus bei allen anderen Mitgliedern und Ehemaligen der Forschergruppe (D6/E6) und weiteren Mitgliedern der Fakultät für Physik (E5) für die vielen Gespräche über (nicht-)physikalische Dinge die wesentlich zur angenehmen Atmosphäre während dieser Jahre beigetragen haben. Dies gilt insbesondere auch für die Sekretärinnen Gudrun Eickmeyer und Susi von Reder. Weiterhin bedanke ich mich bei den Mitgliedern des Support Teams für die gute und interessante Zusammenarbeit.

Ein besonderer Dank gilt noch meinen Eltern, die mich während des gesamten Studiums immer unterstützt haben.